

**University of Alberta**

**Studies on the Potential for Optical Amplification in Erbium-doped Silicon  
Monoxide**

by



**Thomas James Clement**

**A thesis submitted to the Faculty of Graduate Studies and Research  
in partial fulfillment of the requirements for the degree of**

**Master of Science**

**Department of Electrical and Computer Engineering**

**Edmonton, Alberta**

**Fall, 2006**



Library and  
Archives Canada

Bibliothèque et  
Archives Canada

Published Heritage  
Branch

Direction du  
Patrimoine de l'édition

395 Wellington Street  
Ottawa ON K1A 0N4  
Canada

395, rue Wellington  
Ottawa ON K1A 0N4  
Canada

*Your file* *Votre référence*  
*ISBN: 978-0-494-22245-4*  
*Our file* *Notre référence*  
*ISBN: 978-0-494-22245-4*

**NOTICE:**

The author has granted a non-exclusive license allowing Library and Archives Canada to reproduce, publish, archive, preserve, conserve, communicate to the public by telecommunication or on the Internet, loan, distribute and sell theses worldwide, for commercial or non-commercial purposes, in microform, paper, electronic and/or any other formats.

The author retains copyright ownership and moral rights in this thesis. Neither the thesis nor substantial extracts from it may be printed or otherwise reproduced without the author's permission.

**AVIS:**

L'auteur a accordé une licence non exclusive permettant à la Bibliothèque et Archives Canada de reproduire, publier, archiver, sauvegarder, conserver, transmettre au public par télécommunication ou par l'Internet, prêter, distribuer et vendre des thèses partout dans le monde, à des fins commerciales ou autres, sur support microforme, papier, électronique et/ou autres formats.

L'auteur conserve la propriété du droit d'auteur et des droits moraux qui protègent cette thèse. Ni la thèse ni des extraits substantiels de celle-ci ne doivent être imprimés ou autrement reproduits sans son autorisation.

---

In compliance with the Canadian Privacy Act some supporting forms may have been removed from this thesis.

Conformément à la loi canadienne sur la protection de la vie privée, quelques formulaires secondaires ont été enlevés de cette thèse.

While these forms may be included in the document page count, their removal does not represent any loss of content from the thesis.

Bien que ces formulaires aient inclus dans la pagination, il n'y aura aucun contenu manquant.

  
**Canada**

# Abstract

Waveguides with core layers of erbium-doped silicon monoxide (Er:SiO) were investigated for use as erbium-doped waveguide amplifiers (EDWAs). The Er:SiO was annealed to precipitate amorphous silicon nanoparticles, which act as broadband sensitizers for erbium. The annealed layers have an index of refraction of 1.9 at 1.5  $\mu m$ . Waveguide propagation losses were as low as  $\simeq 0.5$  dB/cm, and the measured absorption cross-section of the erbium  $^4I_{15/2}$  to  $^4I_{13/2}$  transition was approximately  $1 \times 10^{-20}$  cm<sup>2</sup>. Pumping of the erbium was conducted using both resonant and non-resonant pumping schemes. Under transverse pumping by a laser operating at 532 nm, both confined carrier absorption (CCA) and erbium-related signal change (ERSC) of 1.5  $\mu m$  probe light were observed. For all pump intensities tested, CCA was the dominant pump-induced mechanism. The invertible fraction of erbium ions saturated at approximately 20 %. Similar results were obtained by pumping with 980 nm light. 80 % of the erbium was believed to be inactive, and likely clustered.

# Acknowledgements

I would like to begin by thanking my family for their unwavering emotional support during my tenure as a Master's candidate. They propped me up when I needed it, and also reminded me consistently that there is life outside of school.

A most gracious thank you to both of my supervisors, Dr. Ray DeCorby, and Dr. Chris Haugen. I've learned a tremendous amount about science from these two, but probably just as much about life. They've been exceptionally patient with me, even when I'm sure they just wanted to kick me out of their offices!

Many thanks to Dr. Al Meldrum in the department of Physics for his support of this work, and for me specifically. He has an uncanny knack for taking a boring, focused meeting and turning it into something creative, informative, and fun.

I cannot thank David Clegg enough for all of the times he has bailed me out of week long searches for equipment, for his timely and succinct explanation of concepts, and his ability to lend a measure of order to our

chaotic lab space.

A special thank you to Hue Nguyen who taught me so much about processing, and was always willing to help! Thank you for your guidance, and for being a good friend.

To all of my student peers, but especially Nakeeran, Trevor, and Aaron, thank you. You have each had a hand in this work, and the document would not be what it is today without your creativity and help.

Thanks to all of the staff here at TRILabs for their kindness and helpfulness. The amount of time and effort that you have saved me is, I'm sure, something that I will never know.

Thanks to George Braybrook for his excellence in scanning electron microscopy. They are not good results until you can see them!

And finally, thanks to TRILabs, and NSERC for their gracious financial support of this work.

# Contents

<b>1</b>	<b>Introduction</b>	<b>1</b>
1.1	Cross-sections and Sensitization . . . . .	2
1.2	Erbium Doping of Silicon . . . . .	4
1.3	Erbium-doped Silicon Nanoparticle-doped Glasses . . . . .	6
1.4	Confined Carrier Absorption . . . . .	9
1.5	Erbium-doped Silicon Monoxide . . . . .	9
1.6	Goals and Outline of This Work . . . . .	11
<b>2</b>	<b>Basic Theory</b>	<b>12</b>
2.1	Introduction . . . . .	12
2.2	Swanepoel's Method . . . . .	13
2.3	Waveguide Design Tools . . . . .	16
2.3.1	The Three-Layer Slab Model . . . . .	16
2.3.2	The Leaky-Mode Four-Layer Slab Model . . . . .	21
2.3.3	The Four-Layer Slab Model for Strip-Loaded and Rib-Loaded Waveguides . . . . .	23
2.3.4	The Effective Index Method . . . . .	25
<b>3</b>	<b>Device Design and Fabrication</b>	<b>32</b>
3.1	Introduction . . . . .	32
3.2	Photomask Design . . . . .	33
3.2.1	Nanofab Photomask . . . . .	34
3.2.2	Adtek Photomask . . . . .	36
3.3	Successful Fabrication Processes . . . . .	40
3.3.1	The Silicon Post Prefabrication Method ( <i>SPPM</i> ) . . . . .	40
3.3.2	The Silicon Dioxide Ribload Process . . . . .	53
3.3.3	The SU8 Electron-Beam-Resist Stripload Process . . . . .	56
3.4	Failed Fabrication Processes . . . . .	58

3.4.1	Commercial PECVD Undercladdings . . . . .	58
3.4.2	Direct Etching of SiO and Er:SiO with BOE . . . . .	60
3.4.3	Rib Waveguide Fabrication by Dry Reactive Ion Etching	61
3.4.4	Rib Waveguides Produced by Direct Etching with KOH	62
3.4.5	The Metal Liftoff Process . . . . .	64
3.4.6	Torlon Striploaded Waveguides . . . . .	68
3.5	Suggestions for Further Development . . . . .	69
3.5.1	Suggestions on Organizational Approach . . . . .	70
3.5.2	Suggestions for Fabrication Specific to This Project . .	70
<b>4</b>	<b>Experimental Results</b>	<b>72</b>
4.1	Introduction . . . . .	72
4.2	The Index of Refraction . . . . .	72
4.3	Undercladding Design and Results . . . . .	74
4.3.1	Estimation of Substrate Leakage Loss for 2D Confining Waveguides . . . . .	75
4.4	Waveguide Loss Characterization . . . . .	78
4.4.1	Waveguide Loss Characterization Techniques . . . . .	79
4.4.2	Measured Waveguide Losses . . . . .	88
4.5	Spectroscopic Characteristics . . . . .	91
4.5.1	Absorption Cross-section . . . . .	92
4.5.2	Waveguide Photoluminescence . . . . .	94
4.5.3	Nonlinear Transmission . . . . .	99
4.5.4	Optical Pumping of Waveguides . . . . .	100
4.6	Discussion of Experimental Results . . . . .	113
<b>5</b>	<b>Conclusion</b>	<b>116</b>
5.1	Summary of Results . . . . .	116
5.2	Suggested Future Work . . . . .	120
5.2.1	Analysis of Loss in SiO Waveguides . . . . .	120
5.2.2	Further Exploration of SiO as an Erbium Host . . . . .	120
5.2.3	Fabrication Using Other Hosts . . . . .	121
	<b>Bibliography</b>	<b>121</b>
	<b>Appendices</b>	<b>129</b>

<b>A</b>	<b>Standard Processes</b>	<b>130</b>
A.1	The Standard Cleaning Process . . . . .	130
A.2	The Standard Annealing Process . . . . .	130
<b>B</b>	<b>Matlab Programs</b>	<b>132</b>
B.1	Matlab Code for Swanepoel's Method . . . . .	132
B.2	Matlab Code for the Three-Layer Slab Model . . . . .	155
B.3	Matlab Code for the Leaky Mode Slab Model . . . . .	158
	B.3.1 The Exact Method . . . . .	159
	B.3.2 The Approximate Technique . . . . .	165
B.4	Matlab Code for the Four-Layer Slab Model . . . . .	169
B.5	Matlab Code for the Effective Index Method (EIM) . . . . .	187



# List of Tables

2.1	The allowed TE modes for a slab structure with the listed parameters. . . . .	21
2.2	Allowed TE and TM modes for a slab structure with the listed parameters. . . . .	21
2.3	Simulation parameters used in the four-layer slab model. . . .	24
2.4	EIM substrate leakage loss simulation parameters. The parameters have been selected based on constructed devices. . .	29
2.5	Modal analysis of the structure in Fig. 2.5(a) as predicted by the EIM. . . . .	30
3.1	Etching parameters of the Trion <i>Phantom</i> RIE used for patterning the $SiO_2$ ICPRIE etch mask. . . . .	44
3.2	Etching parameters of the <i>OXFORD Plasmalab 100</i> ICPRIE used for etching posts into silicon. . . . .	45
3.3	PECVD silicon dioxide deposition parameters used in the $SiO_2$ – <i>RL</i> process. . . . .	55
3.4	Etching parameters of the Trion <i>Phantom</i> RIE used for directly patterning SiO. . . . .	62
3.5	Etching parameters of the Trion <i>Phantom</i> RIE used for fabricating $SiO_2$ ribload with a chrome mask. . . . .	67
3.6	The known etching parameters of the <i>OXFORD Plasmalab 100</i> ICPRIE used for etching into Torlon polymer. . . . .	69

4.1	Undercladding thickness simulation parameters. . . . .	75
4.2	EIM substrate leakage loss simulation parameters. The pa- rameters have been selected based on constructed devices. . .	77
4.3	Important loss results from ICPRIE wafer #2 chip #1. . . . .	89
4.4	Important loss results from ICPRIE wafer #7 chip #2. . . . .	90
4.5	Important loss results from ICPRIE wafer #7 chip #3. . . . .	90
5.1	Measured cross sections of the ${}^4I_{15/2}$ to ${}^4I_{13/2}$ transition. The type of cross-section and the peak cross-sectional wavelength are also listed. . . . .	119
A.1	The steps of the standard cleaning process. . . . .	130
A.2	The steps of the standard annealing process. . . . .	131

# List of Figures

1.1	Some of the erbium ion energy levels. The level designation, approximate ground state transition energy, and approximate ground state transition wavelengths are shown. . . . .	3
1.2	The sequence of events leading to erbium emission in crystalline silicon. First, an exciton is created in the silicon (I). Second, the exciton becomes trapped at an erbium-related level (II). Next, the trapped exciton recombines ( <i>III<sub>a</sub></i> ) and excites a nearby erbium ion ( <i>III<sub>b</sub></i> ). Finally, the excited erbium ion recombines radiatively (IV). At room temperature, a backtransfer process can occur which depopulates the erbium metastable level through the reverse of process III. Also at room temperature, an Auger mechanism can cause excited erbium in the metastable state to de-excite non-radiatively ( <i>V<sub>a</sub></i> ) and transfer its energy to a free carrier ( <i>V<sub>b</sub></i> ). Nonradiative decay mechanisms in the diagram are shown as dashed arrows. After ref. [14]. . . . .	5

1.3	Fast and slow energy transfer mechanisms between silicon nanoparticles and erbium. (a) The fast energy transfer process is very similar to the erbium emission process in bulk silicon. An exciton is created within a silicon nanoparticle (I), and becomes trapped at an erbium-related energy level (II). The trapped exciton recombines ( $\text{III}_a$ ) exciting an erbium ion to the first excited state ( $\text{III}_b$ ). The erbium eventually radiatively recombines emitting a $1.5 \mu\text{m}$ photon. (b) The slow transfer mechanism begins with an exciton being created within a nanoparticle (I). The exciton coulombically interacts with a nearby erbium ion, likely via a Forster mechanism, and de-excites non-radiatively ( $\text{II}_a$ ) exciting the erbium ion to one of its excited states ( $\text{II}_b$ ). The erbium ion rapidly de-excites to its first excited state and radiatively emits a $1.5 \mu\text{m}$ photon (III). Band-tails have been included in the conduction and valence bands since our ( $\text{Er:SiNC:SiO}_2$ ) material is amorphous and likely has a large number of sub-gap states. After [14, 25]. . . . .	8
1.4	A representation of Er:SiO on the nanoscale after an annealing treatment. Silicon clusters of diameter 2-3 nm are represented as black dots. At large distances from nanoclusters, the material may be $\text{SiO}_2$ . The composition within the interface region of the nanoclusters is not known, and may have several regions of different stoichiometry. Several erbium ions are located within the domain. It is widely believed that erbium will be forced out of silicon clusters because silicon has a very low erbium solubility compared with $\text{SiO}_2$ . After [7]. . . . .	10
2.1	A schematic of a thin film on a substrate. The thin film has a linear thickness gradient, a mean thickness $\bar{d}$ , and index of refraction $n_{\text{film}}$ . The substrate has an index $n_{\text{substrate}}$ . . . . .	15

2.2	A schematic of the three-layer slab waveguide considered. In general, $n_2 > n_1, n_3$ . The upper and lower layers are considered semi-infinite in the $x$ direction, whereas the guiding layer has specified thickness $d$ . Each of the three layers is considered infinite along the $y$ and $z$ directions. . . . .	17
2.3	(a) A schematic of a strip-loaded waveguide. (b) A schematic of a rib-loaded waveguide. (c) A schematic of the four-layer slab waveguide considered in this analysis. In all cases the core layer is indicated by label $n_3$ . . . . .	24
2.4	Results of the four-layer slab model seen in Fig. 2.3(c), whose parameters are listed in Table 2.3. The effective index of the fundamental TE mode is plotted against loading layer thickness. It is evident that a maximum lateral index contrast of 0.007 could be achieved based on these parameters. . . . .	25
2.5	The effective index method. (a) A schematic of the original problem showing a high-index core layer surrounded by 4-low index materials. The corners are not explicitly considered in the EIM method. (b) The first part of the EIM. A vertical slice from the center of (a) is expanded through the $y$ -dimension, and shown as a slab waveguide. The three-layer slab model is applied to this structure to determine modal effective indices of the structure. (c) The second part of the EIM, where a horizontal slice from the center of (a) is taken and expanded through the $x$ -dimension. However, instead of using the core index, $n_2$ , the effective indices from (b) are used as the core index for the second part of the EIM. The three-layer slab model is again applied, and modal effective indices are determined. These modes, and their effective indices are the approximate solutions for the $2D$ waveguide shown in (a). . . . .	27

2.6	(a) Estimated substrate leakage loss for the allowed TE modes of a waveguide with simulation parameters listed in table 2.4. As the mode order increases, the mode interacts with the substrate more, and leakage loss increases. (b) Same as (a) except for TM modes. TM modes are always less confined than TE modes and thus suffer higher substrate radiation loss. . . . .	31
3.1	An optical microscope image of an approx. $6\ \mu m$ wide chrome strip of a photomask laser-written and developed in the U of A Nanofab. A stitching error is visible in the chrome trace. Striation on the sides of the chrome trace is difficult to discern in this image. . . . .	35
3.2	SEM image of test mask written in the Nanofab with a <i>Heidelberg DWL – 200</i> . Nominally patterned $1\ \mu m$ feature, which turned out as approx. $0.35\ \mu m$ . a large amount of line-edge roughness is visible. . . . .	36
3.3	A schematic of the setup used for writing masks in the U of A Nanofab. First, structures are written by scanning an interfering laser beam from left to right (1). The interfering laser beam can only scan across a few hundred microns. For structures longer than a few hundred microns, the laser itself must be moved to allow scanning to take place in a new area (2). At the beginning of a new section the laser must begin writing at exactly the same spot that it ended at in the laser writing section. If this is not case, a stitching error may be present. In this figure the laser is shown as being physically displaced, though, typically it is the sample holder which is physically displaced. . . . .	37

3.4	A subsection of the design of the photomask from Adtek. The subsection contains 11 sets of waveguides, with 9 waveguides per set. Each set of waveguides has a different width, ranging from 1 $\mu m$ to 6 $\mu m$ in steps of 0.5 $\mu m$ . At the top of the Figure are circular features with diameters ranging from 20 $\mu m$ to 200 $\mu m$ in steps of 20 $\mu m$ . The circular features are intended to be used to pattern microcavities. . . . .	38
3.5	A schematic showing a waveguide which contains an S-bend, with a given horizontal and lateral offset. . . . .	39
3.6	A subsection of the design of the photomask from Adtek. The subsection contains 5 sets of 5 waveguides each, all of which are 4 $\mu m$ wide. Each set of waveguides has a fixed lateral offset and a horizontal offset between 250 $\mu m$ and 5000 $\mu m$ . . . . .	40
3.7	The complete design of the photomask from Adtek. . . . .	41
3.8	A picture of a circular feature which was produced on the Adtek photomask. . . . .	42
3.9	A step by step schematic of the major steps involved in the <i>SPPM</i> method. (a) A mask of $SiO_2$ is patterned on top of the silicon substrate. (b) Posts are etched into the silicon substrate using an ICPRIE tool. (c) The entire sample is thermally oxidized to deposit an undercladding of $SiO_2$ . (d) A layer of SiO is thermally evaporated onto the sample. The directionality of the evaporation plume causes material to be deposited primarily on the top of the post structures and in the trenches between the posts. . . . .	43

3.10	<p><i>Post</i> structure etched into a silicon wafer using an inductively-coupled plasma (ICP) reactive ion etching (RIE) system. A process gas ratio of <math>O_2:SF_6</math> is used to control the sidewall slope. The gas ratio used in (a) was 19:200. The gas ratio used in (b) was 17:200; it produced a steep sidewall as compared with (a). The gas ratio used in (c) was 13:200; it produced undercutting of the silicon dioxide mask. . . . .</p>	45
3.11	<p>Silicon dioxide undercladdings deposited by two separate methods. (a) A profile view of an undercladding deposited by electron-beam evaporation on a silicon post etch structure similar to that in Fig. 1(c). (b) Oblique angular view of structure from (a) emphasizing the apparent roughness at the undercladding edge. (c) A profile view of an undercladding deposited by wet thermal oxidation. of interest is the <i>lip</i> feature that develops by leaving the silicon dioxide etch mask in place. (d) Oblique angular view of (c) showing smoother edge features as compared to (b). . . . .</p>	47
3.12	<p>Waveguiding layers deposited during the <i>silicon post prefabrication method</i> onto undercladdings grown by wet thermal oxidation. Layers were deposited by either thermal evaporation of silicon monoxide, or by concurrent thermal evaporation of silicon monoxide and electron beam evaporation of erbium oxide. (a) A silicon monoxide layer deposited onto an undercladding with no <i>lip</i> feature. (b) An erbium-doped silicon monoxide layer deposited onto an undercladding with <i>lip</i> feature. The undercladding layers are similar to that shown in Figs. 3.11(c) and 3.11(d). . . . .</p>	48



3.13	(a) A schematic of a completed buried strip waveguide with an upper cladding. Viewed in the waveguide's profile plane. (b) a 3D view of a strip waveguide. The flux direction in the evaporation system will have angles $\theta$ and $\phi$ . For symmetric deposition on the waveguide sidewalls, $\theta$ must be zero. . . . .	50
3.14	profile view of a completed waveguide structure from the silicon post prefabrication method with an upper cladding of benzocyclobutene (BCB). . . . .	50
3.15	SEM images showing examples of the how patterns in the sidewall of a photoresist profile will transfer to silicon dioxide during RIE. (a) profile view of an etched $SiO_2$ rib; the break between the photoresist and $SiO_2$ layers is visible near the top of the image. Visible roughness on the sidewall appears seamless, with nothing to distinguish the different materials besides the height of each of the apparent <i>steps</i> . (b) Oblique-angle view of the sidewall of a rib etched into $SiO_2$ with the photoresist etch mask remaining. Roughness transfer from the photoresist to the $SiO_2$ is clearly visible. The only indication of the interface between the materials is the change between step heights, the larger step height is representative of etched $SiO_2$ . . . . .	52
3.16	SEM image showing the results of etching a layer of $SiO_2$ deposited by PECVD onto silicon using standard photolithography and BOE etching. . . . .	56
3.17	(a) Profile view of a completed ribloaded waveguide. (b) A view of the sidewall of the waveguide shown in (a). The sidewalls appear fairly smooth. . . . .	57
3.18	SEM image of the surface of commercially purchased $SiO_2$ undercladdings. The visible roughness will lead to interfacial scattering. . . . .	59

3.19	(a) Top-view of an as-deposited SiO waveguide produced by patterning with a negative tone photoresist and etching with BOE for 60 minutes. (b) Profile-view of an SiO waveguide produced by patterning with a negative tone photoresist and etching with BOE for 25 minutes. The dashed lines have been added for clarity to show the height of the etch. . . . .	61
3.20	Top-view of a waveguide produced by reactive ion etching of SiO with a positive-tone photoresist mask. A rough bottom surface is evident, likely due to high-energy ionic bombardment. The sidewall of the waveguide is very rough, and shows a <i>stepping</i> profile similar to that of Fig. 3.17, and attributed to stepping in the photoresist profile. . . . .	63
3.21	(a) Oblique angle view of a strip waveguide produced by KOH etching with a silicon nitride mask. Roughness levels seem low, and the break between guiding layer and undercladding layer is faintly visible as a shading contrast on the sidewalls of the waveguide; the material break is indicated by the orange bar on the figure. (b) Oblique angle view of a waveguide with some form of deposit native to the KOH etching bath. The deposit creates a large amount of roughness, which will be detrimental to waveguide performance. . . . .	65
3.22	A $SiO_2$ ribload process was attempted using a chrome masking layer patterned using the liftoff technique. (a) A silicon substrate with $SiO_2$ undercladding, $Er : SiO$ core layer, and $SiO_2$ loading layer; a layer of photoresist has been patterned on top of the structure. (b) Chrome was deposited on the structure, covering the photoresist and filling the trenches between the photoresist pattern. (c) The photoresist is stripped. (d) An RIE process is applied to the structure transferring the chrome pattern into the $SiO_2$ loading layer. . . . .	66

3.23	(a) Oblique angle view showing high rms roughness on the sidewall of the etched $SiO_2$ layer. Good verticality is evident due to the high etching contrast between chrome and $SiO_2$ .	
	(b) Oblique angle view showing some of the bent chrome features at the edges of the waveguide. This likely occurred due to a chrome continuum between the top of the photoresist profile, and the trench bottom. The bent chrome features are considered responsible for the majority of the visible line-edge roughness. . . . .	68
3.24	(a) Oblique angle view showing a delaminated Torlon ribbon.	
	(b) Roughness in the SiO layer associated with ICPRIE ion bombardment of the SiO layer beneath the Torlon layer. . . .	69
4.1	(a) Transmission spectra of substrate alone and of annealed silicon monoxide thin film on substrate collected using a spectrophotometer. Inset: The level of absorption in the 475 nm to 650 nm spectral region. The absorption at 532 nm is approx. 1 dB/ $\mu m$ . (b) A spectrally dependent index of refraction profile extracted using the transmission spectra from (a) and by employing the method described in Section 2.2. . . . .	74
4.2	Substrate leakage loss for a slab waveguide whose parameters are listed in table 4.1. . . . .	76
4.3	Substrate leakage loss for a strip waveguide whose parameters are listed in Table 4.2. . . . .	78
4.4	System setup used to characterize waveguides for insertion loss.	80
4.5	System setup used to empirically characterize <i>mode-field mismatch</i> losses in conjunction with the setup in Fig. 4.4. . . . .	81
4.6	System setup used to measure the mode-field profile of a waveguide by scanning across the face of the mode and periodically sampling the projected mode power. . . . .	82

4.7	(a) Modal profile of a post waveguide simulated using OptiBPM.	
	(b) Modal profile of a similar post waveguide collected by expanding the waveguide mode, and sampling the power in different regions of the mode. The limited resolution of the objective lens used in this setup is believed to cause the vertical expansion of the mode with respect to (a).	83
4.8	A schematic showing how a transmitted signal and a reflected signal can interfere at the output of a waveguide. The graph on the right displays the output signal strength as a function of the phase difference between the two beams. In general this description is a simplification as there are an infinite number of reflections within the waveguide, and an infinite number of beams interfering at the output of the waveguide.	85
4.9	Example of Fabry-Perot fringing in a singlemode waveguide with three different values of loss. As the loss increases, the modulation depth decreases.	86
4.10	A method of estimating the propagation loss of a waveguide by collecting light scattered from a waveguide.	87
4.11	Schematic of the system used to obtain broadband transmission scans of the erbium doped waveguides under test. Dashed red connections indicate free-space, and solid blue connections indicate an electrical connection.	92
4.12	A transmission experiment conducted on Er:SiO waveguides fabricated using the SU8 and <i>SPPM</i> processes, respectively. The results have been scaled to a length of 1 cm for more accurate comparison. EMPA conducted on the SU8 guides revealed an erbium concentration of approx. 1.7 at.%. The concentration of the SPPM waveguides is believed to be approx. 1 at.%. . . . .	93

4.13	Different schemes for excitation of erbium in Er:SRO materials. (a) Pumping of erbium using amorphous silicon nanoclusters as sensitizers. Photons with energy above the material bandgap energy excite carriers within silicon nanoclusters. Carriers may eventually recombine and transfer the recombinant energy to a nearby erbium ion. It is possible that some erbium ions may be at too large a distance from silicon nanoclusters to be properly sensitized, and may not be excitable using this pumping technique. (b) Pumping of erbium directly using resonant erbium pump bands such as 980 <i>nm</i> or 1480 <i>nm</i> . This method of pumping should be capable of exciting all of the erbium ions within the material. . . . .	95
4.14	A setup used to collect waveguide photoluminescence generated by pumping at either 980 <i>nm</i> or 1480 <i>nm</i> . Power is launched from the pump laser through the WDM 980/1480 port out of the common port and into the waveguide. Backwards-travelling photoluminescence in the 1550 <i>nm</i> band is coupled back into the WDM through the common port and is directed out the 1550 <i>nm</i> port before being collected using an OSA. . .	96
4.15	Photoluminescence from <i>SPPM</i> waveguides collected using the setup shown in Fig. 4.14. The PL strength does not follow the pumping strength in a linear fashion, indicating some form of saturation. . . . .	97
4.16	A setup used to collect waveguide photoluminescence. The waveguide is pumped using a diode laser operating at 374 <i>nm</i> . The laser is focused into a stripe covering the length of the waveguide. . . . .	97
4.17	Photoluminescence from <i>SPPM</i> waveguides collected using the setup shown in Fig. 4.16. The typical erbium profile can be seen. . . . .	98

4.18	Absorption and emission cross-sections for waveguides of the <i>SPPM</i> process. The emission cross-section is produced by using the photoluminescence curves in Fig. 4.15, and by assuming a radiative lifetime of 3 <i>ms</i> in line with the work of Hryciw et al [20]. . . . .	99
4.19	Ratio of $P_{PD2}/P_{PD1}$ plotted against $P_{PD1}$ . The undoped waveguide response is approximately linear. The doped waveguide shows significant nonlinearity. This could be a form of excited state absorption, or backtransfer mechanism. . . . .	101
4.20	The method used to estimate the 532 <i>nm</i> pump beam size. (a) An optical beam line is formed, and the beam projected onto a mode analyzer. The distances between each of the elements of the beam line were recorded. (b) The optical beam line is recreated but is now projected onto a waveguide. . . . .	103
4.21	The setup used to collect broadband spectral data under transverse 532 <i>nm</i> pumping. . . . .	103
4.22	(a) Broadband curves obtained under transverse 532 <i>nm</i> pumping. The data was collected using the setup shown in Fig. 4.21, and using a 4 <i>mm</i> long waveguide from the <i>SPPM</i> process. Each curve is taken at a different pump intensity. A description of how the pump intensity was calculated can be found in the text. The curves are affected by confined carrier absorption (CCA) and by erbium ionic emission. (b) Pump-induced change in the curves from (a) due to erbium-ion emission. The effect of CCA has been removed for clarity. . . . .	105
4.23	Percentage of total erbium in the metastable state plotted against transverse pump intensity. The inversion level seems to saturate at an inversion level of approx. 20 %. . . . .	106
4.24	The setup used to collect broadband spectral data under co-directional 980 <i>nm</i> pumping. . . . .	108

4.25	(a) Broadband curves obtained under transverse 532 nm pumping. The data was collected using the setup shown in Fig. 4.21. Each curve is taken at a different pump intensity. The curves are affected by confined carrier absorption (CCA) and by erbium ionic emission. (b) Pump-induced change in the curves from (a) due to erbium-ion emission. The effect of CCA has been removed for clarity. . . . .	109
4.26	Percentage of total erbium in the metastable state plotted against pump power. The results for 532 nm pumping are plotted alongside the results for 980 nm pumping for comparison. The inversion level for both pumping wavelengths seems to saturate at an inversion level of approx. 20 %. . . . .	110
4.27	Plots of confined carrier absorption for different combinations of signal and pump wavelengths and pump intensities. The blue curve (squares) shows the effect of 980 nm pump light on signal light at 1620 nm. The CCA reaches a level of approx. -5 dB. The light green curve (triangles) shows the CCA incurred for a pump wavelength of 532 nm and a signal wavelength of 1620 nm. The CCA reaches a level of approx. -10 dB. The dark green curve (circles) is similar to the conditions for the light green curve except the signal wavelength is set at 1534 nm. The difference between the light green curve and the dark green curve is due to the erbium emission. . . . .	111
4.28	The setup used to collect broadband spectral data under co-directional 1480 nm pumping. . . . .	112

- 4.29 (a) Broadband scans of a waveguide from the *SPPM* process under different 1480 nm pumping intensities. (b) signal change of the waveguide spectral response under pumping. (c) broadband scans in the spectral range 1520 nm to 1560 nm. Signal enhancement can be clearly seen for low pump powers. (d) Higher resolution plot of the signal change of the Er:SiO under increasing 1480 nm pumping. A feature centered around 1534 nm develops as the pump strength is increased. The feature seems like spectrum narrowing, an onset to lasing. . . . 114
- 4.30 Energy diagram showing one route to backtransfer of energy from the erbium ion to the silicon nanocluster under 1480 nm pumping. As can be seen on the left, the bandtails effectively terminate leaving a gap,  $E_{zero}$ , greater than 0.84 eV (the pump energy). First, an erbium ion is excited to the metastable  $^4I_{15/2}$  level (event I). Second, this electron is promoted to a higher state through either excited state absorption or upconversion (II). Finally, the erbium electron de-excites ( $III_a$ ) and creates an exciton within the silicon nanocluster ( $III_b$ ). . . . . 115



# List of Acronyms

<b>2D</b>	two dimensional
<b>3D</b>	three dimensional
<b>at.</b>	atomic
<b>BCB</b>	Benzocyclobutene
<b>BOE</b>	Buffered oxide etchant
<b>CCA</b>	Confined carrier absorption
<b>CCD</b>	Charge-coupled device
<b>CF<sub>4</sub></b>	Carbon tetrafluoride
<b>CHF<sub>3</sub></b>	Carbon hydro-trifluoride
<b>DC</b>	Direct current
<b>DI</b>	De-ionized
<b>DSP</b>	Double-side polish
<b>ECR-PECVD</b>	Electron-cyclotron resonance plasma-enhanced chemical vapour deposition
<b>EDFA</b>	Erbium-doped fiber amplifier
<b>EDWA</b>	Erbium-doped waveguide amplifier
<b>EIM</b>	Effective index method
<b>EM</b>	Electron microscopy

<b>EMPA</b>	Electron microprobe analysis
<b>Er</b>	Erbium
<b>Er<sub>2</sub>O<sub>3</sub></b>	Erbium oxide
<b>ERSC</b>	Erbium-related signal change
<b>Er:SiNC:SiO<sub>2</sub></b>	Erbium-doped silicon nanocluster-doped silicon dioxide
<b>Er:SiO</b>	Erbium-doped silicon monoxide
<b>EYDWA</b>	Erbium-ytterbium-doped waveguide amplifier
<b>FP</b>	Fabry-Perot
<b>H<sub>2</sub></b>	Hydrogen
<b>HMDS</b>	Hexamethyldisilazane
<b>ICPRIE</b>	Inductively coupled plasma reactive ion etch
<b>KOH</b>	Potassium hydroxide
<b>N<sub>2</sub></b>	Nitrogen
<b>ND</b>	Neutral density
<b>Nd:SiO</b>	Neodymium-doped silicon monoxide
<b>Nd:YAG</b>	Neodymium-doped yttrium-aluminum garnet
<b>O<sub>2</sub></b>	Oxygen
<b>OSA</b>	Optical spectrum analyzer
<b>PAI</b>	Polyamide-imide
<b>PC</b>	Polarization controller
<b>PECVD</b>	Plasma-enhanced chemical vapour deposition
<b>PL</b>	Photoluminescence
<b>RF</b>	Radio frequency

<b>RIE</b>	Reactive ion etch
<b>rpm</b>	Revolutions per minute
<b>SEM</b>	Scanning electron microscopy
<b>SF<sub>6</sub></b>	Sulfur hexafluoride
<b>Si</b>	Silicon
<b>SiNC</b>	Silicon nanocluster
<b>SiO</b>	Silicon monoxide
<b>SiO<sub>2</sub></b>	Silicon dioxide
<b>SiO<sub>2</sub>-RL</b>	Silicon dioxide ribload
<b>SiO<sub>x</sub></b>	Silicon-rich oxide
<b>SPPM</b>	Silicon post prefabrication method
<b>SRD</b>	Spin-rinse dryer
<b>SRO</b>	Silicon-rich oxide
<b>SSP</b>	Single-side polish
<b>TE</b>	Transverse electric
<b>TEM</b>	Transmission electron microscopy
<b>TEOS</b>	Tetraethylorthosilicate
<b>TM</b>	Transverse magnetic
<b>UV</b>	Ultraviolet
<b>UV-Vis</b>	Ultraviolet-visible
<b>WDM</b>	Wavelength division multiplexing
<b>WG</b>	Waveguide

# Chapter 1

## Introduction

The capabilities of long-haul networks have greatly expanded since the introduction of the erbium-doped fiber amplifier (EDFA) [1]. EDFAs provide the ability to strengthen optical signals without reverting to the bandwidth-limited electrical domain. Similarly, research into erbium-doped waveguide amplifiers (EDWAs) has expanded greatly in recent years, driven by the expansion of metropolitan (metro) optical networks [1, 2]. Because of the high density of devices, a low cost per device is desired, and a small areal footprint is essential. These performance requirements translate into a variety of EDWA fabrication guidelines. First, guiding materials with a high index of refraction contrast with respect to typical claddings are favoured. The high index contrast confines the optical mode more tightly to the core of the waveguide allowing for sharper bends and a smaller areal footprint [3]. High index contrast also allows for higher pump efficiencies, and lower amplifier power thresholds [4]. The EDWA should be compatible with a silicon substrate in order to take advantage of cheap and highly accessible silicon processing tools. Silicon compatibility is also important for optoelectronic integration.

Glasses have been used heavily in the production of EDWAs since some glasses can dissolve large amounts of erbium, and since glasses tend to

broaden the erbium transitions with respect to crystals [5]. The isotropic nature of glass lends itself well to the fabrication of waveguiding devices. Glass waveguides can be fabricated with low propagation losses, which is essential for efficient amplification. The erbium ion (and other rare-earth ions) has been heavily used to add luminescent functionality to materials. The electronic configuration of trivalent erbium is characterized by an incomplete inner shell, shielded by a pair of outer electron shells. This electron shielding makes the spectral emission bands of rare-earth ions relatively insensitive to the erbium host. This is important as luminescence bands are predictable, regardless of the host medium. Erbium has been doped into many glasses for optical amplification, including silicate glasses, aluminosilicate glasses, borosilicate glasses, phosphate glasses, soda-lime glasses, fluorozirconate glasses, yttria, and alumina glass, and more complex glasses which mix these former types [5, 6]. Each of these glasses can dissolve a different amount of erbium homogeneously in its matrix. The maximum amount of erbium that can be efficiently dissolved in a given glass is referred to as the erbium solubility. Typically, glasses that have higher erbium solubilities are more desirable. In a solid host, the erbium ion typically presents the energy level structure as shown in Fig. 1.1.

## 1.1 Cross-sections and Sensitization

Two important parameters of the erbium ion that are somewhat host-dependent are the absorption cross section and the stimulated emission cross-section [5]. These two parameters are related, and for simplicity, their peak values can often be assumed equal. Each transition between states shown in Fig. 1.1 such as the absorption transition between the  $^4I_{15/2}$  and  $^4I_{13/2}$  levels, has its own cross-sectional value. Relative to cross-sections in crystalline laser media, the transition cross-sections characteristic of the erbium-doped glasses are small. Large pump flux is required to invert the erbium ions directly,

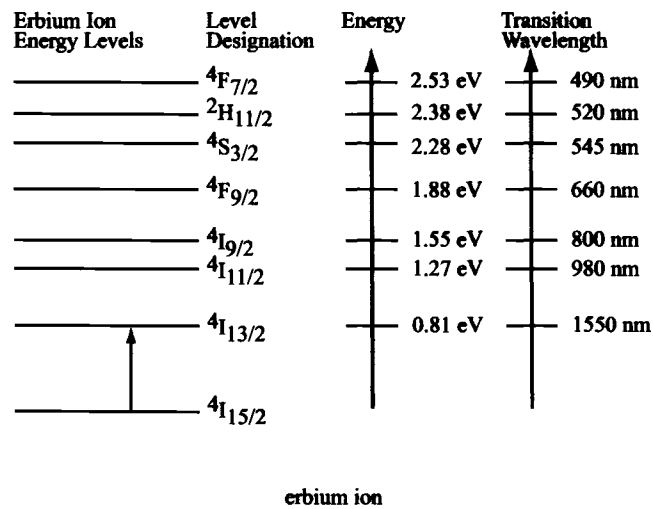


Figure 1.1: Some of the erbium ion energy levels. The level designation, approximate ground state transition energy, and approximate ground state transition wavelengths are shown.

so pump power is often co-propagated with signal power in the waveguides. The transitions are also somewhat spectrally narrow necessitating tuned narrow linewidth pump sources. Most erbium-doped sources to date have been pumped with either a high-power 980 *nm* pump laser or a high-power 1480 *nm* pump laser. Pumping schemes for EDWAs are typically expensive due to the cost of the pump laser, and also due to the need for precise coupling of the pump beam to a small waveguide. Furthermore, a wavelength division multiplexer (WDM) must be used to couple the pump light into the waveguide. Because of high costs and complexity associated with traditional pumping arrangements, methods for increasing the effective pump absorption cross-section in EDWAs are being investigated. These methods are typically referred to as sensitization. The most successful erbium sensitizer to date has been the ytterbium ion [7, 8, 9]. Compared to the erbium ion, the ytterbium ion has a much larger absorption cross-section at 980 *nm*. The ytterbium ion subsequently transfers large amounts of its absorbed energy to co-doped erbium ions. The erbium-ytterbium waveguide amplifier (EYDWA) has al-

lowed for shorter devices to be fabricated with lower pump power thresholds than for EDWAs. However, a co-propagated laser is still typically used to pump EYDWAs, relieving few of the financial drawbacks of current EDWAs.

## 1.2 Erbium Doping of Silicon

It has been known for a long time that silicon is a poor light emitter. Much research has been devoted to improving the luminescent functionality of silicon [10]. Some of the work has involved doping of erbium into silicon [11, 12]. When working at low temperature, efficient optical emission in the  $1.5 \mu m$  band due to the  ${}^4I_{13/2}$  to  ${}^4I_{15/2}$  erbium transition is readily observed. The silicon host also sensitizes the erbium through a carrier-mediated mechanism. Briefly, electron-hole pairs are generated when photons with energy greater than the bandgap impinge on the silicon. Excitons can then become trapped at erbium-related trap sites. The excitons recombine, in some cases transferring their energy to a nearby erbium ion. The erbium ion can then de-excite radiatively, emitting a photon in the  $1.5 \mu m$  band. This sequence of events is illustrated in Fig. 1.2. At room temperatures, however, luminescence of erbium-doped silicon is effectively quenched. This is attributed to a pair of mechanisms [11, 12, 13]. First, electrons can move from the excited erbium ion back to the silicon. This is labeled as backtransfer, and is the reverse of process *III* in Fig. 1.2. Also, at higher temperatures, an excited erbium ion can de-excite non-radiatively by transferring its energy to a free carrier in either the silicon conduction band or valence band. This process is called an impurity Auger effect, and is shown as process *V* in Fig. 1.2.

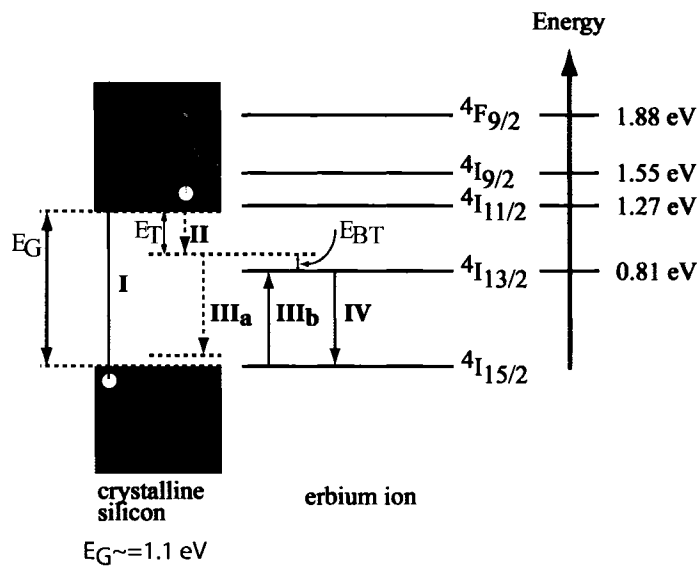


Figure 1.2: The sequence of events leading to erbium emission in crystalline silicon. First, an exciton is created in the silicon (I). Second, the exciton becomes trapped at an erbium-related level (II). Next, the trapped exciton recombines ( $III_a$ ) and excites a nearby erbium ion ( $III_b$ ). Finally, the excited erbium ion recombines radiatively (IV). At room temperature, a backtransfer process can occur which depopulates the erbium metastable level through the reverse of process III. Also at room temperature, an Auger mechanism can cause excited erbium in the metastable state to de-excite non-radiatively ( $V_a$ ) and transfer its energy to a free carrier ( $V_b$ ). Nonradiative decay mechanisms in the diagram are shown as dashed arrows. After ref. [14].



### 1.3 Erbium-doped Silicon Nanoparticle-doped Glasses

Further work in the area of erbium doping of silicon eventually led to the inclusion of significant amounts of oxygen to the material [7, 15]. It was found that the solubility of erbium in silicon scaled with the amount of oxygen, and that for erbium to be in its luminescent  $Er^{3+}$  state, it needed to be coordinated with oxygen atoms, and not silicon atoms [12, 16]. It was also found that increasing the oxygen content of the material resulted in improved room-temperature luminescence characteristics [15, 14]. It is believed that the energy barrier to backtransfer ( $E_{BT}$  in Fig. 1.2) is significantly increased, reducing the probability of the depopulation of the metastable erbium state even when there is significant thermal energy in the system. The magnitude of the impurity Auger effect is also significantly reduced [14]. Glasses of this type are generally referred to as erbium-doped silicon-rich oxides (Er:SRO), and contain an oxygen:silicon ratio between 0 and 2. Formation of this type of glass has been performed with a variety of methods including ion implantation of silica [17], ECR-PECVD with concurrent sputtering [18], RF co-sputtering [19], and concurrent thermal and electron-beam evaporation [20] to name a few.

In all cases, Er:SRO materials undergo a post deposition annealing stage which allows the as-deposited material to undergo a phase separation. The details of the annealing process can be found in Appendix A.2. The result is the formation of a high density of nanometre-scale clusters of silicon within a mixed phase matrix of  $SiO_2$  and possibly  $SiO_x$ . By increasing the annealing temperature and time, the phase separation becomes more complete, and the nanoclusters increase in size [21, 15, 22]. The nanoclusters may also crystallize at higher annealing temperatures. Wang et al state that clusters are amorphous after annealing temperature treatments between 400 °C and 800 °C, whereas clusters tend to crystallize at temperatures above 800 °C [21].

In general, amorphous and crystalline nanostructures are quite different electronically [21, 23]. The more random nature of bonding within amorphous silicon nanoclusters leads to tail states in the material bandgap [23]. Excitons generated in bulk silicon have a characteristic exciton radius called the Bohr exciton radius. In crystalline silicon the value of the Bohr exciton radius is approx.  $43 \text{ \AA}$  [24, 25], while in amorphous silicon band-tail states this value is approx.  $10 \text{ \AA}$  [23]. If the size of the nanoparticle approaches the Bohr exciton radius, quantum confinement effects will be present in the silicon nanoclusters and can increase the bandgap of the material. Given typical nanocluster sizes of  $2 \text{ nm}$  to  $6 \text{ nm}$ , quantum confinement effects can be quite significant in crystalline silicon. However, since typical cluster sizes are larger than the amorphous silicon Bohr exciton radius, quantum confinement effects will have little effect on the photoluminescence spectral location of amorphous silicon nanoclusters [23]. These differences are a strong indicator that processes occurring within amorphous and crystalline nanoclusters are quite different and need to be treated as such. Glasses of this type are also referred to as erbium-doped silicon nanoparticle-doped silica ( $\text{Er:SiNC:SiO}_2$ ). The nanoparticles create three-dimensional index of refraction confinement. The nanoclusters can absorb light and generate excitons, which are in turn trapped within the silicon nanoparticles [11]. The nanoparticles sensitize the erbium ions through a carrier-mediated process [26, 27]. The absorption cross-section of the nanoparticle sensitizers is up to 4-5 orders of magnitude higher than that for direct absorption by erbium [20]. The erbium luminescence competes with the nanoparticle luminescence, and for high erbium concentrations the nanoparticle luminescence is effectively quenched [20]. The erbium luminescence tends to increase with erbium concentration up to the point that concentration-based quenching mechanisms take effect [20]. The transfer of energy between silicon nanoparticles and erbium is believed to occur through two mechanisms [25]. These mechanisms are displayed in Fig. 1.3. The first mechanism is similar to the transfer of energy in erbium-doped

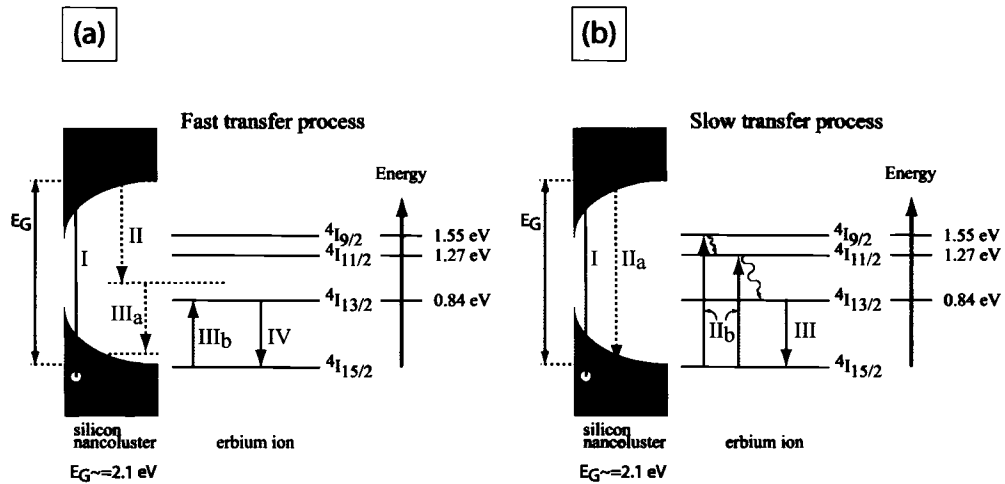


Figure 1.3: Fast and slow energy transfer mechanisms between silicon nanoparticles and erbium. (a) The fast energy transfer process is very similar to the erbium emission process in bulk silicon. An exciton is created within a silicon nanoparticle (I), and becomes trapped at an erbium-related energy level (II). The trapped exciton recombines (III<sub>a</sub>) exciting an erbium ion to the first excited state (III<sub>b</sub>). The erbium eventually radiatively recombines emitting a  $1.5 \mu\text{m}$  photon. (b) The slow transfer mechanism begins with an exciton being created within a nanoparticle (I). The exciton coulombically interacts with a nearby erbium ion, likely via a Forster mechanism, and de-excites non-radiatively (II<sub>a</sub>) exciting the erbium ion to one of its excited states (II<sub>b</sub>). The erbium ion rapidly de-excites to its first excited state and radiatively emits a  $1.5 \mu\text{m}$  photon (III). Band-tails have been included in the conduction and valence bands since our (Er:SiNC:SiO<sub>2</sub>) material is amorphous and likely has a large number of sub-gap states. After [14, 25].

silicon. An exciton becomes bound at an erbium-related trap and upon recombination excites the erbium ion to the metastable level. The erbium ion then de-excites radiatively. The second mechanism is due to direct coupling between confined excitons and erbium ions. This process is believed to excite the erbium ion to its second or third excited state [25]. The ion then non-radiatively relaxes to the metastable level and recombines radiatively. There is some evidence that small and amorphous clusters are better sensitizers for erbium ions than larger crystalline silicon clusters [28, 29, 30]. This is possibly explained by the smaller average spacing between erbium ions and the nearest-neighbour nanoclusters.

## 1.4 Confined Carrier Absorption

A few of the groups investigating the potential for optical amplification in the Er:SiNC: $SiO_2$  system have found them susceptible to confined carrier absorption (CCA) [31, 17, 32]. The mechanism has been documented in n-type silicon, and becomes more severe with increased donor concentration [33]. In each reported case the CCA competes with the erbium emission and in all but one case has led to net loss. When this process is greatly reduced, net optical amplification has been cited [18]. Determining regions of operation where erbium emission exceeds CCA is a critical step in the development of Er:SiNC: $SiO_2$  glasses.

## 1.5 Erbium-doped Silicon Monoxide

Erbium-doped silicon monoxide (Er:SiO) has previously been investigated by Roberts et al. [26, 34, 35]. They found that excitation of erbium proceeded through a carrier mediated energy transfer from the SiO glass to the erbium ion. This energy transfer is likely comprised of the mechanisms described in section 1.3. Hryciw et al. have deposited thin films of Er:SiO through concurrent thermal and electron-beam deposition of SiO and erbium oxide [20]. A post-deposition annealing technique is applied to the glass to optimize the photoluminescence characteristics of the material. Transmission electron microscopy (TEM) analysis of the annealed Er:SiO films reveals a high density of small amorphous silicon nanoclusters of diameter 2 – 3 nm (approx.  $2 \times 10^{19}$  nanoparticles per cubic centimeter) after an annealing treatment. This medium has been shown to exhibit a carrier-mediated process similar to the previous descriptions of indirect erbium excitation by Roberts et al.. Energy transfer is likely comprised of the mechanisms discussed in section 1.3. A diagram of what the silicon nanoparticle glass might look like on the nanometer scale is shown in Fig. 1.4.

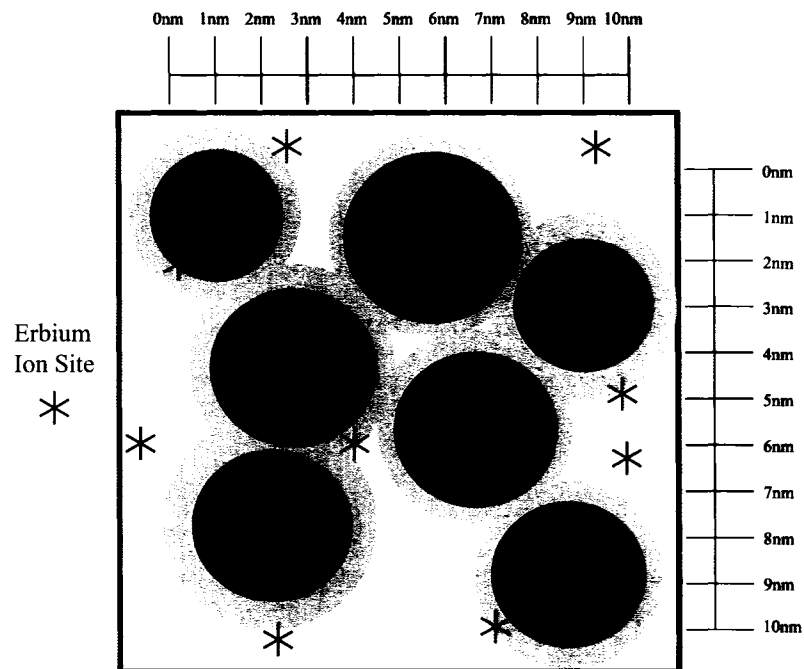


Figure 1.4: A representation of Er:SiO on the nanoscale after an annealing treatment. Silicon clusters of diameter 2-3 nm are represented as black dots. At large distances from nanoclusters, the material may be  $SiO_2$ . The composition within the interface region of the nanoclusters is not known, and may have several regions of different stoichiometry. Several erbium ions are located within the domain. It is widely believed that erbium will be forced out of silicon clusters because silicon has a very low erbium solubility compared with  $SiO_2$ . After [7].

## 1.6 Goals and Outline of This Work

The overriding goal of this work was to determine whether erbium-doped silicon monoxide can function as a material for optical amplification. Waveguides of the material were designed and fabricated on a silicon substrate. The waveguide losses and modal properties were characterized. Spectroscopic investigation of waveguides of Er:SiO was performed to determine the absorption and emission cross-sections of the  ${}^4I_{15/2}$  to  ${}^4I_{13/2}$  transition. Pumping experiments were performed on the waveguides using the standard  ${}^4I_{11/2}$  and  ${}^4I_{13/2}$  pumping bands. Erbium was also pumped indirectly using the silicon nanoclusters. Evidence of CCA and erbium amplification was documented for each pumping band, and will be discussed. Finally, a preliminary assessments of the suitability of Er:SiO as a material for optical amplification is provided.

Chapter 2 describes theory, and theoretical tools used to guide design and help interpret results. Chapter 3 documents approaches to the fabrication of waveguides, and documents successful and unsuccessful fabrication processes. Chapter 4 presents the experimental findings of this work including index of refraction, modal properties, waveguide losses, CCA, and erbium inversion levels. A discussion of the results is also provided. Chapter 5 presents assessments of the research, and suggests future directions for this project.

# Chapter 2

## Basic Theory

### 2.1 Introduction

Several well-known theories were used during this project to aid in the design of optical waveguides. This theory was used to help extract basic material parameters and also to simulate different practical waveguiding structures. In Section 2.2, a method for extracting the index of refraction is reviewed. In Section 2.3, a variety of waveguide theories are developed including:

1. Modal propagation in asymmetric 3-layer slab waveguides
2. Modal propagation in 4-layer slab waveguides
3. Evanescent leakage loss due to waveguide fabrication on a substrate with a high index of refraction
4. The effective index method (EIM) for 2D waveguiding

Theory was used to more efficiently direct waveguide design.

## 2.2 Swanepoel's Method

The index of refraction of a material is sensitive to material preparation techniques, and it is advantageous to have non-destructive techniques which can determine this parameter with speed and accuracy. Manificier and Swanepoel developed a technique to determine the index of refraction, thickness, thickness variation and potentially the absorption coefficient of a thin film on a transparent substrate [36, 37, 38]. The technique requires two transmission spectra as input. The first spectrum is a transmission scan of the substrate in the wavelength region of interest. The second spectrum is of the thin film on the substrate in the same spectral region. The thin film, whose surfaces are assumed nearly parallel, will produce interference fringes due to the index offsets at the air-film and film-substrate interfaces. The interference equation describing the wavelength spacing between transmission peaks is shown in eqn. 2.1.  $m$  corresponds to the fringe order,  $n(\lambda)$  is the thin film index of refraction (which is a function of wavelength),  $s$  is the index of refraction of the substrate,  $d$  is the film thickness, and  $\lambda$  is the wavelength. The fringe order,  $m$ , is either an integer or a half integer.

$$m\lambda = 2n(\lambda)d \quad (2.1)$$

The transmittance,  $T$  will vary according to eqn. 2.2, where the variables  $A$ ,  $B$ ,  $C$ , and  $D$  are expanded as shown in equations 2.3 - 2.9.

$$T = \frac{Ax}{B - C\cos(\phi) + Dx^2} \quad (2.2)$$

$$A = 16n^2s \quad (2.3)$$

$$B = (n + 1)^3(n + s^2) \quad (2.4)$$

$$C = 2(n^2 - 1)(n^2 - s^2) \quad (2.5)$$



$$D = (n - 1)^3(n - s^2) \quad (2.6)$$

$$\phi = 4\pi nd/\lambda \quad (2.7)$$

$$x = \exp(-\alpha d) \quad (2.8)$$

$$\alpha = (4\pi k)/\lambda \quad (2.9)$$

If we consider only the spectral region in which the thin film has low absorption loss, then a good approximation is  $\alpha = 0$ . It follows from eqn. 2.8 and eqn. 2.9 that  $x = 1$ , and  $k = 0$ . Eqn. 2.2 then reduces to eqn. 2.10.

$$T = \frac{A}{B - C\cos(\phi) + D} \quad (2.10)$$

The technique further assumes that there is a linear thickness gradient,  $\Delta d$ , across the film. Over the probed area of the thin film, the thickness variation can often be expressed as a linear function:

$$d = \bar{d} \pm \Delta d \quad (2.11)$$

where  $\bar{d}$  is the mean thickness and  $\Delta d$  is half of the linear thickness variation over the probed area of the thin film. These concepts are illustrated in Fig. 2.1.

From these relations, a pair of coupled transcendental equations can be devised. Eqn. 2.12 provides an upper envelope,  $T_{Md}$ , for the experimental transmission curve. Eqn. 2.13 provides a lower envelope,  $T_{md}$ , for the transmission curve and is equal to the transmission spectrum only at the curve's minima.

$$T_{Md} = \frac{\lambda}{2\pi n \Delta d} \frac{a}{(1 - b^2)^{1/2}} \arctan\left[\frac{1 + b}{(1 - b^2)^{1/2}} \tan\left(\frac{2\pi n \Delta d}{\lambda}\right)\right] \quad (2.12)$$

$$T_{md} = \frac{\lambda}{2\pi n \Delta d} \frac{a}{(1 - b^2)^{1/2}} \arctan\left[\frac{1 - b}{(1 - b^2)^{1/2}} \tan\left(\frac{2\pi n \Delta d}{\lambda}\right)\right], \quad (2.13)$$

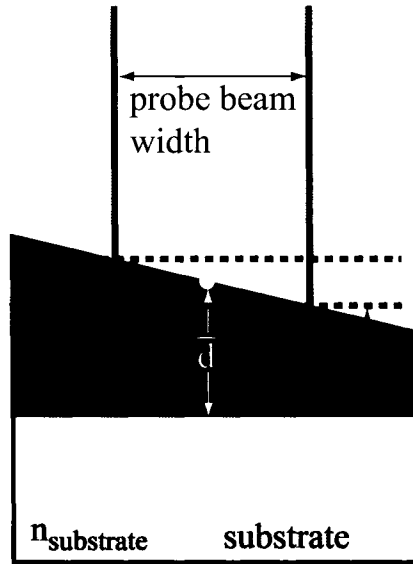


Figure 2.1: A schematic of a thin film on a substrate. The thin film has a linear thickness gradient, a mean thickness  $\bar{d}$ , and index of refraction  $n_{film}$ . The substrate has an index  $n_{substrate}$ .

where  $a$  and  $b$  are defined as,

$$a = \frac{A}{B + D} \quad (2.14)$$

$$b = \frac{C}{B + D}. \quad (2.15)$$

By solving for  $n$  and  $\Delta d$ , a discrete set of index values can be determined for different wavelengths. An index trend can generally be extracted from the data. By manipulating eqn. 2.1, eqn. 2.16 can be used to estimate a value of the thickness for each set of two consecutive maxima.

$$\bar{d} = \frac{\lambda_i \lambda_{i+1}}{2(\lambda_i n_{i+1} - \lambda_{i+1} n_i)} \quad (2.16)$$

where the  $i$  and  $i+1$  subscripts indicate data taken for successive maxima. A mean value for  $\bar{d}$  can be obtained by averaging each of the thickness values

determined using consecutive maxima. Given that values for  $\bar{d}$ ,  $n$ , and  $\lambda$  have all been determined, eqn. 2.1 can be employed to determine the approximate fringe orders. Recall that the fringe orders should be integers or half-integers. By rounding each of the fringe orders to the nearest half integer, eqn. 2.1 can be rearranged to form eqn. 2.17 which can be used to determine improved values for the indices of refraction at given wavelengths,

$$n = \frac{m\lambda}{2\bar{d}}. \quad (2.17)$$

Matlab code was written to solve this system of equations, and typically produced very good results. However, the accuracy of the method was observed to be significantly compromised with increasing  $\Delta d$ . The simulations also showed that the results are sensitive to optical DC transmission offsets in the raw spectrophotometer curves. The results are typically accurate to better than 1 % in both thin film thickness and index of refraction [37, 38].

## 2.3 Waveguide Design Tools

### 2.3.1 The Three-Layer Slab Model

The three-layer slab model applies the wave equation for a homogeneous medium to a set of 3 semi-infinite dielectric layers. The separate layers in this simple yet powerful model are considered to be linear, isotropic, homogeneous, and non-dispersive. These assumptions are often satisfied by judicious choice of operating conditions (wavelength, etc.). A schematic of a three-layer slab is shown in Fig. 2.2.

The upper and lower materials are assumed to be quasi-infinite in the x-direction. The middle layer has a specified thickness, but is considered infinite along both dimensions transverse to the x-direction. For waveguiding to be possible, the index of the guiding layer ( $n_2$ ) must be higher than that of the upper ( $n_1$ ) and lower ( $n_3$ ) layers. ( $n_1$ ) and ( $n_3$ ) can be equal, resulting

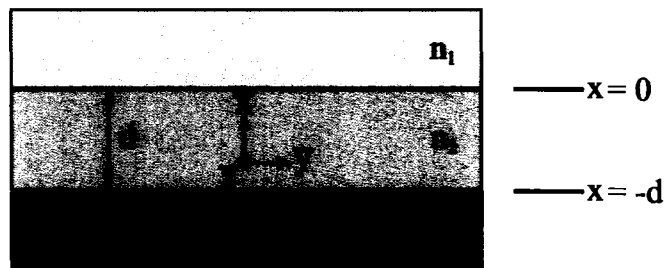


Figure 2.2: A schematic of the three-layer slab waveguide considered. In general,  $n_2 > n_1, n_3$ . The upper and lower layers are considered semi-infinite in the  $x$  direction, whereas the guiding layer has specified thickness  $d$ . Each of the three layers is considered infinite along the  $y$  and  $z$  directions.

in a symmetric slab waveguide, or they can be different, resulting in an asymmetric slab waveguide.

Starting from the wave equation, we can apply the electromagnetic boundary conditions at the interfaces of the guiding layer and each of the upper and lower layers. From the requirement of continuity of the tangential electric and magnetic fields at both interfaces, two separate and orthogonal classes of solutions result. For the first class of solution, the electric field vector is tangential to both interfaces. These solutions are called transverse electric (TE), because the electric field is completely transverse to the direction of propagation. For the second class of solution, the magnetic field is tangential to both interfaces. These solutions are thus commonly referred to as transverse magnetic (TM). Each solution to the wave equation in the three-layer slab model is either TE or TM. In general, there are infinite TE and TM solutions to the wave equation, but only a finite set correspond to bound or guided modes. The number of guided modes is determined by the indices of refraction of the layers and the thickness of the guiding layer. Each modal solution is characterized by its own unique longitudinal propagation constant,  $\beta$ , and transverse propagation constant,  $\kappa$ . These propagation constants are eigenvalues of the eigenequations, which mathematically describe the three-layer slab waveguide.

Assuming mode propagation along the z-direction, the electric and magnetic fields for the three-layer slab waveguide can be expressed as:

$$\mathbf{E}(\mathbf{r}, t) = \mathbf{E}(x)e^{i(\omega t - \beta z)}, \quad (2.18)$$

$$\mathbf{H}(\mathbf{r}, t) = \mathbf{H}(x)e^{i(\omega t - \beta z)}. \quad (2.19)$$

By inserting these assumed solutions into Maxwell's equations (for linear, non-dispersive, isotropic and homogeneous media) we can develop wave equations pertinent to the cases of TE and TM propagation. For TE propagation, we derive a wave equation in terms of only the transverse (y-direction) electric field. This is shown in eqn. 2.20:

$$\frac{d^2 E_y(x)}{dx^2} + [k_0 n^2(x) - \beta^2] E_y(x) = 0. \quad (2.20)$$

Similarly, for TM, we can derive a wave equation in terms of only the transverse (y-directed) magnetic field,

$$\frac{d^2 H_y(x)}{dx^2} + [k_0 n^2(x) - \beta^2] H_y(x) = 0. \quad (2.21)$$

These wave equations are standard second-order differential equations. A general solution to the TE wave equation is

$$E_j(x) = A_j e^{i\gamma_j x} + B_j e^{-i\gamma_j x}. \quad (2.22)$$

This solution satisfies the TE wave equation provided that the following relation holds:

$$\gamma_j = \sqrt{k_0^2 n_j^2 - \beta^2}. \quad (2.23)$$

It is evident that if the argument under the square root is positive, then  $\gamma_j$  will be real, and eqn. 2.22 will be sinusoidal in nature. Conversely, if the argument is negative, then  $\gamma_j$  will be imaginary, and eqn. 2.22 will be

comprised of exponential functions. For guided modes, there is a sinusoidal solution within the guiding layer, and exponentially decreasing solutions in the upper and lower layers. Thus the electric field in the each of the layers takes on the form:

$$\begin{aligned}
E_{y-upper} &= Ae^{-\gamma_1 x}, \\
E_{y-guide} &= Be^{i\kappa_2 x} + Ce^{-i\kappa_2 x}, \\
E_{y-lower} &= De^{\gamma_3 x},
\end{aligned} \tag{2.24}$$

where:

$$\begin{aligned}
\gamma_1 &= \sqrt{\beta^2 - k_0^2 n_1^2}, \\
\kappa_2 &= \sqrt{k_0^2 n_2^2 - \beta^2}, \\
\gamma_3 &= \sqrt{\beta^2 - k_0^2 n_3^2}.
\end{aligned} \tag{2.25}$$

Note that the the exponential arguments in eqn. 2.24 for the upper and lower layers are of opposite polarity, and have been chosen in accordance with the origin in Fig. 2.2 to provide exponentially decreasing solutions in the upper and lower layers of the slab.

Finally, if we apply the boundary conditions at both interfaces, we can derive the transcendental eigenequation

$$\tan(\kappa_2 h) = \frac{\gamma_1 + \gamma_3}{\kappa_2 \left[1 - \frac{\gamma_1 \gamma_3}{\kappa_2^2}\right]}. \tag{2.26}$$

This eigenequation governs TE propagation in an asymmetric three-layer slab waveguide. Taking a similar approach with 2.21 as we did with 2.20, we find a transcendental eigenequation for TM propagation in the asymmetric

three layer slab waveguide:

$$\tan(\kappa_2 h) = \frac{\kappa_2 \left[ \frac{n_2^2}{n_3^2} \gamma_3 + \frac{n_2^2}{n_1^2} \gamma_1 \right]}{\kappa_2^2 - \frac{n_2^4}{n_1^2 n_3^2} \gamma_1 \gamma_3}. \quad (2.27)$$

These equations can be solved numerically to determine the allowed propagation constants. Each of these solutions is commonly called a *mode* of propagation for the structure. It is common to assign an effective index,  $N$ , to each of the modes defined as

$$N = \frac{\beta}{k_0}. \quad (2.28)$$

Intuitively, the effective index gauges how much of the mode propagates within the high-index guiding region of the slab, and how much of the mode propagates as exponential tails in the upper and lower claddings of the slab. The fundamental mode of a waveguide always has the highest effective index. Higher-order modes have lower effective indices, and extend further into the upper and lower slab layers.

### Application of the Three-Layer Slab Model

The three-layer slab model is useful for determining possible modes of propagation in a given slab waveguide structure. For work conducted throughout this thesis, a guiding layer index of refraction of 1.9 has been typical. Also, both silicon dioxide and polymer claddings have been extensively employed in this work, and these have indices of refraction of approx. 1.5. Matlab programs were developed to determine modal solutions based on inputs of wavelength, indices of refraction, and the guiding layer thickness. These programs have been included in Appendix B.2. Thicknesses of  $0.65 \mu m$  and  $6 \mu m$  have been simulated for allowable mode propagation for both TE and TM polarization, at both  $1300 nm$  and  $1550 nm$  wavelengths. These are representative of the core thickness and width, respectively, for the *SPPM*

n1=1.5, n2=1.9, n3=1.5, t= 6 $\mu$ m, lambda = 1550 nm			
Wavelength (nm)	Polarization	Mode Order	Effective Index
1550	TE	1	1.89617
1550	TE	2	1.88463
1550	TE	3	1.86528
1550	TE	4	1.83794
1550	TE	5	1.80235
1550	TE	6	1.75819
1550	TE	7	1.70511
1550	TE	8	1.64284
1550	TE	9	1.57182

Table 2.1: The allowed TE modes for a slab structure with the listed parameters.

n1=1.5, n2=1.9, n3=1.5, t= 0.65 $\mu$ m lambda = 1300 nm, 1550 nm			
Wavelength (nm)	Polarization	Mode Order	Effective Index
1550	TE	1	1.76556
1550	TM	1	1.72621
1300	TE	1	1.79108
1300	TM	1	1.76081

Table 2.2: Allowed TE and TM modes for a slab structure with the listed parameters.

waveguides described in Section 3.3.1 and characterized in Chapter 4. Table 2.1 details TE modes which can propagate at wavelength 1550 nm for a slab width of 6  $\mu$ m. Table 2.2 details the allowed modes for a 0.65  $\mu$ m slab thickness, for both 1300 nm and 1550nm wavelengths.

### 2.3.2 The Leaky-Mode Four-Layer Slab Model

The three-layer slab model developed in Sec. 2.3.1 is an idealization. Though it is possible to form waveguides on low index substrates such as silicate glass, quartz, or sapphire, the substrate of choice is usually silicon. Due to the cost advantages of processing on silicon, the large body of knowledge related to silicon, and the potential for optoelectronic integration, compatibility with



a silicon substrate is highly advantageous for mainstream application of any integrated optic technology. Unfortunately, silicon has an index of refraction that is higher than that of most optical waveguide materials. As a result, guided mode energy is not truly confined to the core, but radiates into the substrate at a finite rate versus propagation distance. The thickness of the lower cladding layer must be sufficiently thick that such substrate radiation loss is reduced to an acceptable level. In determining the required buffer layer thickness, the extent to which the mode exists outside of the core layer must be known. The main variables that affect the core-mode-confinement, at a given wavelength, are the guiding-layer thickness and the index of refraction contrast between the guiding layer and cladding layers. These two variables combine to provide the modal effective index. The higher the modal effective index, the less the mode will exist outside of the guiding-layer, and the lower the required buffer-layer thickness. As can be seen in table 2.2, as the mode number increases the modal effective index decreases. Each successively higher mode will thus incur higher substrate leakage loss. A few papers have treated this problem [39, 40, 41] in a way similar to Section 2.3.1. An eigenequation is determined by applying the Helmholtz equation within each of the separate layers, followed by applying the boundary conditions at each interface to link the separate regions. The leakage loss is introduced by use of a complex propagation constant:

$$\beta = \beta_{real} + i\beta_{imag}, \quad (2.29)$$

and numerical techniques are used to determine the roots in the complex plane. Unfortunately, it is both difficult and time-consuming to determine the complex roots numerically. Stutius and Streifer also developed an analytical approximation technique to determine the complex  $\beta$  values [39]. The method starts by calculating the  $\beta$  values as in section 2.3.1, and then uses this value to determine the real  $\beta$  values for the leaky model. Both methods were coded in Matlab (see Appendix B.3), and were found to give nearly

identical results. However, the approximate technique is much faster than the exact solver, and was thus used in subsequent waveguide designs.

### 2.3.3 The Four-Layer Slab Model for Strip-Loaded and Rib-Loaded Waveguides

Due to difficulties in etching thermally evaporated silicon monoxide layers in this work, it was desirable to fabricate 2-dimensionally confining waveguides through strip-loading or rib-loading [42]. In these two methods a second material is deposited adjacent to the guiding layer. A strip-loaded waveguide and rib-loaded waveguide, and a 4 layer slab model are shown in Fig. 2.3. The *loading* layer should have a lower index of refraction than the experimental material (layer 3) in order that the majority of the light travels through the desired core layer, but should be able to provide high lateral index contrast. The three-layer slab model described previously is insufficient to determine the allowed modes of propagation in this four-layer slab structure. However, the four-layer slab model has several common points with the three-layer slab model. Both of the models assume the guiding layer has the highest index of refraction surrounded by layers with lower refractive index. Considering the wave equation, (2.20), along with the proposed electric field solution, eqn. (2.22), as discussed in section 2.3.1, the modes of propagation will have sinusoidal solutions in the high-index guiding region and exponentially decaying solutions in the three lower-index cladding layers. Thus the electric field in the four-layer slab model will have the form:

$$\begin{aligned}
 E_y &= Ae^{-\gamma_1 x}, & x > t_2 \\
 E_y &= Be^{-\gamma_2 x}, & t_2 > x > 0 \\
 E_y &= Ce^{i\kappa_3 x} + De^{-i\kappa_3 x}, & 0 > x > -t_1 \\
 E_y &= Fe^{\gamma_4 x}, & x < -t_1
 \end{aligned} \tag{2.30}$$

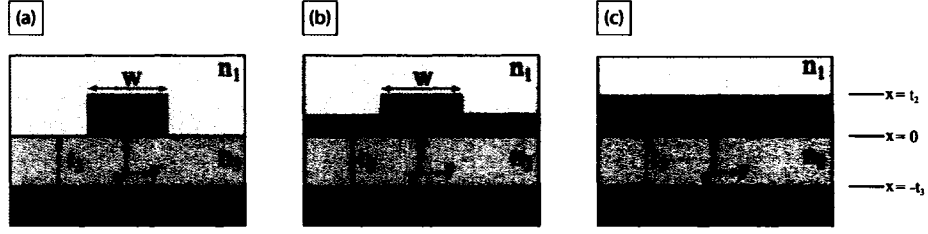


Figure 2.3: (a) A schematic of a strip-loaded waveguide. (b) A schematic of a rib-loaded waveguide. (c) A schematic of the four-layer slab waveguide considered in this analysis. In all cases the core layer is indicated by label  $n_3$ .

Simulation wavelength = 1550 nm		
Simulation polarization = TE		
Layer number	Refractive Index	Thickness ( $\mu m$ )
1	1.0	infinite
2	1.46	0.01 - 0.7
3	1.9	1.0
4	1.46	infinite

Table 2.3: Simulation parameters used in the four-layer slab model.

where the  $\gamma_j$  ( $j = 1,2,4$ ) and  $\kappa_3$  coefficients are given by:

$$\begin{aligned}
 \gamma_1 &= \sqrt{\beta^2 - k_0^2 n_1^2} \\
 \gamma_2 &= \sqrt{\beta^2 - k_0^2 n_2^2} \\
 \kappa_3 &= \sqrt{k_0^2 n_3^2 - \beta^2} \\
 \gamma_4 &= \sqrt{\beta^2 - k_0^2 n_4^2}
 \end{aligned} \tag{2.31}$$

By applying the boundary conditions at each of the interfaces, an eigenequation can be derived to determine the propagation constants of the allowed TE modes for the structure. This method was coded in Matlab, and is included in Appendix B.4. Simulations were conducted using this model to determine the amount of lateral index contrast which could be achieved using a loading layer of PECVD  $SiO_2$ . Simulation parameters are listed in Table 2.3. The resulting effective indices of refraction for the various loading layer thicknesses

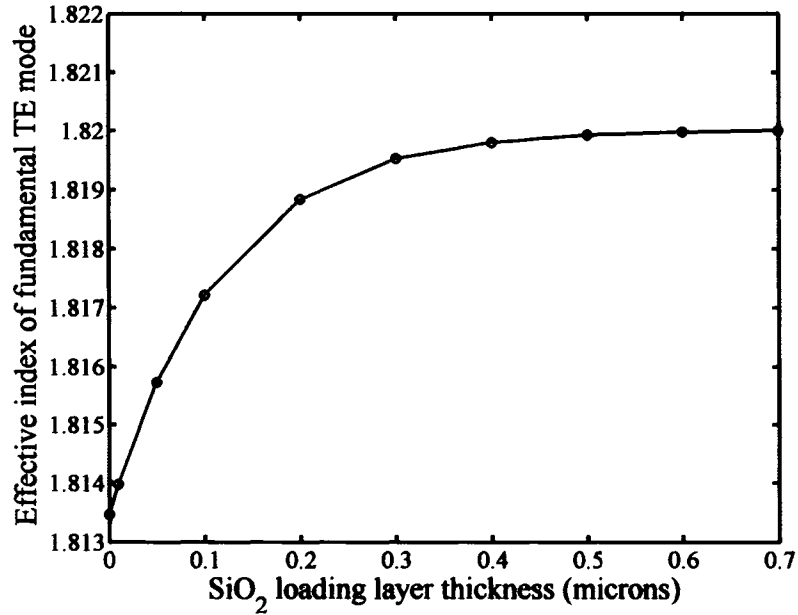


Figure 2.4: Results of the four-layer slab model seen in Fig. 2.3(c), whose parameters are listed in Table 2.3. The effective index of the fundamental TE mode is plotted against loading layer thickness. It is evident that a maximum lateral index contrast of 0.007 could be achieved based on these parameters.

are shown in Fig. 2.4. It seems clear that the increase of effective index saturates for a loading layer thickness of approx. 600 nm. The maximum lateral index contrast would occur if the guiding region had a loading layer thickness greater than 600 nm and if the cladding regions had no remaining loading layer. The lateral contrast in index of refraction could be as much as 0.007. Experimental structures similar to those simulated here are discussed in Sec. 3.3.2.

### 2.3.4 The Effective Index Method

There are several techniques that have been developed to accurately assess the modal characteristics of 2D waveguides structures [43]. One of the most widely used techniques is the effective index method (EIM) [43, 44, 42]. This

method is popular due to its simplicity of implementation and of understanding. In  $2D$  waveguides, the electric and magnetic fields are no longer completely polarized along a single direction as in the slab waveguide case. However, the modes are typically either quasi-TE or quasi-TM, and as such the assumption of complete polarization is approximately valid. The EIM technique is akin to a separation of variables, and amounts intuitively to assuming that the horizontal and vertical boundaries of a  $2D$  waveguide can be separated and treated as two separate  $1D$  slab waveguides, where the effective index determined from the first slab waveguide is used as the core index for the second step of the EIM. Fig. 2.5 shows the sequence of steps in applying the EIM.

Starting from The  $2D$  scalar wave equation, 2.32, a solution is proposed as in eqn 2.33

$$\frac{\delta E(x, y)}{\delta x^2} + \frac{\delta E(x, y)}{\delta y^2} + [k_0^2 n^2(x, y) - \beta^2]E(x, y) = 0 \quad (2.32)$$

$$E(x, y) = \theta(x, y)\phi(y) \quad (2.33)$$

Substituting (2.33) into (2.32), we find a pair of coupled differential equations:

$$\frac{\delta^2 \theta(x, y)}{\delta x^2} + [k_0^2 n^2(x, y) - k_0^2 N^2(y)]\theta(x, y) = 0 \quad (2.34)$$

$$\frac{\delta^2 \phi}{\delta y^2} - \left(\frac{2 \delta \theta}{\theta \delta y}\right) \frac{\delta \phi}{\delta y} + (k_0^2 N^2(y) + \left(\frac{1}{\theta} \frac{\delta^2 \theta}{\delta y^2}\right) - \beta^2)\phi = 0 \quad (2.35)$$

It is assumed that the  $y$ -component of the function  $\theta(x, y)$  varies slowly so that partial derivatives of  $\theta$  with respect to  $y$  can be neglected. Eqn. (2.35) is then reduced to :

$$\frac{\delta^2 \phi}{\delta y^2} + [k_0^2 N^2(y) - \beta^2]\phi = 0 \quad (2.36)$$

which has the same form as eqns. (2.34), (2.20), and (2.21). Each of these equations can be solved in the same manner as demonstrated in section 2.3.1.

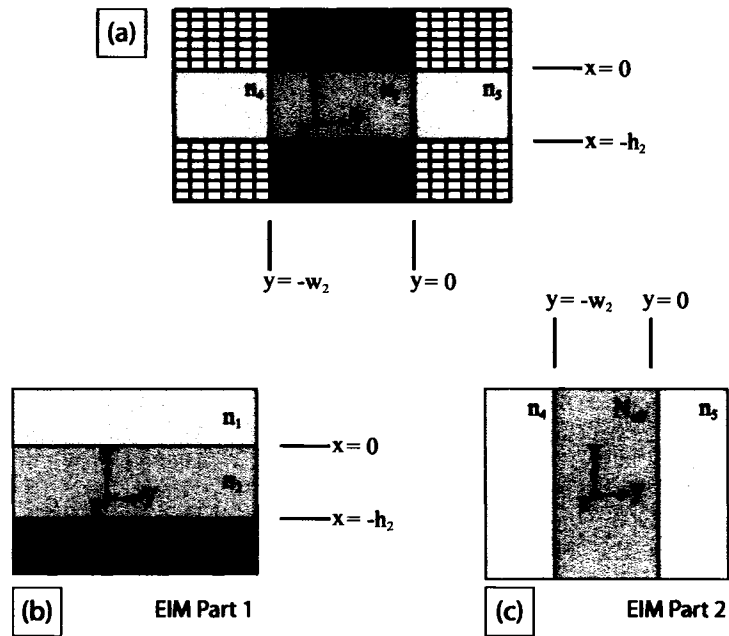


Figure 2.5: The effective index method. (a) A schematic of the original problem showing a high-index core layer surrounded by 4-low index materials. The corners are not explicitly considered in the EIM method. (b) The first part of the EIM. A vertical slice from the center of (a) is expanded through the  $y$ -dimension, and shown as a slab waveguide. The three-layer slab model is applied to this structure to determine modal effective indices of the structure. (c) The second part of the EIM, where a horizontal slice from the center of (a) is taken and expanded through the  $x$ -dimension. However, instead of using the core index,  $n_2$ , the effective indices from (b) are used as the core index for the second part of the EIM. The three-layer slab model is again applied, and modal effective indices are determined. These modes, and their effective indices are the approximate solutions for the 2D waveguide shown in (a).

The  $\beta$  values solved in equation 2.34 provide the index of refraction  $N(y)$  required to solve the second differential equation. The electric fields are determined for each of the slab waveguides and then combined as in 2.33. It is noted that, since in  $2D$  waveguides the fields are polarized strongly along either the horizontal or vertical dimensions, the eigenequations solved for the first and second steps must be different. If the electric field is strongly polarized along the x-direction in Fig. 2.5 then the mode is a quasi-TE mode, and we start with a TE eigenequation. A TM eigenequation is then used for the second part of the EIM. If the electric field is strongly polarized in the y-direction, then the mode is quasi-TM, and the eigenequations used to solve respective parts of the EIM are reversed from that for quasi-TE. The modal order of a particular solution is shown in the notation as  $TX^{p,q}$ , where  $X$  is either  $E$  or  $M$ ,  $p$  is the solution order from the first part of the EIM, and  $q$  is the solution order from the second part of the EIM.

### Application of the EIM

Suppose we have a rectangular strip waveguide of width  $6 \mu m$  and height  $0.65 \mu m$ . Suppose also, that the core material has an index of refraction of 1.9, that the upper and side media have index of refraction of 1.54, that the lower medium has an index of refraction of 1.46, and that we operate at a wavelength of  $1300 nm$ . The theoretical construct is shown in Fig. 2.5(a). We are interested in determining the allowed modes of propagation of this  $2D$  structure. The guides are to be fabricated on a silicon substrate, so modal leakage loss is also to be determined as a function of undercladding thickness. The first part of the EIM is to break this structure into two separate slab waveguide problems. The first problem is depicted in Fig. 2.5(b). Two modes of propagation are found, 1 TE mode and 1 TM mode. These modes are very similar to those listed in Table 2.2, except that the new structure is slightly asymmetric. The second part of the EIM uses the effective indices of refraction from the first part of the EIM as the core index for the second slab

Volume Designation	Material	Index of Refraction	Thickness
n1	BCB	1.54	infinite
n2	annealed silicon monoxide	1.9	height: $0.65 \mu m$ width: $6.0 \mu m$
n3	thermal $SiO_2$	1.46	$1.0 \mu m - 2.0 \mu m$
n4	BCB	1.54	infinite
n5	BCB	1.54	infinite
substrate	silicon	3.5	infinite
Simulation wavelength = $1.30 \mu m$			

Table 2.4: EIM substrate leakage loss simulation parameters. The parameters have been selected based on constructed devices.

waveguide. A separate slab waveguide must be evaluated for each solution found in the first part of the EIM. Thus, we must evaluate two separate slab waveguides with the core index specified from the first part of the EIM. Theoretical constructs of the cases to be evaluated are shown in Fig. 2.5 (a) and (b) respectively. The simulation parameters are reviewed in Table 2.4. The solutions found from evaluating these two cases give the approximate propagation constants for modes supported by the rectangular structure. A list of the allowed modes are shown in Table 2.5. By comparison, a mode-solver from Optiwave found only 3 quasi-TE modes (quasi-TM was not checked), though, the modal effective indices matched closely those found in the EIM.

The perturbation approach to predicting substrate leakage loss discussed in 2.3.2 was next applied to the modal data determined here. The perturbation approach requires only the modal effective index, some of the raw structural data, and a specification of undercladding thickness. By supplying the required information, substrate leakage loss of the EIM-simulated structure is shown in Fig. 2.6(a) and (b) for quasi-TE and quasi-TM modes respectively, as a function of undercladding thickness. It is readily observed that the lower the propagation constant, or effective modal index, the higher



Mode Number	Mode Designation	Modal Effective Index
1	<i>quasi</i> – $TE^{00}$	1.788
2	<i>quasi</i> – $TE^{01}$	1.780
3	<i>quasi</i> – $TM^{00}$	1.766
4	<i>quasi</i> – $TE^{02}$	1.765
5	<i>quasi</i> – $TM^{01}$	1.758
6	<i>quasi</i> – $TE^{03}$	1.744
7	<i>quasi</i> – $TM^{02}$	1.743
8	<i>quasi</i> – $TM^{03}$	1.723
9	<i>quasi</i> – $TE^{04}$	1.717
10	<i>quasi</i> – $TM^{04}$	1.697
11	<i>quasi</i> – $TE^{05}$	1.684
12	<i>quasi</i> – $TM^{05}$	1.665
13	<i>quasi</i> – $TE^{06}$	1.646
14	<i>quasi</i> – $TM^{06}$	1.627
15	<i>quasi</i> – $TE^{07}$	1.602
16	<i>quasi</i> – $TM^{07}$	1.584
17	<i>quasi</i> – $TE^{08}$	1.555

Table 2.5: Modal analysis of the structure in Fig. 2.5(a) as predicted by the EIM.

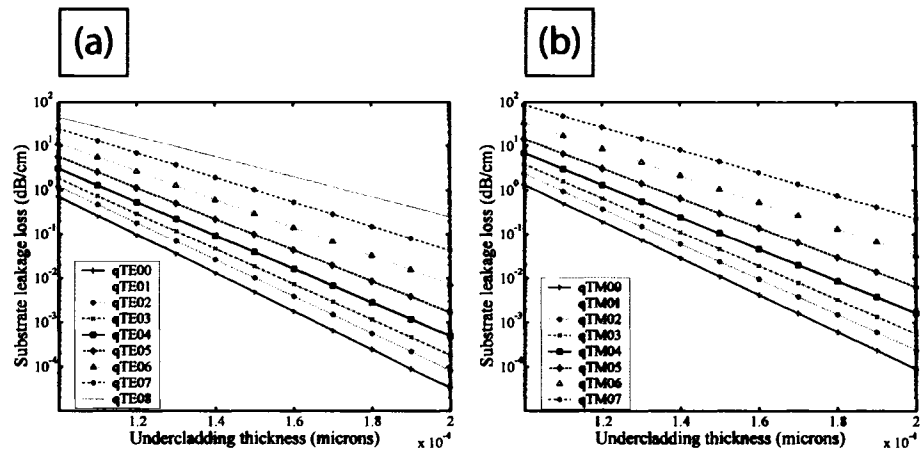


Figure 2.6: (a) Estimated substrate leakage loss for the allowed TE modes of a waveguide with simulation parameters listed in table 2.4. As the mode order increases, the mode interacts with the substrate more, and leakage loss increases. (b) Same as (a) except for TM modes. TM modes are always less confined than TE modes and thus suffer higher substrate radiation loss.

the leakage loss. This is intuitively expected since a lower effective index implies that the mode will exist more into the cladding layers, increasing the overlap of the mode and the substrate.

# Chapter 3

## Device Design and Fabrication

### 3.1 Introduction

Several waveguide processes were attempted in the course of this work, with varied degrees of success. Given the planar nature of microfabrication, and the step by step construction of devices, a logical approach to any design is the characterization of each step. If each step can be characterized for structure and repeatability, it is more straightforward to design and test subsequent steps. From the necessary step-by-step sequencing of microfabrication, it can be understood that errors (for example, sidewall roughness) can either be due to the current step, or could have persisted from earlier steps. Thus, sources of error in each step of the process must be identified and minimized.

A traditional approach was initially adopted to guide the fabrication of waveguides in silicon monoxide (SiO) or in erbium-doped SiO (Er:SiO). Undercladding thickness was evaluated and chosen to ensure negligible substrate leakage losses, and slab waveguides were created in a conventional way by depositing SiO or Er:SiO onto the undercladdings using physical vapour deposition techniques. To create 2D confining waveguides, a conventional process is to first use photolithography to create a pattern and then to transfer this

pattern into the material using an appropriate etchant. This process requires knowledge about chemicals that will etch SiO (or Er:SiO), and the rate at which they etch the material. It also requires knowledge of whether the material can withstand an etchant, or whether it will crack, delaminate, or suffer pitting, all of which are not intended outcomes of employing the etchant. It proved difficult to create satisfactory waveguides in SiO and Er:SiO by using this conventional approach. Thus, subsequent efforts focused on the development of waveguide processes that minimize the difficulties associated with etching novel materials. This was accomplished by focusing on methods to create 2D waveguides that involved etching of widely-used materials, such as silicon and silicon dioxide.

This chapter describes the design of waveguides, along with the fabrication processes used to create them. The design of master templates known as *masks* is described in Section 3.2. Section 3.3 is dedicated to the fabrication processes that were deemed successful. Section 3.4 describes fabrication processes that were deemed failures, and attempts to explain why they failed. Section 3.5 provides a summary and some suggestions as to how to improve further on waveguide fabrication.

## 3.2 Photomask Design

Optical photomasks were used as a master template for all of the lithography accomplished in this project. During the course of this project a change from negative image photomasks to positive-image photomasks was required due to the discontinued availability of negative-tone photoresist at the University of Alberta (U of A) Nanofab. Since the majority of work required a positively patterned image to be left after photolithography, new positive-image photomasks were required. Since only basic characteristics of waveguides were of immediate interest in this project, a mask containing mostly simple, straight waveguides of varied lateral width was designed.

### 3.2.1 Nanofab Photomask

Photomasks are expensive items to purchase, so anything that can potentially reduce the cost of purchase is welcome. At the time of this work, the Nanofab had recently purchased a *Heidelberg DWL – 200* photomask and direct write lithography system. Because of the capital investment, photomask cost to Nanofab consumers was well below commercial prices. The cost of a photomask in the Nanofab was approx. \$250. A similar mask from industry would cost approx. \$2000.

#### Design

The mask design was conducted by selecting waveguide widths that would allow for single-mode operation, but that could be patterned predictably. Six different widths ranging from  $1\mu m$  to  $6\mu m$  in steps of  $1\mu m$  were incorporated into the mask design. For each waveguide size a grouping of 5 waveguides was produced. Each size was repeated 3 times on the mask, giving a total of 18 groupings of 5 waveguides on the mask. Design was conducted using *Ledit* layout tools, and exported to GDSII format for data input to the *Heidelberg*.

#### Fabrication

The design was submitted to staff at the Nanofab in GDSII format. The design file was translated into a patterned photoresist profile by feeding the data into the *Heidelberg DWL – 200* and patterning a 5 inch quartz blank coated with a layer of chrome and a layer of AZ1518 photoresist. The photoresist was developed, and the chrome layer was etched using a wet chrome etchant. The photoresist was removed, and the finished photomask was returned.

#### Fabrication Results

Visual inspection of the photomask revealed visible striation on the sides of the remaining chrome. There were also visible stitching errors, where a

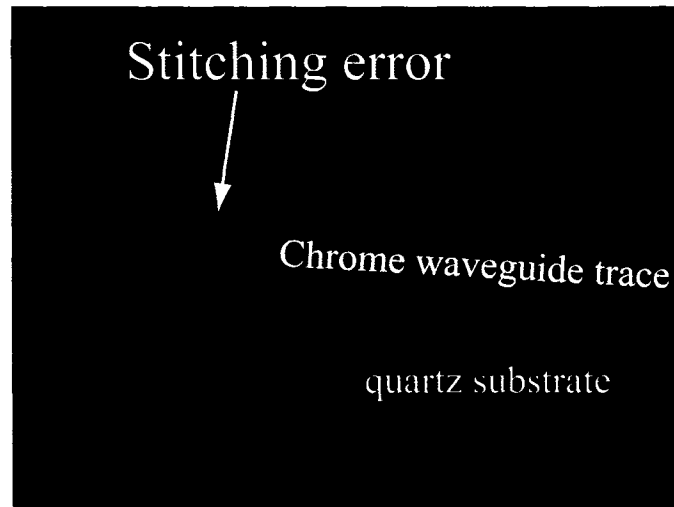


Figure 3.1: An optical microscope image of an approx.  $6\ \mu\text{m}$  wide chrome strip of a photomask laser-written and developed in the U of A Nanofab. A stitching error is visible in the chrome trace. Striation on the sides of the chrome trace is difficult to discern in this image.

lateral displacement occurred. Fig. 3.1 shows an optical microscope image of a stitching error in a chrome strip on the quartz substrate. After these problems were discussed with Nanofab staff, a small test area was written on a different mask, and this test area was taken for SEM. Fig. 3.2 shows what was nominally to have been a  $1\ \mu\text{m}$  wide waveguide feature. The width is closer to  $0.35\ \mu\text{m}$  and shows significant line-edge roughness. Stitching errors were also visible with optical microscopy. Stitching errors can occur if direct-write lithography tools (such as the *Heidelberg DWL – 200*) are used to pattern long features. Direct-write laser tools often use a scanned interfering laser beam to write short distances ( $500\ \mu\text{m}$ ) but must physically move the sample stage if longer lengths are required. A schematic of this setup is shown in Fig. 3.3. If a long continuous structure is to be written, it is necessary for the laser to start at exactly the same position after a physical displacement. This would ensure that there is no lengthwise discontinuity in the device, and no unplanned lateral offset in the design. Unfortunately, the

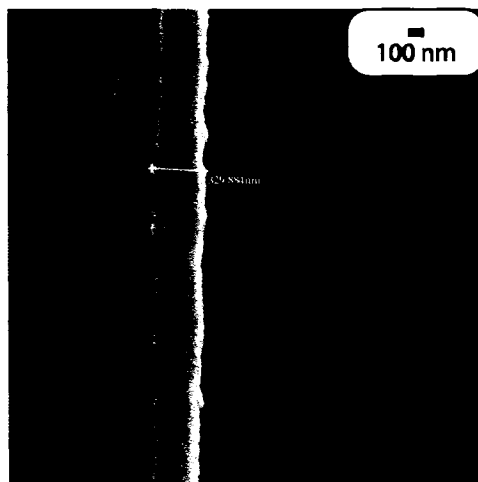


Figure 3.2: SEM image of test mask written in the Nanofab with a *Heidelberg DWL-200*. Nominally patterned  $1\mu m$  feature, which turned out as approx.  $0.35\mu m$ . a large amount of line-edge roughness is visible.

*Heidelberg* could not meet these demands, and consistently displayed lateral offsets when laser-writing continued after a physical movement. Roughness on the photomask transfers through lithographic patterning and ultimately is reflected in the final devices. The stitching errors will persist to create mode-field mismatch points along the length of the waveguide. Due to these problems, the process of creating photomasks in the Nanofab for waveguide applications was deemed a failure, and was not pursued further.

### 3.2.2 Adtek Photomask

Adtek is a commercial photomask company with direct-write laser writing, and direct-write electron-beam systems. The company had, in the past, supplied our group with low-roughness, high-quality photomasks. After the cheaper option of producing masks in the Nanofab was deemed inappropriate, a commercial mask was sought. Adtek seemed the logical choice from which to source a commercial photomask.

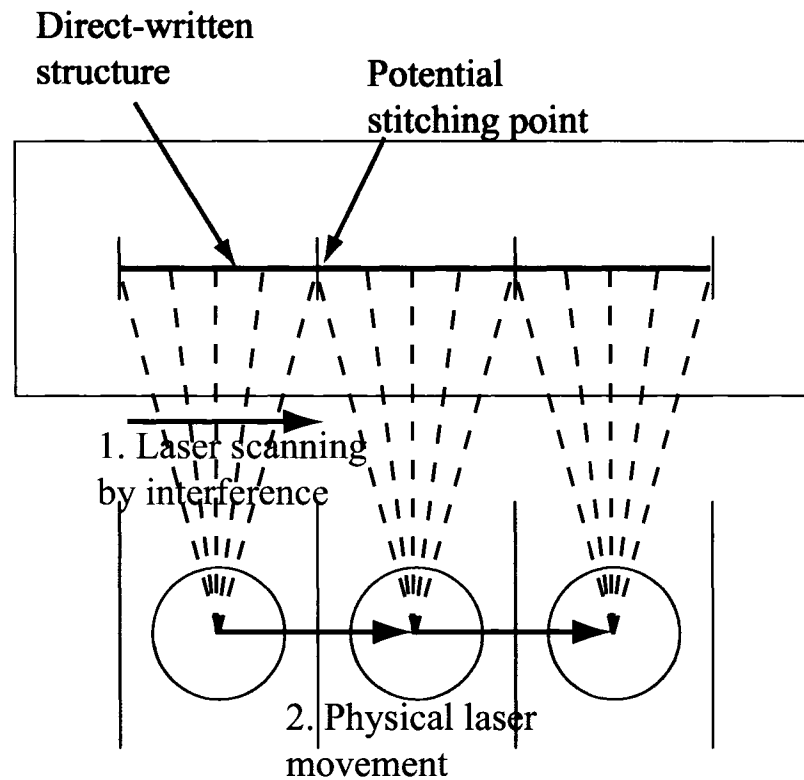


Figure 3.3: A schematic of the setup used for writing masks in the U of A Nanofab. First, structures are written by scanning an interfering laser beam from left to right (1). The interfering laser beam can only scan across a few hundred microns. For structures longer than a few hundred microns, the laser itself must be moved to allow scanning to take place in a new area (2). At the beginning of a new section the laser must begin writing at exactly the same spot that it ended at in the laser writing section. If this is not case, a stitching error may be present. In this figure the laser is shown as being physically displaced, though, typically it is the sample holder which is physically displaced.



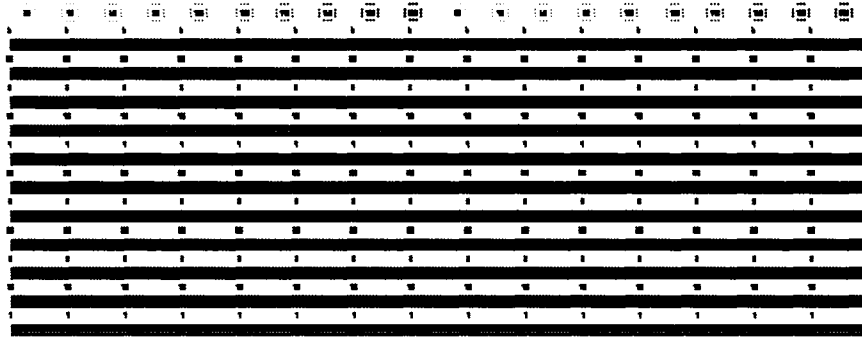


Figure 3.4: A subsection of the design of the photomask from Adtek. The subsection contains 11 sets of waveguides, with 9 waveguides per set. Each set of waveguides has a different width, ranging from  $1\ \mu\text{m}$  to  $6\ \mu\text{m}$  in steps of  $0.5\ \mu\text{m}$ . At the top of the Figure are circular features with diameters ranging from  $20\ \mu\text{m}$  to  $200\ \mu\text{m}$  in steps of  $20\ \mu\text{m}$ . The circular features are intended to be used to pattern microcavities.

## Design

The Adtek photomask was designed in a similar way to the Nanofab mask discussed above. The entire design was done in software from *Ledit*. A 3 inch square design area was selected, suitable for the 4 inch wafers that are typically used in the Nanofab. Groups of waveguides between  $1\ \mu\text{m}$  to  $6\ \mu\text{m}$  were designed in steps of  $0.5\ \mu\text{m}$ . This corresponds to 11 separate size groupings of waveguides. Each of the waveguides was 3 inches in length. Each grouping on this mask contained 9 waveguides separated by  $125\ \mu\text{m}$ . An *Ledit* layout picture of this set of waveguides is shown in Fig. 3.4. The design of the 11 sets of waveguides was twinned on the mask giving a total of 22 groupings of 9 waveguides. A section of waveguides incorporating bends was also designed for this photomask. All bent waveguides had a width of  $4\ \mu\text{m}$ . Straight waveguide sections were connected using S-bend regions of varying lateral offset but fixed horizontal length. The schematic shown in Fig. 3.5 identifies the *lateral* and *horizontal* directions. The horizontal offset was fixed at  $250\ \mu\text{m}$ , and the lateral offset was varied between  $250\ \mu\text{m}$  and  $5000\ \mu\text{m}$ . Thus a design containing 5 sets of 5 waveguides with the offsets

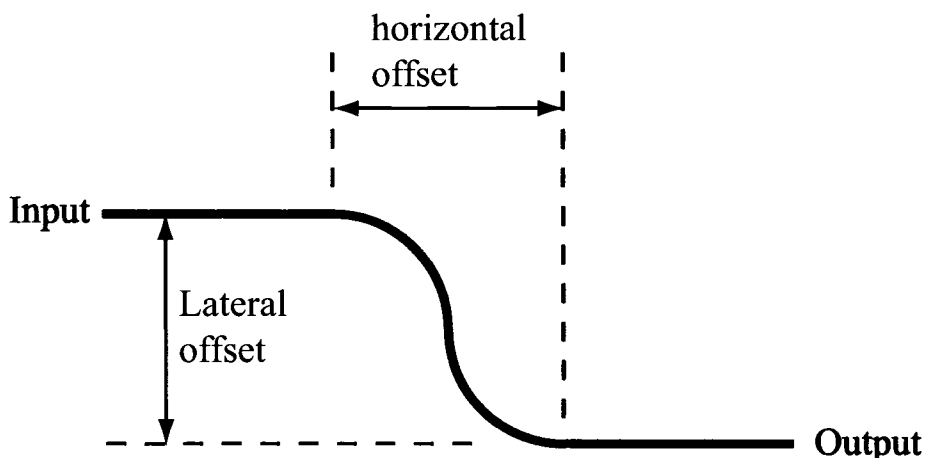


Figure 3.5: A schematic showing a waveguide which contains an S-bend, with a given horizontal and lateral offset.

listed above was created, and was repeated six times on the wafer to give a total of 30 sets of 5 waveguides each. An *Ledit* layout of the bent waveguides is shown in Fig. 3.6. Also included on the mask were circular features, ranging in diameter from  $20\mu m$  to  $200\mu m$ . These structures can potentially be used to fabricate microcavities. An *Ledit* layout of the entire Adtek mask is shown in Fig. 3.7.

### Fabrication

The design file was submitted to Adtek in a GDSII format. The mask was laser-written using a machine from *Ultra*. The mask was returned to our group upon writing completion.

### Fabrication Results

Visual microscopic inspection of the photomask revealed no obvious defects or stitching errors. Photoresist features patterned using the commercial mask were characterized by low line-edge roughness. The circular microcavity looked like a many-sided approximation to a circle. Fig. 3.8 shows a

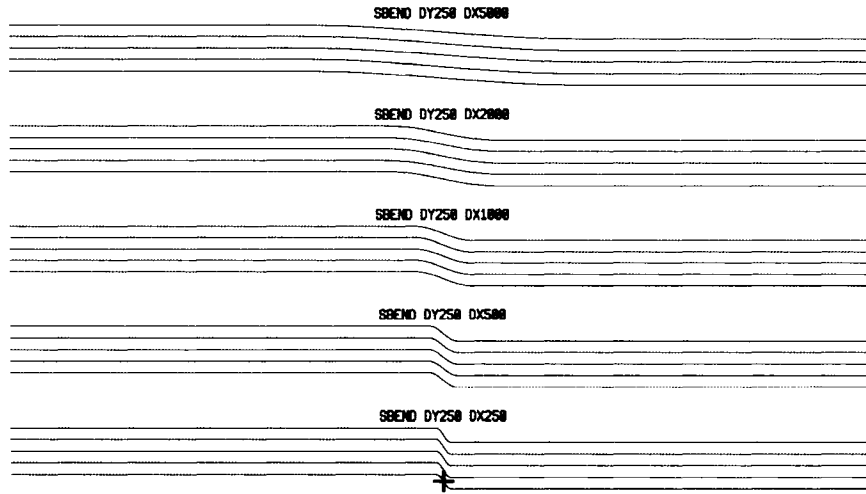


Figure 3.6: A subsection of the design of the photomask from Adtek. The subsection contains 5 sets of 5 waveguides each, all of which are  $4\ \mu\text{m}$  wide. Each set of waveguides has a fixed lateral offset and a horizontal offset between  $250\ \mu\text{m}$  and  $5000\ \mu\text{m}$ .

schematic of a what the microcavity features look like on the photomask.

### 3.3 Successful Fabrication Processes

A variety of approaches were attempted to create waveguides, and both low index contrast and high index contrast waveguides were fabricated. This section is devoted to the fabrication processes that repeatedly produced successful waveguides.

#### 3.3.1 The Silicon Post Prefabrication Method (*SPPM*)

As discussed in the introduction to this chapter, fabrication processes were sought that mitigated the need to chemically etch the SiO core material. The silicon post prefabrication method (*SPPM*) creates two dimensional structure by etching silicon instead of the experimental material (SiO or Er:SiO in this case). An undercladding is deposited, followed by a guiding

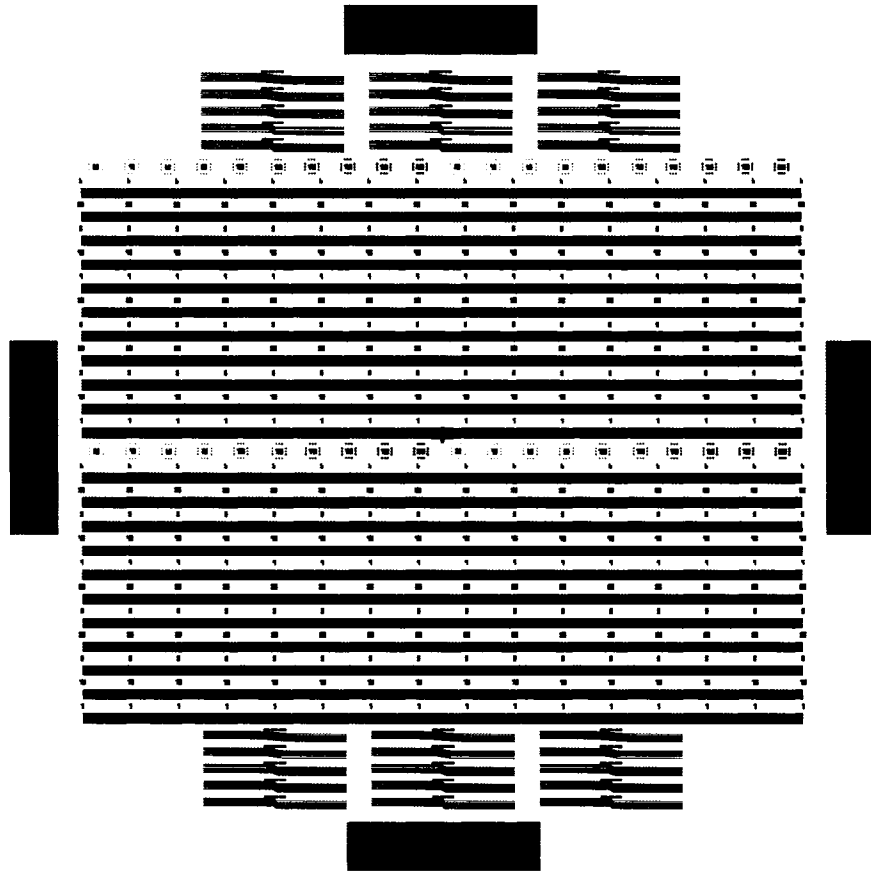


Figure 3.7: The complete design of the photomask from Adtek.

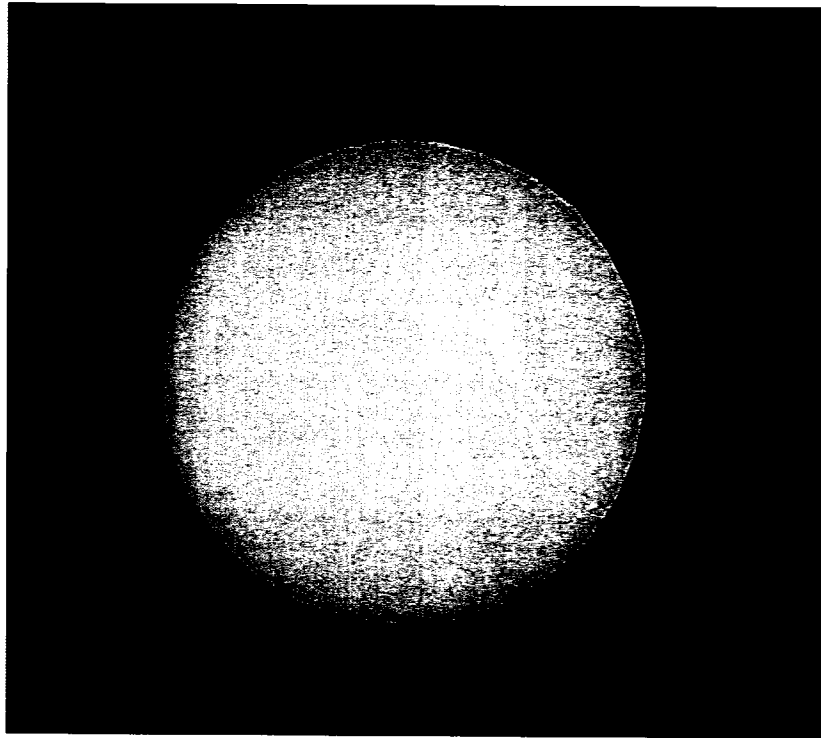


Figure 3.8: A picture of a circular feature which was produced on the Adtek photomask.

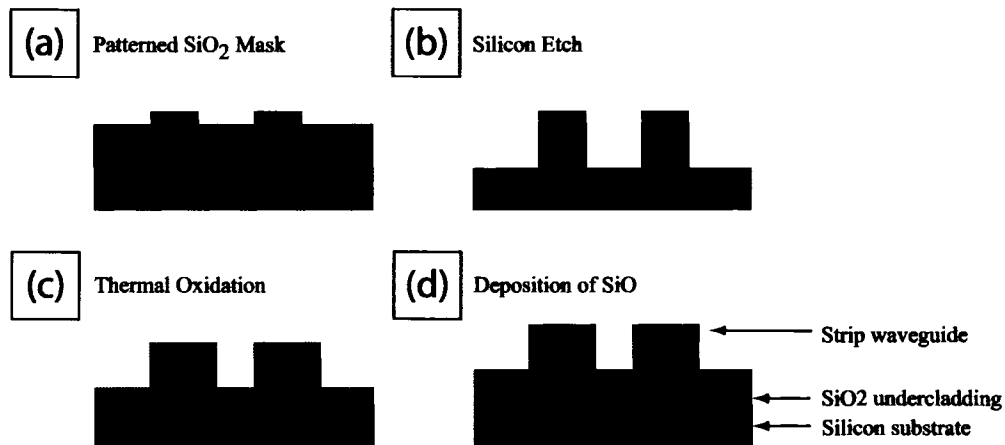


Figure 3.9: A step by step schematic of the major steps involved in the *SPPM* method. (a) A mask of  $SiO_2$  is patterned on top of the silicon substrate. (b) Posts are etched into the silicon substrate using an ICPRIE tool. (c) The entire sample is thermally oxidized to deposit an undercladding of  $SiO_2$ . (d) A layer of SiO is thermally evaporated onto the sample. The directionality of the evaporation plume causes material to be deposited primarily on the top of the post structures and in the trenches between the posts.

layer, creating highly confining strip waveguides. This process produced the highest quality waveguides studied in this work.

### Fabrication

Figure 3.9 shows a step by step schematic of the important steps in the *SPPM* method. Prime grade wafers were first exposed to a standard cleaning process by placing them in a piranha solution, rinsing them with DI water, and drying them in nitrogen with either a spin-rinse-dryer, or by using a dry nitrogen gun (henceforth referred to as *the standard cleaning process*).

A silicon dioxide ( $SiO_2$ ) etch-mask was grown on the silicon wafers by placing them in a furnace with flowing nitrogen and water vapour. A layer of silicon dioxide of approximately 400 nm was grown by thermal oxidation, and the wafers were then cleaned using a standard process of dipping samples in piranha followed by rinsing with de-ionized water and drying with dry nitrogen (for full details of the standard cleaning process see Appendix A.1).

Parameter	Setting
$CF_4$ gas flow	45 <i>sccm</i>
$O_2$ gas flow	5 <i>sccm</i>
Chamber pressure	150 <i>mT</i>
RF power	125 <i>W</i>
Etch time	480 <i>s</i>

Table 3.1: Etching parameters of the Trion *Phantom* RIE used for patterning the  $SiO_2$  ICPRIE etch mask.

Subsequently, a layer of positive photoresist was deposited, patterned, and developed. The portions of the thermal silicon dioxide layer not covered by photoresist were over-etched through to the silicon substrate using a *Trion Phantom* reactive ion etching (RIE) system. The Trion etching recipe used is given in Table 3.1. The remaining photoresist was stripped by first dipping the wafers into acetone, and then applying the cleaning process as above. A schematic of this situation is shown in Fig. 3.9(a).

Immediately prior to silicon etching, the wafers were dipped into a buffered oxide etchant (BOE) for 1 minute to remove native oxide from exposed silicon areas, rinsed, and dried in an SRD. They were placed into an *OXFORD Plasmalab 100* inductively coupled plasma (ICP) RIE system. Process gases consisted of a mixture of oxygen ( $O_2$ ) and sulfur hexafluoride ( $SF_6$ ). Radio frequency power, ICP power, system pressure, and cryo system temperature were all kept constant over all experiments. These parameters are reported in Table 3.2. A schematic of this situation is shown in Fig. 3.9(b). The ratio of the two process gases was used to tailor the sidewall angle of the silicon posts, or to select a region where the undercutting of the silicon dioxide mask would occur. The etching time was used to control the depth of etch, and is a function of the gas ratio used. Fig. 3.10 shows the different structures produced when different ratios of  $O_2:SF_6$  were used. Fig. 3.10(a) used an  $O_2:SF_6$  ratio of 19:200, Fig. 3.10(b) used a ratio of 17:200, and Figure 3.10(c) used a ratio of 13:200.

Parameter	Setting
Temperature	$-110^{\circ}C$
$SF_6$ gas flow	200 <i>sccm</i>
$O_2$ gas flow	13-20 <i>sccm</i>
Chamber pressure	$< 10$ <i>mT</i>
ICP power	500 <i>W</i>
RF power	3 <i>W</i>
Etch time	104-160 <i>s</i>

Table 3.2: Etching parameters of the *OXFORD Plasmalab 100* ICPRIE used for etching posts into silicon.

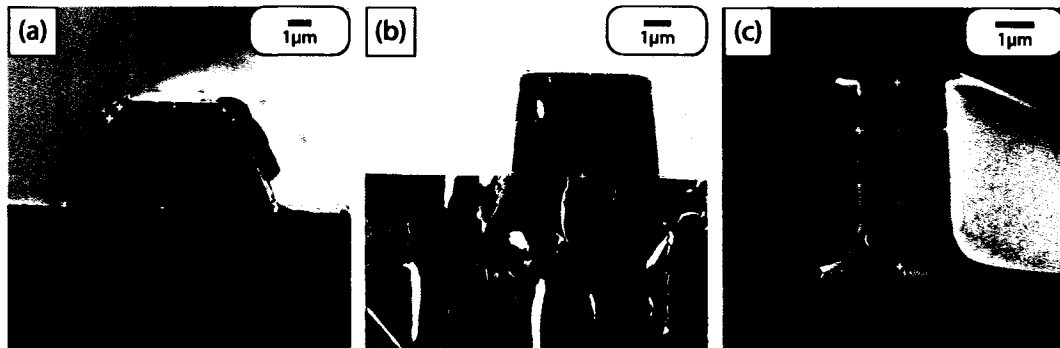


Figure 3.10: *Post* structure etched into a silicon wafer using an inductively-coupled plasma (ICP) reactive ion etching (RIE) system. A process gas ratio of  $O_2:SF_6$  is used to control the sidewall slope. The gas ratio used in (a) was 19:200. The gas ratio used in (b) was 17:200; it produced a steep sidewall as compared with (a). The gas ratio used in (c) was 13:200; it produced undercutting of the silicon dioxide mask.



After the post structure has been etched into the silicon wafers, a suitable undercladding must be deposited. The wafers were cleaned using the standard cleaning process, and undercladdings were deposited on the silicon post structures by either electron-beam (e-beam) evaporation or thermal oxidation. A schematic of thermally oxidized silicon posts is shown in 3.9(c). Fig. 3.11 shows electron microscope images of undercladdings deposited by e-beam evaporation and wet thermal oxidation. Fig. 3.11(a) shows a profile view of an undercladding deposited by e-beam evaporation. The undercladding was deposited on top of a silicon post similar to that in Fig. 3.10(c). The rounded deposition profile is likely due to a broad angular range of silicon dioxide flux. The average flux direction in the profile-plane can be estimated from the shadowing effects seen in the slab waveguides created at the bottom of the post structure. If the average flux direction in the profile-plane is not normal to the substrate, the undercladding layer will be non-symmetric. Fig. 3.11(b) shows an oblique angle view of fig. 3.11(a). Roughness is apparent on the sides of the undercladding. The roughness will follow the trend imparted by the silicon etch, and may also be caused by some structure created by glancing-angle deposition.

Fig. 3.11(c) shows a profile view of an undercladding deposited by wet thermal oxidation of the silicon post structure. The *lip* visible on the top of the undercladding structure is an artifact of leaving the silicon dioxide ICPRIE etch mask on top of the etched silicon post during wet thermal oxidation. by visual inspection of the electron microscope images, the thermal oxidation provides smoother undercladding features, which may be due to the roughness-reducing nature of isotropic processes. Fig. 3.11(d) shows a tilted angle view of Fig. 3.11(c). Roughness is visible on the sidewalls of the silicon post, but the lip region and the edges of the lip features are apparently very smooth. The undercladding deposited by wet thermal oxidation is symmetric.

Once an appropriate undercladding had been deposited, a guiding layer

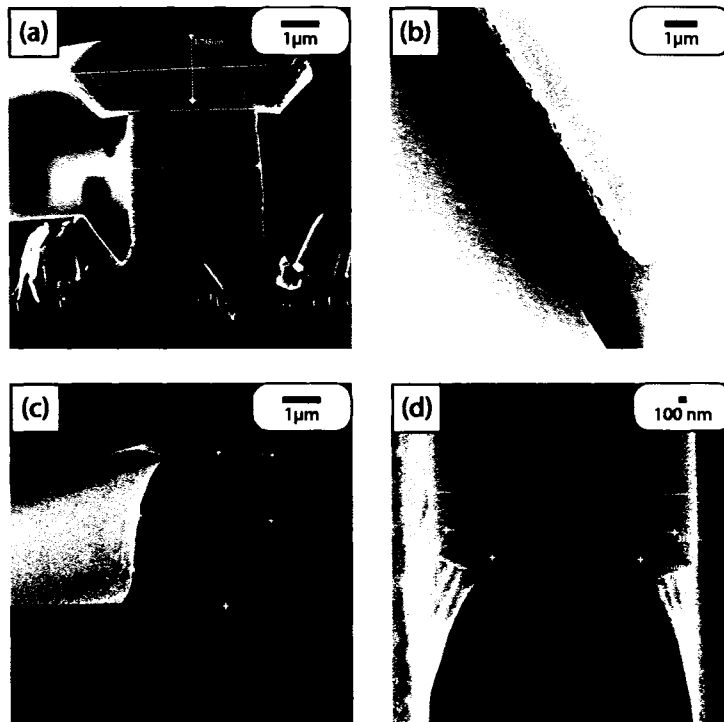


Figure 3.11: Silicon dioxide undercladdings deposited by two separate methods. (a) A profile view of an undercladding deposited by electron-beam evaporation on a silicon post etch structure similar to that in Fig. 1(c). (b) Oblique angular view of structure from (a) emphasizing the apparent roughness at the undercladding edge. (c) A profile view of an undercladding deposited by wet thermal oxidation. of interest is the *lip* feature that develops by leaving the silicon dioxide etch mask in place. (d) Oblique angular view of (c) showing smoother edge features as compared to (b).

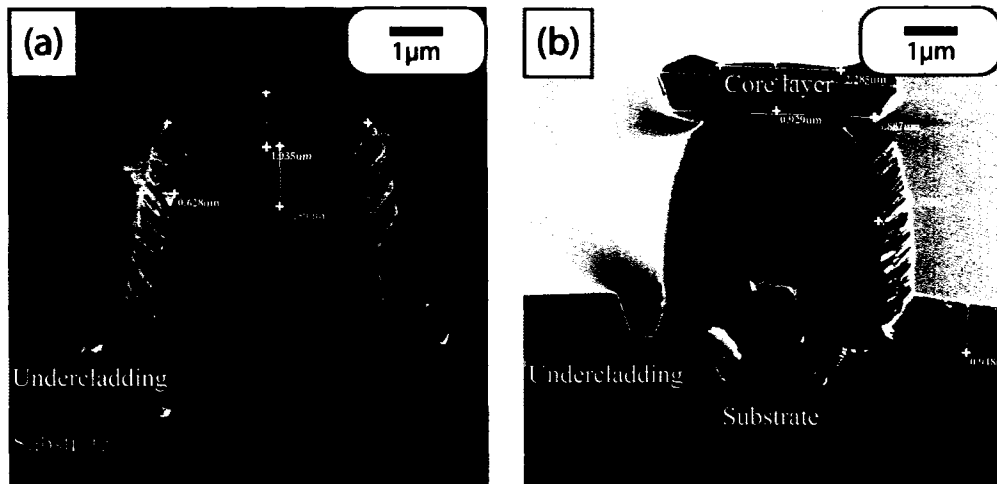


Figure 3.12: Waveguiding layers deposited during the *silicon post prefabrication method* onto undercladdings grown by wet thermal oxidation. Layers were deposited by either thermal evaporation of silicon monoxide, or by concurrent thermal evaporation of silicon monoxide and electron beam evaporation of erbium oxide. (a) A silicon monoxide layer deposited onto an undercladding with no *lip* feature. (b) An erbium-doped silicon monoxide layer deposited onto an undercladding with *lip* feature. The undercladding layers are similar to that shown in Figs. 3.11(c) and 3.11(d).

was deposited. Wafers were cleaned by the standard process, and guiding layers of either silicon monoxide (SiO) or erbium-doped silicon monoxide (SiO:Er) were subsequently deposited on top of the appropriate undercladdings. All of the SiO materials used in this thesis were deposited by the group of Al Meldrum in the Department of Physics. SiO was deposited by thermal evaporation, and SiO:Er by concurrent thermal and electron beam evaporation techniques of silicon monoxide and erbium oxide respectively. The deposition rates of the separate materials were monitored using separate crystal-thickness monitors. The erbium source has recently been switched to erbium metal to improve deposition consistency. A schematic of a strip waveguide formed on top of a thermally oxidized silicon post sample is shown in Fig. 3.9(d). The rates of evaporation were adjusted to target films with approximately 1 atomic percent erbium. Fig. 3.12 shows the resulting structures created by guiding layer deposition. All guiding layers have

been deposited on wet thermally oxidized undercladdings. The waveguides do not coat the undercladdings conformally. This is believed to be caused by a broad angular range of flux deposition, similar to that described above for e-beam deposited silicon dioxide undercladdings. Fig. 3.12(a) shows a profile view of a thermally oxidized silicon post with a waveguiding layer of silicon monoxide deposited on top. In this case, the core material covered both the sidewalls equally. This apparently indicates that the net average direction of flux, projected onto the profile plane, was approximately normal to the substrate plane. Fig. 3.13(a) shows a profile plane view of a waveguide schematic. Fig. 3.13(b) shows the a three-dimensional view of a waveguide schematic. For symmetric deposition on the sidewalls of a waveguide,  $\theta$  in Fig. 3.13(b) must be zero. Fig. 3.12(b) shows a profile view of a thermally oxidized silicon post with a waveguiding layer of erbium-doped silicon monoxide deposited on top. The direction of net flux deposition in the profile plane in Fig. 3.12(b) is believed to be from right of normal since the core material only coated the right-hand side of the *post* structure. Waveguides deposited in this manner might have non-symmetric mode profiles. However, note that the intended strip waveguide region is well isolated from the core material on the sidewalls in this latter case.

After deposition of a guiding layer of either SiO or SiO:Er, the structures were cleaned by the standard cleaning process, and exposed to a standard annealing treatment of 1 hour at 500 °C in an atmosphere of 5%:95%  $H_2:N_2$  (henceforth referred as *the standard annealing process*).

Finally, some of the waveguide samples were coated with an upper cladding of benzocyclobutene (BCB) polymer to reduce losses due to scattering and to protect the waveguides from environmental damage. The BCB was spun-cast onto the finished structures, and cured. Fig. 3.14 shows a waveguide with an upper cladding of BCB deposited on it. After fabrication, wafers were cleaved in order to test waveguides.

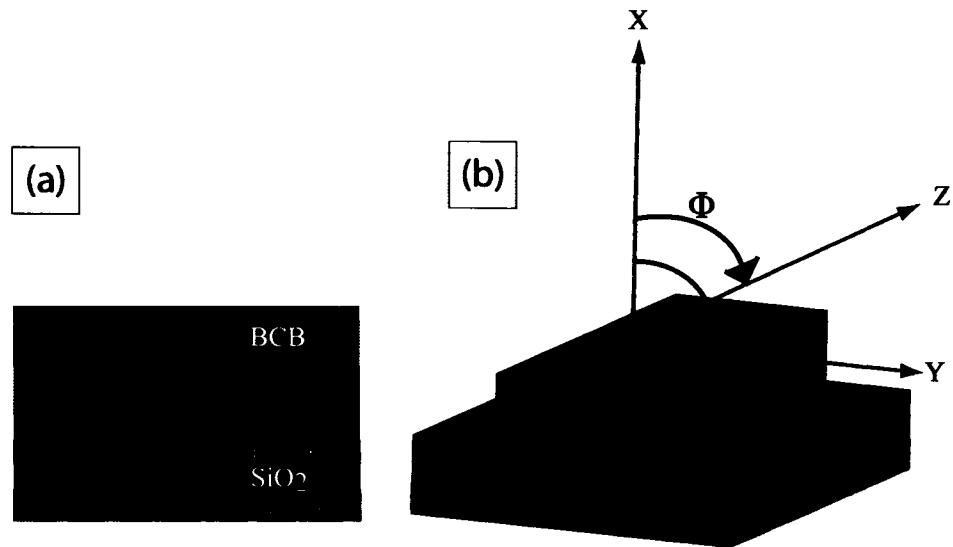


Figure 3.13: (a) A schematic of a completed buried strip waveguide with an upper cladding. Viewed in the waveguide's profile plane. (b) a 3D view of a strip waveguide. The flux direction in the evaporation system will have angles  $\theta$  and  $\phi$ . For symmetric deposition on the waveguide sidewalls,  $\theta$  must be zero.

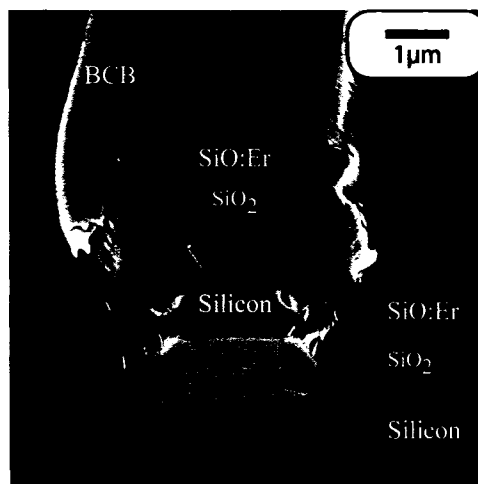


Figure 3.14: profile view of a completed waveguide structure from the silicon post prefabrication method with an upper cladding of benzocyclobutene (BCB).

## Fabrication Results

In some cases, the *SPPM* produced high quality strip waveguides with high modal confinement. The results, however, were not completely consistent. Even on the same chip, some of the waveguides exhibited low loss values, while others did not. It is important to analyze each stage of the process to identify problems that might contribute to waveguide scattering loss, which is one of the key challenges in the development of experimental waveguides.

In the *SPPM* there are three identifiable sources of roughness. The first is the roughness on the sidewall of the  $SiO_2$  ICPRIE etch mask used in the silicon post etching step. The second source is roughness arising from the ICPRIE silicon dry etching process. The third source of roughness occurs when the guiding layer is deposited onto the structure. Glancing-angle deposition of the core material seems to create a highly porous structure on the sidewalls of the posts.

The roughness begins during the photoresist process, and is exacerbated by the RIE process used to pattern the  $SiO_2$  ICPRIE etch mask. The line-edge roughness of the photoresist process was typically only a few nanometers, but the sidewall profile of the standard photolithography process has a large amount of stepping and striation as shown in Fig. 3.15. In an anisotropic RIE process where the etch rates of the masking material and the material to be etched are comparable, the sidewall pattern will transfer into the etched material below. In the specific case of RIE etching of the  $SiO_2$ , the etch rates of the  $SiO_2$  and the masking material are similar, and so roughness transfers readily to the  $SiO_2$  masking layer. Thus, it is likely that the  $SiO_2$  ICPRIE etch mask will have relatively low line-edge roughness and a poor sidewall, as is the case with the photoresist profile.

The subsequent step was the ICPRIE etch of the underlying silicon. The etch ratio of silicon to  $SiO_2$  in the silicon cryo process used is very high, on the order of 500:1. In a region where no undercutting occurs, the silicon etch will likely follow the line-edge of the silicon dioxide, given that a targeted

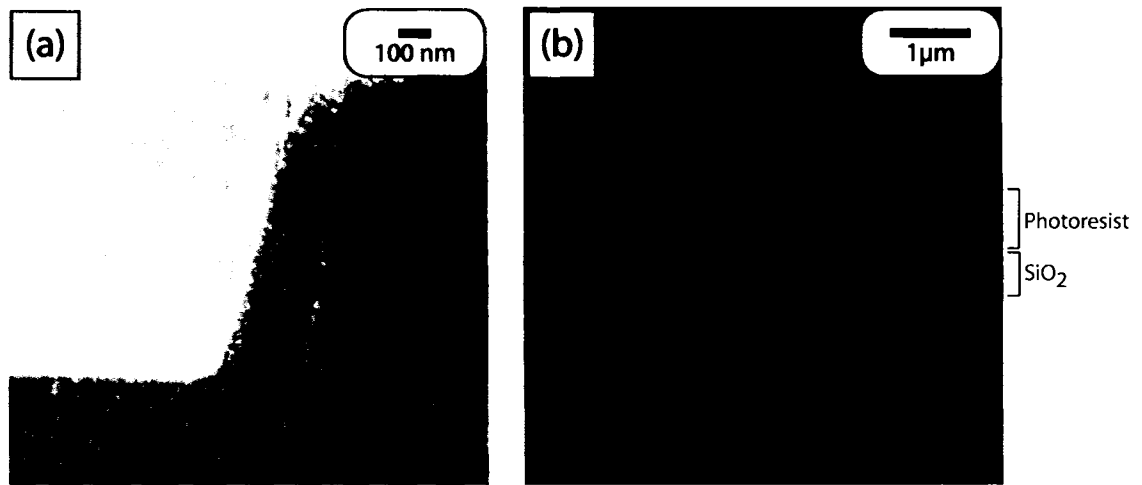


Figure 3.15: SEM images showing examples of the how patterns in the sidewall of a photoresist profile will transfer to silicon dioxide during RIE. (a) profile view of an etched  $\text{SiO}_2$  rib; the break between the photoresist and  $\text{SiO}_2$  layers is visible near the top of the image. Visible roughness on the sidewall appears seamless, with nothing to distinguish the different materials besides the height of each of the apparent *steps*. (b) Oblique-angle view of the sidewall of a rib etched into  $\text{SiO}_2$  with the photoresist etch mask remaining. Roughness transfer from the photoresist to the  $\text{SiO}_2$  is clearly visible. The only indication of the interface between the materials is the change between step heights, the larger step height is representative of etched  $\text{SiO}_2$ .

silicon etch depth of  $5\mu\text{m}$  would only etch 10 nm down into the  $\text{SiO}_2$ . Thus, a tentative conclusion for the roughness on the silicon walls is that it persists from the line-edge roughness of the photoresist process. It can further be concluded that improving both the line-edge roughness of the photoresist profile along with the sidewall smoothness of the photoresist profile would help to reduce the amount of scattering in the completed waveguides.

The third source of scattering, that from the deposition of the guiding layer, occurs due to the deposition of a porous material on the sides of the silicon wall. From SEM images (see Fig. 3.13(a)), this seemingly results in increased striation at the edges of the strip waveguide itself. To reduce this effect, it is likely necessary to restrict angular range of the material flux to lower values, and to center the flux source so that the net flux direction in the profile plane of the waveguides is normal to the substrate surface.

Another potential problem with having the net flux direction in the waveguide profile plane off-of-normal to the substrate is that there will be a thickness gradient across the width of the waveguide. This will create a graded effective index situation across the width of the waveguide, pushing the center of the mode profile towards one of the edges of the strip waveguide. A mode profile nearer to the edges of the waveguide will allow for an increased amount of modal power to interact with each of the aforementioned forms of sidewall roughness, increasing the optical losses due to scattering. It is interesting to note that the two batches of waveguides that yielded low optical loss results had a fairly symmetric deposition. Those that have had a visibly non-symmetric deposition produced higher loss waveguides. Examples of symmetric depositions are shown in Fig. 3.12(a) and Fig. 3.14. An example of non-symmetric deposition is shown in Fig. 3.12(b).

### 3.3.2 The Silicon Dioxide Ribload Process

The silicon dioxide ribload process (henceforth known as  $\text{SiO}_2\text{-RL}$ ) started off with much the same intent as the the silicon post prefabrication pro-



cess from Section 3.3.1 above. The ribload process permits the fabrication of waveguides with minimal processing of experimental materials. In the present case it was desired to avoid the need to etch rare-earth ion doped SiO systems such as erbium-doped SiO (Er:SiO) and neodymium-doped SiO (Nd:SiO). The ribload structure provides relatively low lateral index contrast. Given a high vertical index contrast, only a small portion of the mode will interact with the etched sidewalls of the waveguides. Thus, it was hoped that fabrication-induced scattering losses would be low.

### **Fabrication**

Silicon wafers of orientation  $\langle 100 \rangle$  were cleaned using the standard cleaning procedure of dipping in piranha, rinsing in DI water, and drying with either a nitrogen gun or a spin-rinse dryer. Wafers were then placed in a furnace (Minibrute) for wet thermal oxidation. The wafers were heated to a temperature of  $1040^\circ\text{C}$  while both water vapor and nitrogen were passed through the furnace area. The wafers were left for approximately 16 hours, providing an  $\text{SiO}_2$  undercladding thickness of greater than  $2\mu\text{m}$ . The standard cleaning procedure was again applied, after which a  $1\mu\text{m}$  layer of either SiO or Er:SiO was deposited on top of the undercladdings. SiO was deposited by thermal evaporation, while Er:SiO was deposited by concurrent thermal evaporation of SiO and electron-beam (e-beam) evaporation of erbium oxide ( $\text{Er}_2\text{O}_3$ ). The wafers were again treated with the standard cleaning process, and then subjected to the standard annealing process of 1 hour at  $500^\circ\text{C}$  in an atmosphere of  $\text{H}_2:\text{N}_2$  at a ratio of 5:95. The furnace could handle a maximum sample diameter of 2 inches. Thus, 4 inch wafers were cleaved into quarter-wafers prior to annealing. After annealing, a  $600\text{nm}$  layer of  $\text{SiO}_2$  was deposited on quarter-wafers. Two methods were tested for depositing the  $\text{SiO}_2$ . The first method was deposition via thermal evaporation of bulk  $\text{SiO}_2$ . The second method was deposition via plasma-enhanced chemical vapour deposition (PECVD) of a mixture of tetraethylorthosilicate (TEOS),

Parameter	Setting
Temperature	300°C
TEOS gas flow	100 sccm
O <sub>2</sub> gas flow	85 sccm
Chamber pressure	1015 mT
RF power	40 W
Deposition time	600 s

Table 3.3: PECVD silicon dioxide deposition parameters used in the  $SiO_2 - RL$  process.

and oxygen ( $O_2$ ) as precursors. The process was inherent to the equipment, and only the time of deposition was controllable. The deposition parameters are listed in Table 3.3. The deposition rate was approx. 1 nm per second. A deposition time of 600 seconds was consistently used. The wafers were exposed to the standard cleaning process before being placed in an oven for deposition of hexamethyldisilazane, a photoresist adhesion promoter. Following this step, the mask described in Section 3.2.2 and positive-tone photolithography were used to pattern the wafer. After photoresist developing, the quarter-wafer was placed into a bath of a buffered oxide etchant (BOE) for 8 minutes, and then carefully rinsed with DI water. The patterned photoresist strips were then removed by first dipping the wafer in acetone, followed by applying the standard cleaning process. Waveguides of different lengths were attained by cleaving the quarter-wafers into chips of various sizes.

### Fabrication Results

To assess the potential of this process, a layer of  $SiO_2$  was deposited onto a plain silicon wafer, standard photolithography was used to pattern thin strips on top of the  $SiO_2$ , and the  $SiO_2$  was etched using BOE. Figure 3.16 is an SEM image showing the extremely smooth sidewalls of the etched  $SiO_2$  on silicon. Based on the knowledge that it was possible to pattern smooth features this way, the process was subsequently attempted on top of thin films of SiO. Fabrication runs were performed with  $SiO_2$  loading layers

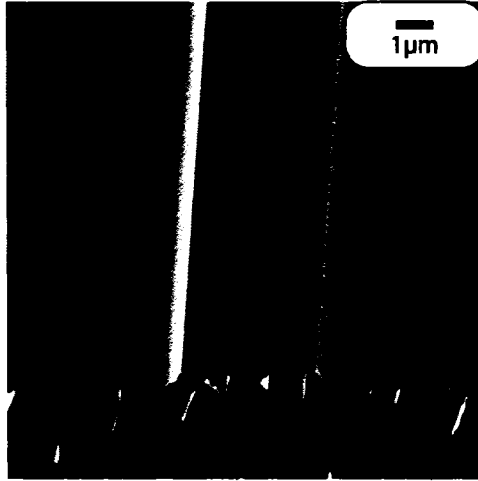


Figure 3.16: SEM image showing the results of etching a layer of  $SiO_2$  deposited by PECVD onto silicon using standard photolithography and BOE etching.

deposited by either thermal evaporation or PECVD. However, the thermally evaporated  $SiO_2$  was found to be porous and resulted in poorer etching results, so was not pursued further. Fig. 3.17(a) shows a profile view of one of the resulting ribloaded waveguides using PECVD  $SiO_2$  for the rib. Fig. 3.17(b) shows a magnified view of the sidewall striations of the ribloaded waveguide in fig. 3.17(a)

### 3.3.3 The SU8 Electron-Beam-Resist Stripload Process

The SU8 electron-beam-resist stripload process (henceforth the *e-beam SU8* process) is a slight variation on the  $SiO_2$ -RL process from Sec. 3.3.2. This process provides 2D confining waveguides by using the vertical index of refraction offset nascent to slab waveguides, and creates effective horizontal index of refraction confinement by patterning thin strips of the SU8 electron-beam-resist on top of the slab waveguide. The SU8 was patterned by exposing it to i-line UV radiation ( $\lambda \sim 365$  nm) through a standard mask such as that

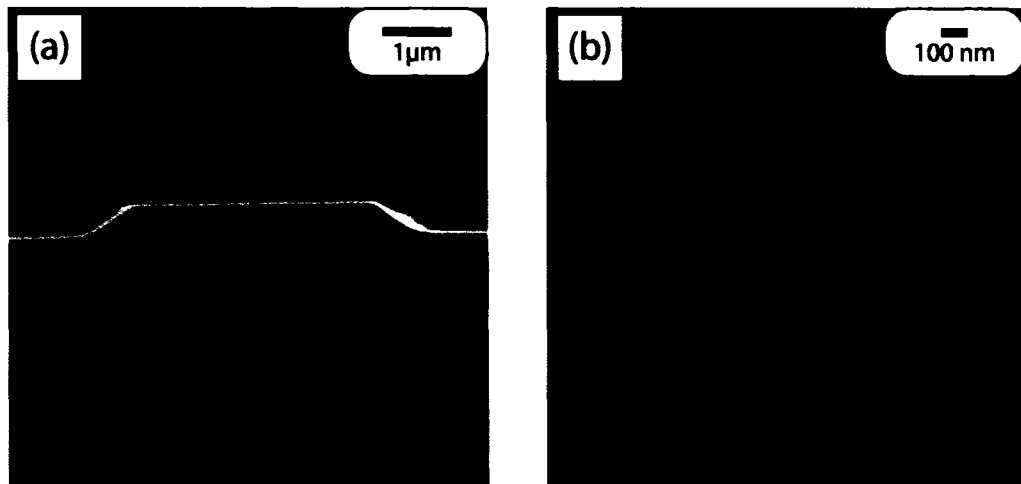


Figure 3.17: (a) Profile view of a completed ribloaded waveguide. (b) A view of the sidewall of the waveguide shown in (a). The sidewalls appear fairly smooth.

described in Sec. 3.2.2. Compared to the  $SiO_2$ -RL process, the SU8 process has the advantage of requiring less fabrication steps, providing less chance for process failure. This process should also allow for exact replication of the mask features, which is an improvement over the processes of Sec. 3.3.1 and Sec. 3.3.2.

### Fabrication

Fabrication of the undercladding and core layers of the structure are the same as in Sec. 3.3.2. Following deposition of the core layer, samples were annealed, cleaned, and then had a layer of e-beam SU8 (SU8 - 2000) spun onto them. The spin speed was approx. 1000 *rpm* and the resulting layer thickness was approx. 15 *nm*. The SU8 was patterned using i-line UV light, and the unexposed portions were etched away in an appropriate developing solution. The samples were subsequently cleaved to produce waveguides of varying lengths.

## Fabrication Results

The SU8 resist formulation used in this process was originally developed for patterning with a focused electron beam. The first part of this project focused on validating the ability to pattern this formulation of SU8 with standard i-line photolithography. This was shown to be successful experimentally. The complete process was executed, and 2D waveguides were successfully fabricated. Originally the resist was thought to spin to a thickness of  $\sim 150$  nm, though, measurements using a contact profilometer showed that the resist layer is only  $\sim 15$  nm in thickness. This thickness does not provide a large amount of lateral index confinement, which could make waveguides from this process sensitive to small variations in surface quality or even surface cleanliness.

## 3.4 Failed Fabrication Processes

Several processes attempted during this project were deemed as failures because they did not produce low loss waveguides. Though they did not produce the designed result, these failures provide useful information, and this information can be useful in guiding future processes. This section documents these failed fabrication processes and explores the likely reasons behind their failures.

### 3.4.1 Commercial PECVD Undercladdings

The required undercladding thickness for the given index contrast was studied for proper waveguide design (see Sections 2.3.2 and 4.3). Originally, an undercladding thickness of approx.  $3 \mu\text{m}$  was believed to be required for proper modal isolation. A commercial order for  $3 \mu\text{m}$  thick layers of  $\text{SiO}_2$  on silicon substrates was placed.

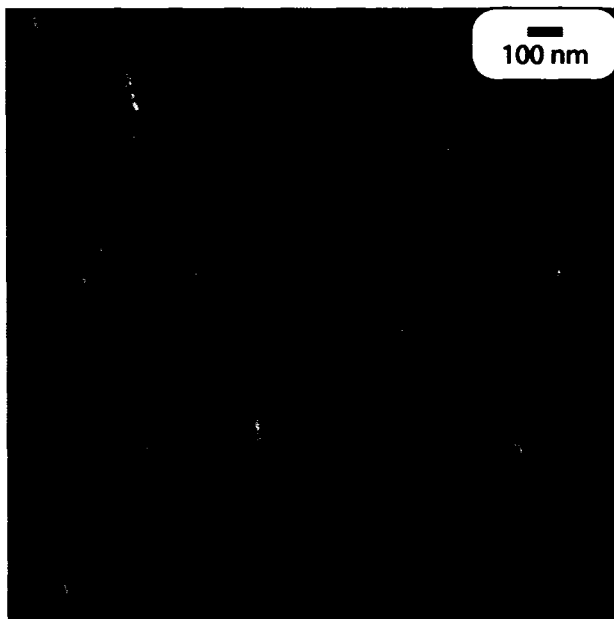


Figure 3.18: SEM image of the surface of commercially purchased  $SiO_2$  undercladdings. The visible roughness will lead to interfacial scattering.

### **Fabrication**

$3\ \mu m$   $SiO_2$  thick undercladdings were fabricated using PECVD and delivered to TRILabs. Layers of SiO and Er:SiO were deposited onto the commercial undercladdings and 2D waveguides were fabricated.

### **Fabrication Results**

Poor propagation losses were typical of waveguides fabricated on commercial PECVD undercladdings. A high resolution visual inspection of the undercladding surfaces using SEM was conducted, and found large amounts of roughness. The roughness likely caused high levels of interfacial scattering losses. An SEM image of a typical surface is shown in Fig. 3.18.

### 3.4.2 Direct Etching of SiO and Er:SiO with BOE

The most obvious process to begin patterning of SiO and Er:SiO was to attempt etching with BOE. BOE etching with a photoresist mask is a standard method of patterning silicon-oxygen glasses. The goal of the process was to transfer patterns into SiO and Er:SiO by first patterning negative-tone photoresist, and exposing the glass to BOE.

#### Fabrication

Deposition of undercladding and core layers are consistent with the approach of Sec. 3.3.2. The structure was exposed to the standard annealing process (see appendix A for standard process description). The structure was again cleaned, and a layer of negative-tone photoresist was spun onto the sample. The photoresist was patterned with a negative-image photomask, leaving a positive image of photoresist on top of the experimental material. The sample was then placed in BOE for differing lengths of time. The photoresist was removed using a two-step procedure of first exposing the photoresist to acetone, and by following this by applying the standard cleaning process.

#### Fabrication Results

It was found that both the SiO and Er:SiO could be etched using the BOE process. Figure 3.19 shows a top-view and a profile-view of typical waveguides produced via this process. Test etching of experimental materials before and after annealing revealed different etch rates. The etching rates of annealed SiO, and annealed Er:SiO were 3.7 *nm* per minute, and 3.0 *nm* per minute, respectively. Further, more uniform etching characteristics were achieved after annealing. Though etching in BOE was successful, material quality after etch was poor, and inconsistent. Problems ranged from large numbers of visible micron scale pinholes, to large area roughness with no identifiable cause. Given the poor material quality after etching, this process was deemed

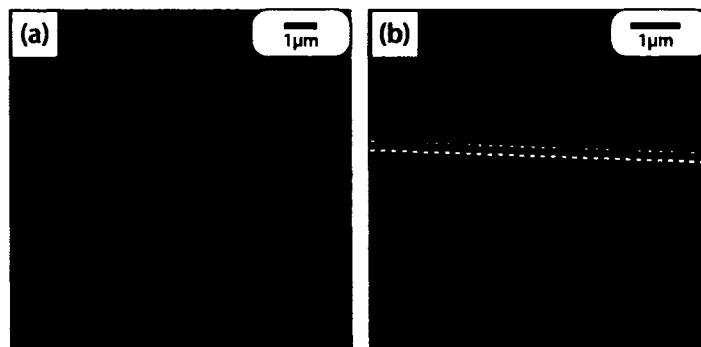


Figure 3.19: (a) Top-view of an as-deposited SiO waveguide produced by patterning with a negative tone photoresist and etching with BOE for 60 minutes. (b) Profile-view of an SiO waveguide produced by patterning with a negative tone photoresist and etching with BOE for 25 minutes. The dashed lines have been added for clarity to show the height of the etch.

a failure.

### 3.4.3 Rib Waveguide Fabrication by Dry Reactive Ion Etching

Another obvious process to attempt was the direct dry etching of SiO and Er:SiO. Good results are routinely demonstrated in direct patterning of  $SiO_2$  using this technique.

#### Fabrication

Silicon wafers with  $SiO_2$  undercladdings were cleaned by the standard cleaning method, and a layer of SiO was deposited onto the sample by the standard deposition method described in Sec. 3.3.1. The samples were cleaned, exposed to the standard annealing treatment, and cleaned once again. The samples were exposed to HMDS, and patterned with a positive tone photoresist, (HPR-504), using a Nanofab-supplied photomask. The samples were placed into a *Trion Phantom* RIE, and etched with either  $CF_4$  or a mixture of  $CF_4$  and  $O_2$  to remove any redeposited photoresist. Etch times were set



Parameter	Setting
$CF_4$ gas flow	45 <i>sccm</i>
$O_2$ gas flow	0 or 5 <i>sccm</i>
Chamber pressure	150 <i>mT</i>
RF power	125 <i>W</i>
Etch time	180 <i>s</i>

Table 3.4: Etching parameters of the Trion *Phantom* RIE used for directly patterning SiO.

at 3 minutes. The process parameters are given in Table 3.4. Samples were removed from the RIE, and had remaining photoresist removed by first dipping the samples in acetone, followed by application of the standard cleaning recipe. Samples were cleaved to exposed cross-sectional views for SEM

### Fabrication Results

SEM images of the etched features reveal roughened surfaces in each area exposed to process gases. Sidewall roughness was significant, though, the stepping profile evident in Fig. 3.20 suggests that the roughness and shallow sidewall angle persist from the photoresist profile much the same as in Fig. 3.17. The rough bottom surface is likely indicative of high power bombardment, or resputtering of photoresist, and subsequent micromasking due to the resist. Due to both sources of roughness, this method was deemed a failure.

#### 3.4.4 Rib Waveguides Produced by Direct Etching with KOH

After it was determined that BOE was not an appropriate wet etchant for SiO, wet etching using potassium hydroxide (KOH) was attempted. This process is more complicated than that for BOE because KOH etches photoresist quickly. Thus, photoresist cannot be used as an effective masking layer. A mask made of silicon nitride was used instead.

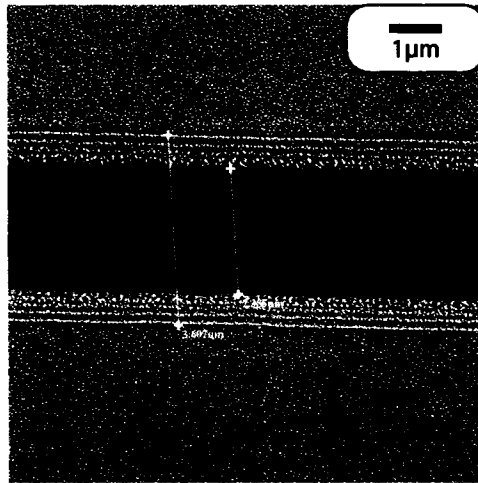


Figure 3.20: Top-view of a waveguide produced by reactive ion etching of SiO with a positive-tone photoresist mask. A rough bottom surface is evident, likely due to high-energy ionic bombardment. The sidewall of the waveguide is very rough, and shows a *stepping* profile similar to that of Fig. 3.17, and attributed to stepping in the photoresist profile.

### Fabrication

Layers of SiO and SiO:Er were deposited on top of cleaned thermal  $\text{SiO}_2$  undercladdings, and were subjected to standard cleaning and annealing techniques. A thin (approx.  $100\text{nm}$ ) layer of silicon nitride was deposited by PECVD, and subsequently cleaned and exposed to HMDS. A layer of positive-tone (*HPR-504*) photoresist was spun-cast, patterned, and developed using a mask prepared in the Nanofab. The silicon nitride layer was etched in a *Microetch* RIE using  $\text{CF}_4$  process gas. Excess photoresist was removed by first dipping samples in acetone followed by exposure to the standard cleaning treatment. Thus, a patterned layer of silicon nitride remains on top of a layer of SiO or SiO:Er. A swirling bath of KOH was heated to approx.  $95^\circ\text{C}$ , and the samples were placed in the baths for differing lengths of time. Samples were removed, and dipped in water to try to remove any residues from the KOH bath. No suitable wet etchant could be found to remove the silicon nitride, so the remainder of the mask was exposed to the

same dry etching treatment as was used to pattern the silicon nitride layer. The SiO or SiO:Er layer was roughened due to the dry etching, so the KOH bath was prepared again, and the the samples were placed into the KOH bath to try to smooth out surface roughness. The samples were removed from the KOH after approx 5 minutes, and dipped in water for approx. 30 minutes to try to remove KOH residues. Finally, samples were cleaved for SEM analysis.

### **Fabrication Results**

Waveguide fabrication by the aforementioned method seemed reasonably successful, producing relatively low apparent sidewall roughness, as shown in Fig. 3.21(a). However, several regions of the samples revealed contamination from the KOH bath, as shown in Fig. 3.21(b). The low sidewall roughness was achieved even with use of a Nanofab written mask. Unfortunately, subsequent attempts at the process produced low quality waveguides with high losses. These subsequent attempts used  $3\mu m$  thick PECVD  $SiO_2$  undercladdings produced by Micralyne as opposed to undercladdings produced by thermal oxidation. Further inspection of these undercladdings revealed high rms surface roughness (see Sec. 3.4.1) which may have played a major role in persistent sidewall roughness as well as interface roughness. It was also difficult to maintain a constant repeatable temperature using the Nanofab's KOH setup. This was a problem because the material etch rates are a strong function of KOH temperature. Because of the inability to control various aspects of this process, along with the failure of waveguide fabrication upon successive attempts, this process was deemed a failure.

### **3.4.5 The Metal Liftoff Process**

Patterning of metal layers was attempted in the Nanofab using the liftoff process. A schematic of the process is shown in Fig. 3.22. Briefly, a layer

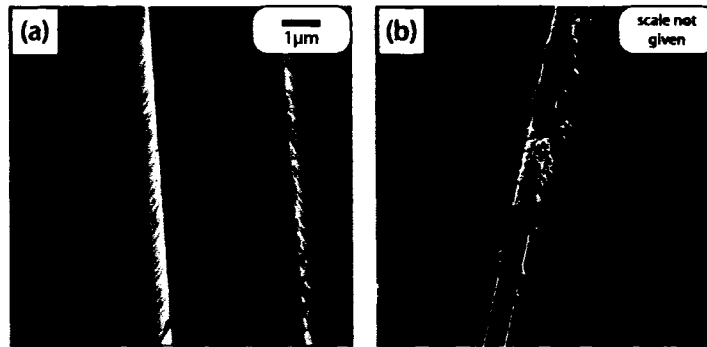


Figure 3.21: (a) Oblique angle view of a strip waveguide produced by KOH etching with a silicon nitride mask. Roughness levels seem low, and the break between guiding layer and undercladding layer is faintly visible as a shading contrast on the sidewalls of the waveguide; the material break is indicated by the orange bar on the figure. (b) Oblique angle view of a waveguide with some form of deposit native to the KOH etching bath. The deposit creates a large amount of roughness, which will be detrimental to waveguide performance.

of photoresist was patterned (Fig. 3.22(a)) on top of a silicon dioxide layer. A layer of chrome was deposited on top of the photoresist and also filled the trenches between the photoresist (Fig. 3.22(b)). The patterned photoresist was stripped, leaving only a chrome mask (Fig. 3.22(c)). The  $SiO_2$  was then etched using RIE (Fig. 3.22(d)). This process was used to attempt the fabrication of  $SiO_2$  ribloaded waveguides.

### Fabrication

Silicon wafers with  $3\mu m$  thick PECVD  $SiO_2$  layers were cleaned and had a layer of Er:SiO deposited. The sample was cleaned and exposed to the standard annealing treatment. The sample then had a layer of  $SiO_2$  grown onto it by PECVD. It was again cleaned, exposed to HMDS, and patterned using positive-tone (HPR-504) photoresist and a negative mask produced by Adtek (a mask designed prior to this thesis). The sample was next placed into a sputter system, where a thin layer of chrome was deposited. The remaining photoresist was removed by ultrasonic agitation of the sample in

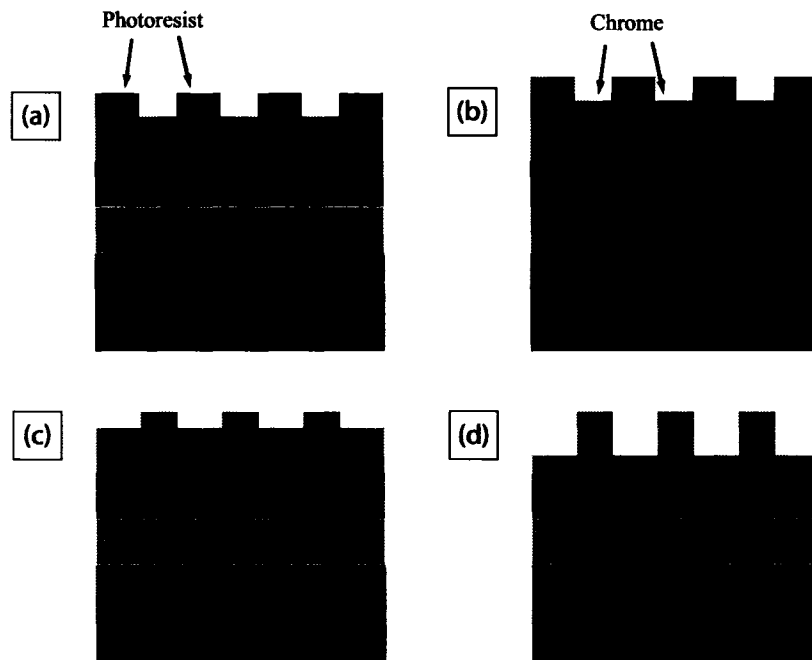


Figure 3.22: A  $SiO_2$  ribload process was attempted using a chrome masking layer patterned using the liftoff technique. (a) A silicon substrate with  $SiO_2$  undercladding,  $Er:SiO$  core layer, and  $SiO_2$  loading layer; a layer of photoresist has been patterned on top of the structure. (b) Chrome was deposited on the structure, covering the photoresist and filling the trenches between the photoresist pattern. (c) The photoresist is stripped. (d) An RIE process is applied to the structure transferring the chrome pattern into the  $SiO_2$  loading layer.

Parameter	Setting
$CHF_3$ gas flow	40 <i>sccm</i>
$O_2$ gas flow	5 <i>sccm</i>
Chamber pressure	40 <i>mT</i>
RF power	125 <i>W</i>
Etch time	360 <i>s</i>

Table 3.5: Etching parameters of the Trion *Phantom* RIE used for fabricating  $SiO_2$  ribload with a chrome mask.

acetone for several minutes. The sample could not be placed in a piranha bath (which would have been more effective at removing photoresist) because the piranha would etch chrome. The samples were next placed into a *Trion Phantom* RIE, and were patterned with a mixture of  $CHF_3$  and  $O_2$ . The RIE parameters are listed in Table 3.5. Samples were removed and cleaved for profile viewing by SEM.

### Fabrication Results

Under SEM investigation it was immediately obvious that the sidewall roughness of the waveguides is very high. A typical waveguide is shown in Fig. 3.23(a). The process was inconsistent; it produced good results (i.e. lower roughness) on some attempts. Fig. 3.23(b) shows a profile view of the chrome mask features after liftoff. The bent corners of the chrome mask suggest that there may have been a continuous layer of chrome from the layer in the trench to the layer on top of the photoresist. For this connected layer to occur, the patterned photoresist profile was likely positively tapered. The poor liftoff of the layer leaves a rough masking layer, which has been transferred into the  $SiO_2$  layer below. Due to the sidewall roughness, and the uncontrollable nature of this lift-off process, this process was deemed a failure.

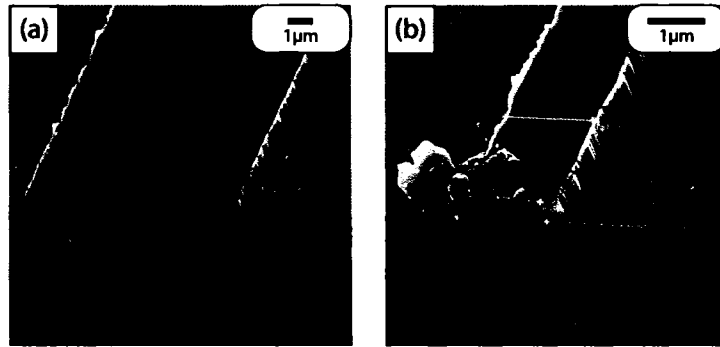


Figure 3.23: (a) Oblique angle view showing high rms roughness on the sidewall of the etched  $SiO_2$  layer. Good verticality is evident due to the high etching contrast between chrome and  $SiO_2$ . (b) Oblique angle view showing some of the bent chrome features at the edges of the waveguide. This likely occurred due to a chrome continuum between the top of the photoresist profile, and the trench bottom. The bent chrome features are considered responsible for the majority of the visible line-edge roughness.

### 3.4.6 Torlon Striploaded Waveguides

A successful fabrication method for low-loss polymer waveguides had been developed by our group based on a gold liftoff approach. The polymer used was a polyamide-imide (PAI), named *TorlonAI* – 10 from Solvay Advanced Polymers. Thus, Torlon was evaluated as a potential rib-loading or strip-loading material for SiO-based waveguides.

#### Fabrication

Silicon wafers with  $3\mu m$  thick PECVD  $SiO_2$  undercladding layers were cleaned, and had a layer of SiO deposited. The layers were again cleaned, and a layer of Torlon polymer of approx.  $500nm$  was spun-cast on top of the Er:SiO. Standard liftoff (see Section 3.4.5) was used to pattern a gold film layer (approx.  $100nm$  thick) on top of the PAI. The patterned samples were placed in an *Oxford Plasmalab 100* ICPRIE and were etched for several minutes using the *TRLabs Polymer* etching recipe. The parameters of the process are reviewed in table 3.6. The samples were removed from the ICPRIE and were cleaved for inspection.

Parameter	Setting
Temperature	0°C
SF <sub>6</sub> gas flow	2 sccm
O <sub>2</sub> gas flow	8 sccm
Chamber pressure	< 10 mT
ICP power	500 W
RF power	30 W
Etch time	360 s

Table 3.6: The known etching parameters of the *OXFORD Plasmalab 100* ICPRIE used for etching into Torlon polymer.

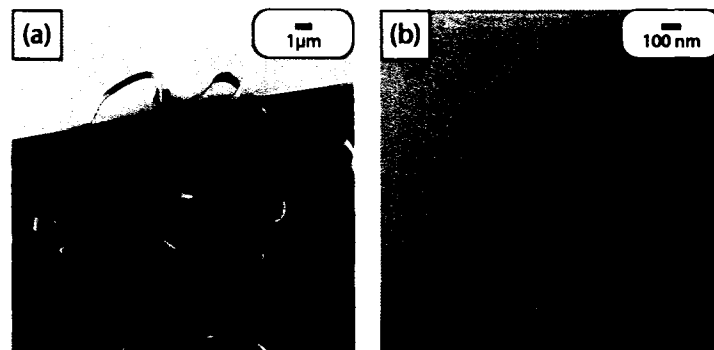


Figure 3.24: (a) Oblique angle view showing a delaminated Torlon ribbon. (b) Roughness in the SiO layer associated with ICPRIE ion bombardment of the SiO layer beneath the Torlon layer.

### Fabrication Results

It was immediately apparent that the Torlon layer did not adhere well to the sample. Fig. 3.24(a) shows a ribbon of Torlon delaminated upon cleaving. Fig. 3.24(b) shows roughness in the SiO layer from ionic bombardment. Due to the delamination, this process was deemed a failure.

## 3.5 Suggestions for Further Development

Fabrication research conducted in this project yielded many successes. It has also provided a large amount of information about planning and process exe-



cution. Some suggestions for both the choice of and organizational approach to future fabrication processes are described below.

### **3.5.1 Suggestions on Organizational Approach**

The most important aspect to remember about processing work is that it is experimental. Every person who pursues work in this area will learn by making mistakes, and overcoming them. Perhaps the important rule of process development is the following:

- Inspect everything that you are provided with to the best of your ability. This includes products and samples that may have been purchased or provided, or information and processing parameters that might or might not be applicable to your specific processing.

Microfabrication is a step-by-step process, and as discussed in Sec. 3.1, problems in a fabricated device could have persisted from any of the steps in the process. It is thus important to understand the goals of each step of the process, and to execute and verify that these goals are attainable in a repeatable fashion. Only after this should work continue on to the next step. Similar to this, processing tips or help should be put into context of your own work. The term *standard process* could mean that the step is ubiquitous to a large percentage of all processes, or it could be the specifically tailored process pertinent only to one person's work. It is important to know what is meant by such terminology and to validate the usefulness of such *standard processes* to your own work.

### **3.5.2 Suggestions for Fabrication Specific to This Project**

An important task that I would undertake if I were to have more time on this work would be to characterize and document the photoresist process. During the course of this project, low line-edge roughness photoresist profiles have been achieved in many cases. However, I know very little about

how to tailor the profile for specific applications, and little about reducing the striation on the sidewalls of the photoresist profile (see Fig. 3.15(a) and (b)). For processes where etching rates of the masking and masked material are similar, this mask profile (the line-edge roughness *and* the sidewall profile) will be transferred into the masked material (see for example, Fig. 3.15(b) and Fig. 3.20). It is no coincidence that the majority of successful processes in this project were based on processes with high etch ratios between the mask and masked layer. As discussed in Sections 3.3 and 3.4, a reduction of loss could certainly be achieved through better control of the photolithography process. Further, a reduction of the number of steps in a process often leads to higher success rates. This was the motivation for using photo-patterned SU8 as a striploading material (see Sec 3.3.3). To further enhance the usefulness of this type of process, a spin-on *high index* photo-patterned layer with variable thickness would potentially allow for highly conformal patterns to be produced in a single step on a wide array of materials. High-index materials of this type are commercially available in the form of spin-on photo-patterned titanium dioxide layers [45]. Finally, in the silicon post prefabrication method, it is important to try to maintain a centralized mode to reduce scattering losses. In order to do this, the thickness gradient nascent to a deposition system without rotation should be aligned along the length of the waveguides, so that at each point along the waveguide, there is no thickness gradient across the waveguide width which would push the mode to one side of the channel waveguides (see Sec. 3.3.1).

# Chapter 4

## Experimental Results

### 4.1 Introduction

The index of refraction is an essential material parameter used in the design of optical waveguides. This parameter was extracted for our silicon monoxide material based on the procedure described in Section 2.2. Results are reported in section 4.2. Using the index of refraction and target waveguide dimensions, undercladdings were designed using the techniques described in Section 2.3. These results will be discussed below in Section 4.3. Subsequently, waveguides were fabricated using the processes discussed in Section 3.3. in Section 4.4 methods for characterizing waveguides are discussed and results of applying these methods are reported. Finally, experiments were performed to quantify the suitability of erbium-doped silicon monoxide to provide signal amplification in the  $1.5 \mu m$  band. These results along with some discussion are provided in Sections 4.5 and 4.6.

### 4.2 The Index of Refraction

The index of refraction of silicon monoxide was extracted using the method discussed in Section 2.2. Briefly, a thin film of silicon monoxide was de-

posited by thermal evaporation onto a cleaned glass substrate to a thickness of approx.  $3\ \mu\text{m}$ . The sample was then annealed for 1 hour in an atmosphere of hydrogen and nitrogen at a ratio of 5 : 95. A spectrophotometric scan of the sample was collected at normal incidence using a Perkin-Elmer Lambda 900 spectrophotometer. The spectrophotometer uses a peltier cooled lead sulphide detector in the near-infrared region, and a photomultiplier tube in the UV-Vis region. Data in the region 400 to 3000  $\text{nm}$  was collected at increments of 2  $\text{nm}$ . Prior to the scan, the spectrophotometer was normalized by employing the internal calibration procedure. Further, prior to film deposition, a scan of the bare substrate was collected. Figure 4.1(a) shows the collected transmission scans for the bare substrate and the coated substrate overlaid. The peaks and troughs of the thin film transmission spectrum correspond to total constructive and total destructive interference conditions, respectively. The dips at approx. 1400  $\text{nm}$  and 2100  $\text{nm}$  in the substrate scan are related to the hydroxyl group density in the substrate. Corresponding dips do not appear in the thin film transmission scan; this might be because the annealing procedure has eliminated most of the hydroxyl groups. The discontinuity in the substrate scan at approx. 800  $\text{nm}$  is an artifact of the spectrophotometer. Using Swanepoel's method, the index of refraction can be extracted from the collected data. A plot of the index of refraction values and a Wemple-DiDomenico spectral fit of the data are shown in Fig. 4.1(b) [46]. A refractive index of approximately 1.9 is extracted in the 1.5  $\mu\text{m}$  region. Different samples which were tested prior to annealing did not show a significant difference in refractive index in the 1.5  $\mu\text{m}$  region. The addition of small amounts of erbium does not appreciably change the index of refraction in the 1.5  $\mu\text{m}$  region either. The results were confirmed using a prism-coupling technique in the 1.5  $\mu\text{m}$  band, and the value is supported by previous work by Roberts and Parker [26], and Haas and Salzburg [47] who found values of 1.85 and 1.9, respectively.

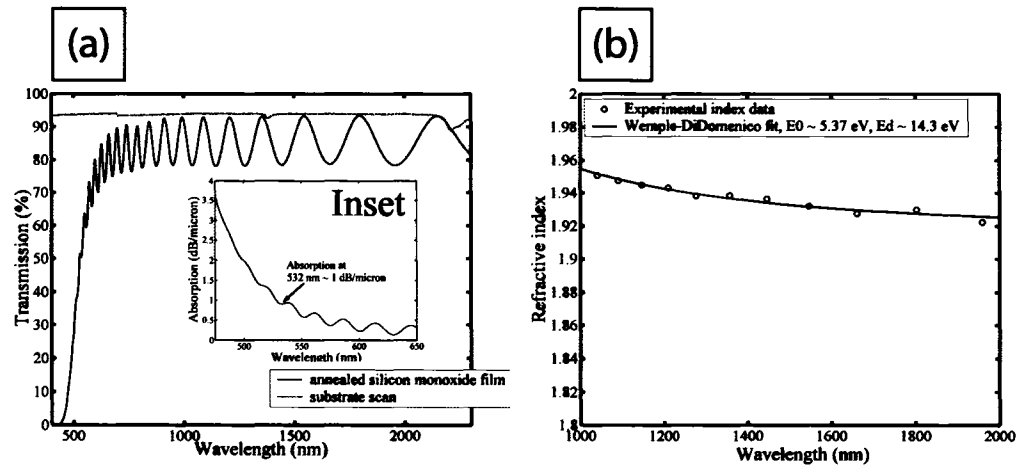


Figure 4.1: (a) Transmission spectra of substrate alone and of annealed silicon monoxide thin film on substrate collected using a spectrophotometer. Inset: The level of absorption in the 475 nm to 650 nm spectral region. The absorption at 532 nm is approx. 1 dB/ $\mu\text{m}$ . (b) A spectrally dependent index of refraction profile extracted using the transmission spectra from (a) and by employing the method described in Section 2.2.

### 4.3 Undercladding Design and Results

Since the ultimate goal of this work is the integration of optical amplification devices on silicon, all of the waveguides have been produced on silicon substrates. Silicon has a high index of refraction in the 1.5  $\mu\text{m}$  region, of approx. 3.5. As determined in Section 4.2, the index of the silicon monoxide thin films being produced is approx. 1.9. As such, a buffer layer must be grown between the desired silicon monoxide guiding layer and the silicon substrate to prevent light from escaping into the substrate. The theory of Section 2.3 has been employed to determine a suitable undercladding thickness.

Undercladding materials tested included PECVD grown  $\text{SiO}_2$ , thermally grown  $\text{SiO}_2$ , and polymers. It was determined that none of the available polymers could withstand the annealing cycle at 500°C. The PECVD  $\text{SiO}_2$  was ruled out based of poor surface characteristics and high cost. The majority of successful waveguides fabricated employed thermal  $\text{SiO}_2$  as an undercladding. Thermal  $\text{SiO}_2$  was grown directly on cleaned silicon substrates

Layer	Material	Index of Refraction	Thickness
1	BCB	1.54	infinite
2	annealed silicon monoxide	1.9	0.65 $\mu m$
3	thermal $SiO_2$	1.46	0.5 $\mu m$ - 3 $\mu m$
4	silicon	3.5	infinite
Simulation wavelength = 1550 $nm$			

Table 4.1: Undercladding thickness simulation parameters.

using wet thermal oxidation. The oxide produced has an index of refraction of 1.46. A simulation was conducted to predict substrate leakage loss using the parameters listed in Table 4.1, and the results are shown in Fig. 4.2. There will always be a residual level of loss incurred, so the goal is to select an undercladding thickness that reduces leakage loss to negligible levels with respect to the other forms of waveguide losses. Waveguides with overall propagation losses less than 1  $dB/cm$  are typically considered of good quality. If we thus select a substrate thickness that provides less than 0.01  $dB/cm$  leakage loss, this thickness should prove acceptable. The TM mode crosses the 0.01  $dB/cm$  threshold at approx. 1.8  $\mu m$  thickness. Any thickness greater than this should be acceptable. Experimentation with wet thermal oxidation revealed that a 16 hour exposure yields greater than 2  $\mu m$  of thermal  $SiO_2$ . This was the standard process used for undercladding growth in subsequent fabrication runs.

### 4.3.1 Estimation of Substrate Leakage Loss for 2D Confining Waveguides

For 2D confining waveguides, a more valid approach to predicting substrate leakage loss would be to use propagation constants that have been theoretically predicted for 2D waveguides. 2D waveguides will always have a lower propagation constant than corresponding slab waveguides since more of the mode will interact with low-index cladding regions. A lower propagation

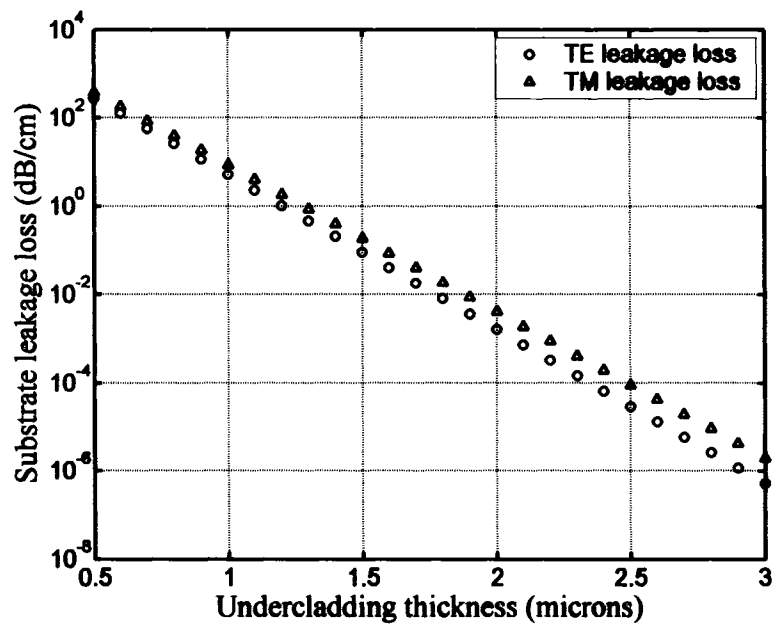


Figure 4.2: Substrate leakage loss for a slab waveguide whose parameters are listed in table 4.1.

Volume Designation	Material	Index of Refraction	Thickness
n1	BCB	1.54	infinite
n2	annealed silicon monoxide	1.9	height: 0.65 $\mu m$ width: 6.0 $\mu m$
n3	thermal $SiO_2$	1.46	1.0 $\mu m$ - 2.0 $\mu m$
n4	BCB	1.54	infinite
n5	BCB	1.54	infinite
substrate	silicon	3.5	infinite
Simulation wavelength = 1.55 $\mu m$			

Table 4.2: EIM substrate leakage loss simulation parameters. The parameters have been selected based on constructed devices.

constant leads to higher penetration of the mode outside of the core region, increasing the interaction of a mode with the substrate. This method was applied to all of the waveguides described in this thesis. The simulation parameters for the EIM are listed in Table 4.2. The simulation parameters are nearly identical to those from Section 2.3.4. However, the simulation wavelength in this case is 1.55  $\mu m$ .

Figure 4.3 shows the substrate leakage loss for each of the modes found for the strip waveguide structure shown in Fig. 3.14 in the substrate thickness range 1 -2  $\mu m$ . It is believed that the as-fabricated undercladding thickness is approx. 1.3  $\mu m$ . Given this thickness, the substrate leakage loss should be approx. 0.2  $dB/cm$  for the fundamental TE mode and a few times this for the fundamental TM mode. It is apparent that leakage loss increases with the mode order. Sufficiently high-ordered modes, though valid modal solutions, will be filtered due to the high substrate leakage loss.

Construction of subsequent devices should aim for undercladding thicknesses of greater than 2  $\mu m$  to reduce substrate leakage losses to negligible levels as compared with other forms of loss.



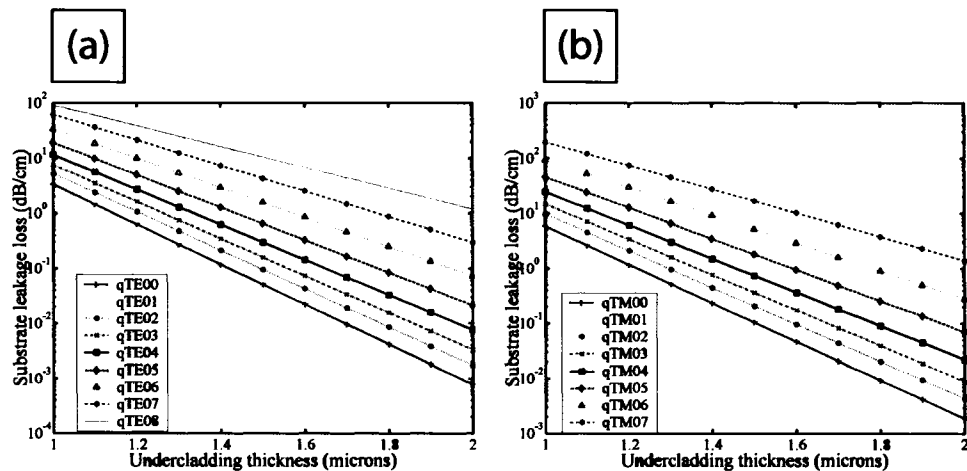


Figure 4.3: Substrate leakage loss for a strip waveguide whose parameters are listed in Table 4.2.

## 4.4 Waveguide Loss Characterization

Of significant importance in the validation of any waveguide under test is optical loss characterization. A waveguide can lose optical power due to either *material* losses, or *fabrication* related losses. *Material* losses include *absorption* losses and *scattering* losses. *Absorption* losses could be due to electronic transitions or a variety of phonon-related events. *Material scattering* losses are due to material inhomogeneities. *Fabrication* losses are comprised of *interfacial scattering* losses, *mode-field mismatch* losses, and the *substrate leakage* losses discussed in Sections 2.3.2 and 4.3. *Fabrication scattering* losses are due to interface roughness typically induced by microfabrication-related processing. *Mode-field mismatch* losses occur at the junction of two dissimilar waveguides, for example an optical fibre connected to a rectangular waveguide. *Mode-field mismatch* losses can be predicted by conducting an overlap integral of the modal solutions, and are often referred to as *coupling* losses. It is often difficult to discern whether losses are due to *material* or *fabrication* issues, unless materials can be prepared in bulk form or waveguides can be fabricated with extremely low *fabrication scattering* losses. However, if the

composite loss value is low enough, it may not be necessary to determine the exact nature of the losses. The term *propagation* loss is also often employed to refer to the sum of all losses mentioned above (except *mode-field mismatch* losses), and is the optical loss figure of merit with most practical significance for a given waveguide.

#### 4.4.1 Waveguide Loss Characterization Techniques

There are a few key methods in popular use to characterize the optical loss of a waveguide. The three that were attempted in this thesis were the insertion loss technique, the Fabry-Perot resonance method, and scattering-collection method.

##### The Insertion Loss Technique

The insertion loss technique is an intuitively straightforward technique used for characterizing waveguide loss. An optical fiber carrying a known amount of power is butt-coupled to a waveguide, and the power exiting the waveguide is collected with an objective and recorded using a photodetector. A mathematical model employing the frequency-response of each element,  $H_{element}$ , can be used to express the relationship between the waveguide response,  $H_{WG}$ , the launched power,  $S_{LASER}$ , and the collected power,  $P_{PD}$ . A reference scan can be used to remove the responses of the other elements in the lightpath. This type of setup is shown in Fig. 4.4.

To ascertain the spectral insertion loss of the waveguide, a scan is obtained using the setup shown in Fig. 4.4, followed by a reference scan with the waveguide in Fig. 4.4 removed. The output of the system will be a function of the responses of each element in the setup, and  $P_{PD}$  can be expressed as:

$$P_{PD} = S_{LASER}H_{PC}H_{WG}H_{OBJ}H_{PD} \quad (4.1)$$

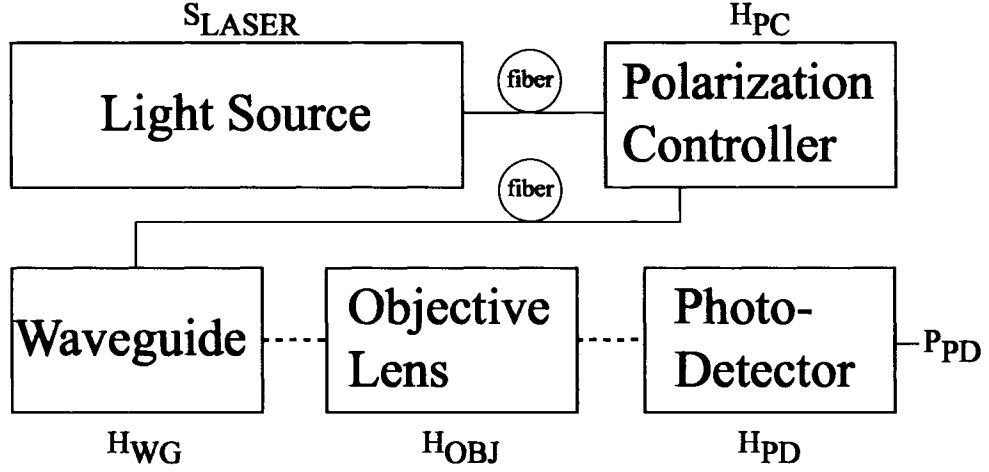


Figure 4.4: System setup used to characterize waveguides for insertion loss.

The reference scan response will have the form of eqn. 4.2.

$$P_{PDREF} = S_{LASER}H_{PC}H_{OBJ}H_{PD} \quad (4.2)$$

And by dividing eqn. 4.1 by eqn. 4.2 an expression for the waveguide response is obtained as in eqn. 4.3.

$$\frac{P_{PD}}{P_{PDREF}} = \frac{S_{LASER}H_{PC}H_{WG}H_{OBJ}H_{PD}}{S_{LASER}H_{PC}H_{OBJ}H_{PD}} = H_{WG} \quad (4.3)$$

Neglecting reflections at the waveguide facets,  $H_{WG}$  includes contributions due to *mode-field mismatch* losses and *propagation* losses. It is important to separate the two, as it is mainly the *propagation* loss being sought. To separate the two, the modal profile of the waveguide under test must be determined, along with the mode-field of the optical fiber in use. The modal profile of the optical fiber is circular, and the dimensions of the mode-field are given in accompanying data sheets. A trio of methods can be used to obtain an estimate of the *mode-field mismatch* losses of the waveguide under test. The first method involves microscopic inspection and estimation of waveguide dimen-

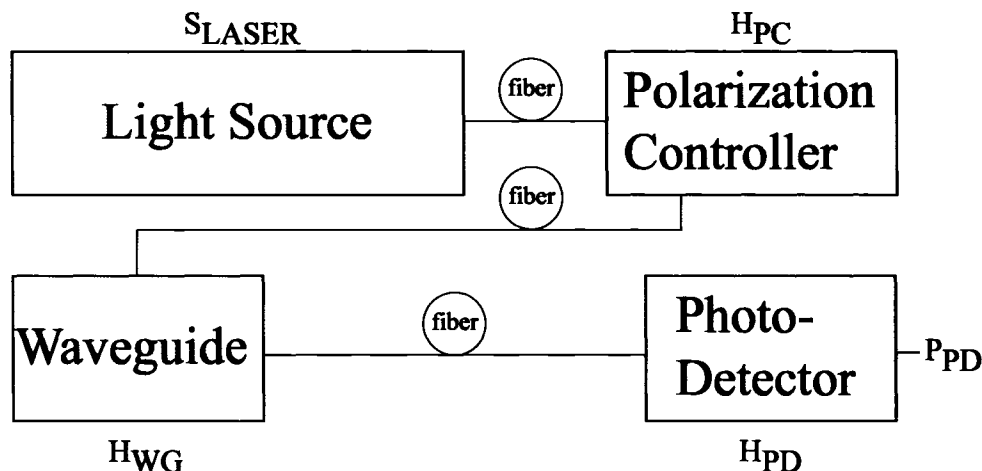


Figure 4.5: System setup used to empirically characterize *mode-field mismatch* losses in conjunction with the setup in Fig. 4.4.

sions followed by the use of a simulation package to determine a theoretical waveguide mode-field. The mismatch losses are then estimated by performing an overlap integral of the theoretical fiber and waveguide mode-fields. This method was carried out for a post waveguide from the *SPPM* process using SEM to estimate the spatial dimensions, and OptiBPM to determine the fundamental mode of the waveguide. OptiBPM is a computer-aided design tool with a built-in mode solver. The second method is empirical and seeks to determine the difference in collected power between the setup shown in Fig. 4.4, and that in Fig. 4.5. The only difference between the two setups is that a second fiber is butt-coupled to the back-end of the waveguide and then guided to a photodetector. The difference in collected power between the two setups can then be attributed to the *mode-field mismatch* loss at the second waveguide-fiber interface, and due to the removal of the objective. If losses due to the objective are assumed negligible, then the difference in collected power can be attributed mainly as *mode-field mismatch* loss.

The third method involves the experimental determination of the mode-field by spatially probing the optical field periodically. This can be accom-

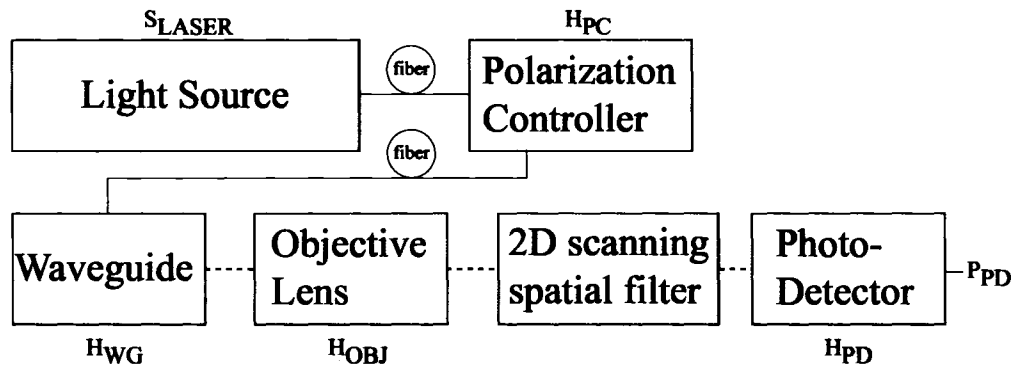


Figure 4.6: System setup used to measure the mode-field profile of a waveguide by scanning across the face of the mode and periodically sampling the projected mode power.

plished by the use of a CCD array of photodetectors, or by use of a single photodetector scanned through the optical field. Due to the relative sizes of the optical mode-field and the photodetection equipment, the mode-field is typically expanded using a set of lenses or an objective lens. A schematic of the setup used to probe the optical mode-field is shown in Fig. 4.6. This setup is sometimes augmented using an optical chopper and lock-in detection. This method was attempted using an objective which magnified the mode-field by a factor of approx. 100. The magnification was estimated by applying this technique to single-mode fibers with known mode-fields. A small (approx.  $10 \mu\text{m}$  diameter) pinhole was used as a spatial filter. The pinhole was placed as close to the photodetector as possible. The spatial filter was raster scanned perpendicular to the direction of propagation of the mode, and at each point a measurement of the power was taken. The two-dimensional image was then reconstructed, to display the measured modal profile. It is important to note that the objective lens used to project the modal image has a finite resolution, and that images may become smeared if the mode-field dimensions approach or exceed the resolution limit of the objective lens.

Fig. 4.7(a) shows the fundamental TE mode profile produced by OptiBPM based on the dimensions estimated using SEM. The waveguide core was sim-

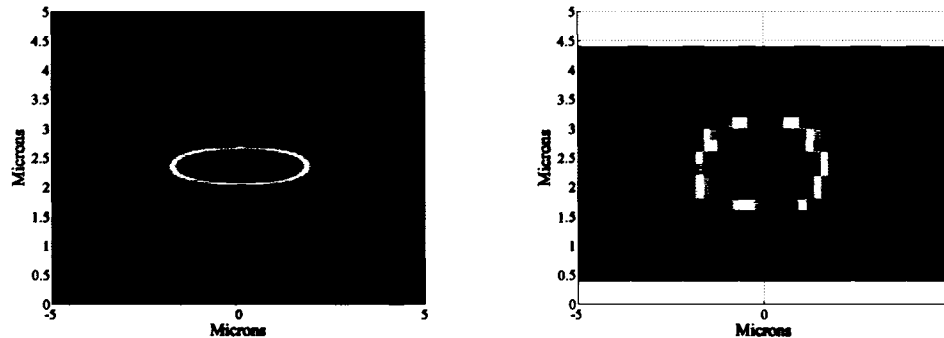


Figure 4.7: (a) Modal profile of a post waveguide simulated using OptiBPM. (b) Modal profile of a similar post waveguide collected by expanding the waveguide mode, and sampling the power in different regions of the mode. The limited resolution of the objective lens used in this setup is believed to cause the vertical expansion of the mode with respect to (a).

ulated as a rectangular box with a height of approx.  $0.65 \mu m$ , and a width of approx.  $6 \mu m$ . The simulation was conducted for a wavelength of  $1300 nm$ . Fig. 4.7(b) shows the experimental mode-field profile collected using an objective lens and a scanning pinhole. The profiles are quite similar in the horizontal direction. However, the experimentally collected vertical mode-field is much larger than its simulated counterpart. This is attributed to the limited resolution of the objective lens which has already been estimated as approx.  $1 \mu m$  [48].

Coupling losses were estimated by conducting an overlap integration between the theoretically predicted mode profiles of the waveguide and optical fiber. The fiber in use was from Nufern and has a mode-field diameter of approx.  $4.8 \mu m$ . A coupling loss of approx.  $4.4 dB$  was estimated. The coupling losses estimated from the empirical technique of replacing the objective with a second fiber-coupling point were approx.  $4.8 dB$ . The close agreement of these estimates is encouraging.

## The Fabry-Perot Technique

The Fabry-Perot technique for estimating waveguide propagation losses involves treating the waveguide as a resonant cavity, with cleaved waveguide facets playing the role of mirrors [49, 50]. One advantage of this technique is that propagation losses can be determined independent of any knowledge regarding the coupling losses.

Due to the change in index of refraction at the input and output of the waveguide, light will reflect at each of these facets. Light that reflects first at the back facet, and then a second time at the front facet will be co-propagating with the originally coupled beam of light. The co-propagating beams may be out of phase with each other. The phase difference will be a function of the length of the cavity, the index of refraction, and of the frequency of the light. By changing any of these conditions, the relative difference in phase between the beams can be changed. If the input source is scanned in frequency and has sufficiently narrow spectral width, the phase difference will move through an entire  $2\pi$  radians. The output from the waveguide will show maxima and minima corresponding to complete constructive and complete destructive interference. Bear in mind, that there will be an infinite number of reflections at the front and back facets which will interfere together at the output facet of the waveguide. A diagram of the situation is shown in Fig. 4.8.

In the absence of waveguide propagation losses, the depth of the interference modulation will depend on the difference in effective index of refraction between the waveguide mode and the external medium (i.e. the facet reflectivity). If there is an amount of propagation loss through the waveguide, the reflected beam will be weakened and the depth of modulation will be reduced. This is qualitatively shown in Fig. 4.9. The depth of modulation can be used to estimate the propagation losses of the waveguide. Losses can

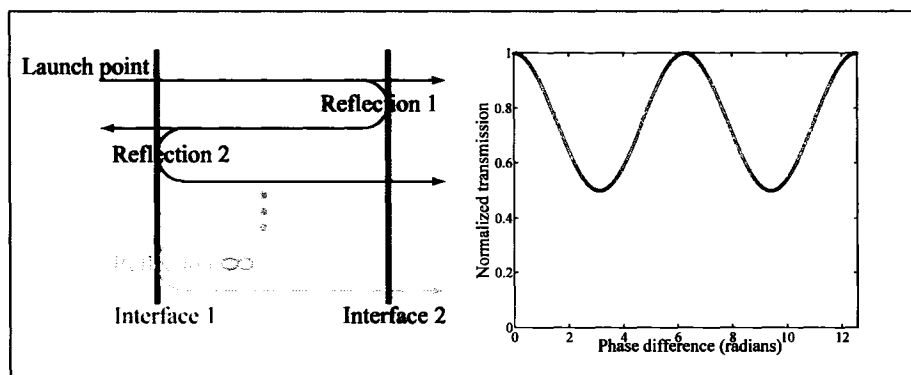


Figure 4.8: A schematic showing how a transmitted signal and a reflected signal can interfere at the output of a waveguide. The graph on the right displays the output signal strength as a function of the phase difference between the two beams. In general this description is a simplification as there are an infinite number of reflections within the waveguide, and an infinite number of beams interfering at the output of the waveguide.

be estimated by using eqn. 4.4 [48].

$$loss = -\frac{1}{L} 10 \log \left[ \frac{1}{R} \frac{K^{\frac{1}{2}} - 1}{K^{\frac{1}{2}} + 1} \right] \quad (4.4)$$

In eqn. 4.4,  $K$  is the ratio of the maximum to the minimum output power,  $R$  is the geometric mean of the power reflection coefficients at the waveguide facets, and  $L$  is the length of the waveguide in centimeters [48]. One difficulty with regard to this method is the requirement of good quality facets. Poor quality facets will lead to poorer reflection, and losses due to scattering. Cleaving good quality facets was a consistent problem in the *SPPM* process, documented in section 3.3.1. A second problem of the Fabry-Perot is its insensitivity to multi-moded waveguides. Each mode travels with a different effective index, and so will have a different resonant period. The waveguides from the *SPPM* have been documented to be multi-moded. Attempts to characterize waveguides produced using the *SPPM* process with this method did not provide good results.



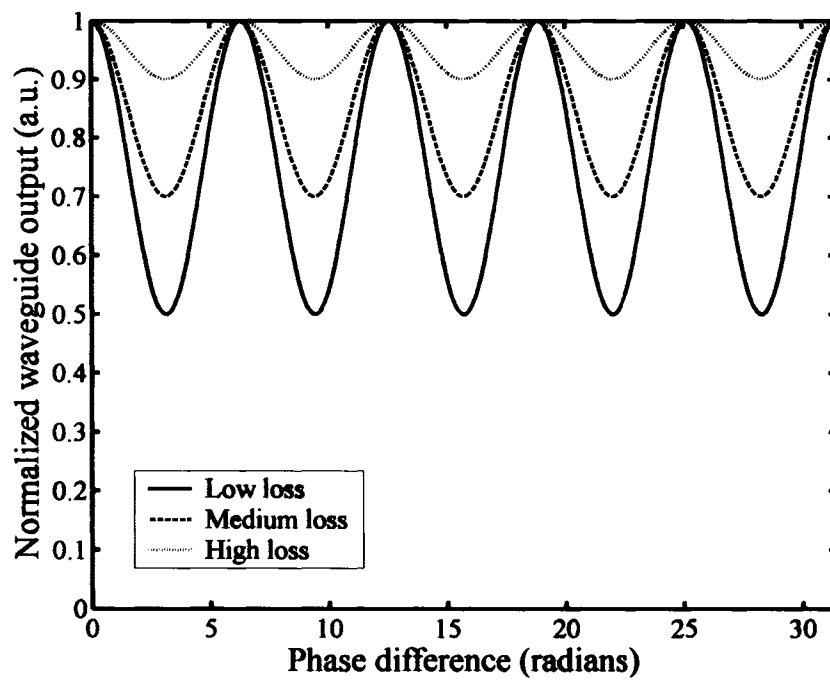


Figure 4.9: Example of Fabry-Perot fringing in a singlemode waveguide with three different values of loss. As the loss increases, the modulation depth decreases.

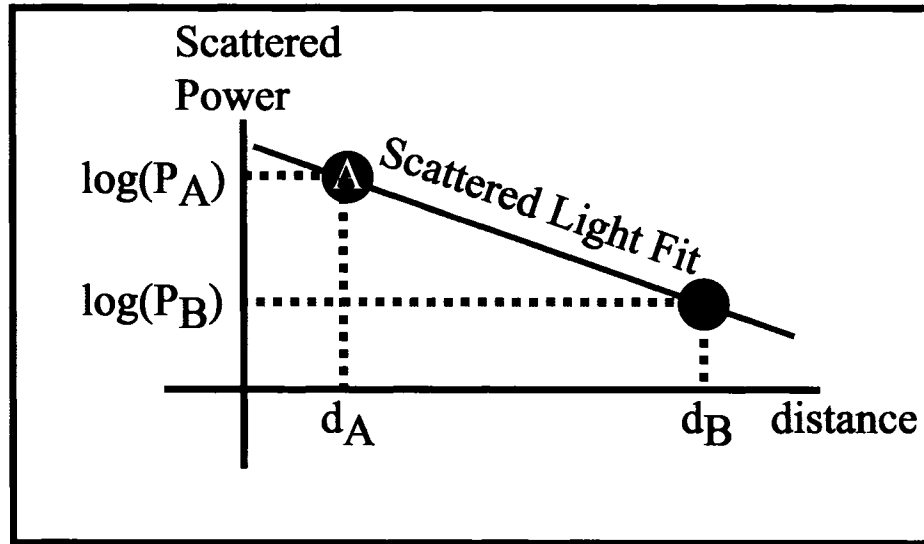


Figure 4.10: A method of estimating the propagation loss of a waveguide by collecting light scattered from a waveguide.

### The Scattering-Collection Method

The scattering-collection method is based on the principle that the amount of light scattered from a waveguide is proportional to the amount of light in the waveguide [51]. If two points along a waveguide are selected, the scattered light measurement at each point allows relative levels of power to be determined as a function of distance. This situation is shown in Fig. 4.10. An estimate of the propagation loss can be determined through the use of Beer's Law, shown in eqn. 4.5. The use of more points provides higher levels of confidence in the loss assessment.

$$\alpha = \frac{\log_{10}(P_A) - \log_{10}(P_B)}{d_B - d_A} \quad \left[ \frac{dB}{cm} \right] \quad (4.5)$$

For this method to be valid, the waveguide under test should not have

any major defect points that correspond to large scattering centers. Large scattering centers will provide discontinuities in the *scattered light fit* line illustrated in Fig. 4.10, and will typically lead to an overestimation of the propagation loss.

This method was applied to waveguides produced using the *SPPM* process, however, poor results were obtained.

## 4.4.2 Measured Waveguide Losses

### Waveguides from the *SPPM* Process

Two of the fabrication runs using the *SPPM* process produced relatively low-loss waveguides. The experiments were conducted on chips from batches labeled *ICPRIE wafer #2*, and *ICPRIE wafer #7*. As discussed in Section 4.4.1, only the *insertion loss* technique provided reliable results, and these waveguides were thus characterized using this method. There was only one useful sample from the batch labeled as *ICPRIE wafer #2*, and there were two useful chips from the batch labeled *ICPRIE wafer #7*. Significant results from each of the samples are listed in Tables 4.3, 4.4, and 4.5. along with descriptions of the samples.

Scatter in the results reflects both the experimental nature of the fabrication processes, and the short waveguide lengths used for testing. Because of these issues an error estimate of approx.  $1 \text{ dB/cm}$  [49] should be applied to the results. However, the collected information lends support to the conclusion that low loss waveguiding in SiO based materials is possible.

### Waveguides from Processes other than the *SPPM*

Waveguides were fabricated using other processes including those described in Sections 3.3.2 and 3.3.3. However, most processing attempts were conducted with rough PECVD oxide undercladdings (see Section 3.4.1). Due to time constraints these processes could not be thoroughly re-attempted after this

ICPRIE wafer #2 chip #1, length = 8.3 mm			
SiO guiding layer (1 $\mu m$ ) on SiO <sub>2</sub> undercladding (1.3 $\mu m$ ) on Si substrate			
Waveguide width ( $\mu m$ )	Measured insertion loss (dB)	Estimated <sup>+</sup> coupling loss (dB)	Estimated propagation loss (dB/cm)
6	7.4	3.9	4.2
6	14.2	3.9	12.4
6	14.4	3.9	12.7
6	16.5	3.9	15.2
5	9.6	3.3	7.6
5	16.9	3.3	16.4
5	16.1	3.3	15.4
4	12.2	3.5	10.5
4	16.5	3.5	15.7
4	10.2	3.5	8.1
3	14.2	4.1	12.2
3	13.6	4.1	11.4
measurement wavelength = 1530 nm, polarization = TE			
<sup>+</sup> estimated based on theoretical mode-field overlap			

Table 4.3: Important loss results from ICPRIE wafer #2 chip #1.

ICPRIE wafer #7 chip #2, length = 8 mm			
BCB upper cladding (10 $\mu m$ ) on SiO:Er guiding layer (0.65 $\mu m$ ) on SiO <sub>2</sub> undercladding (1.3 $\mu m$ ) on Si substrate			
Waveguide width ( $\mu m$ )	Measured insertion loss (dB)	Estimated <sup>+</sup> coupling loss (dB)	Estimated propagation loss (dB)
6	5.9	4.4	1.9
6	7.3	4.4	3.6
6	10.1	4.4	7.1
6	10.2	4.4	7.3
6	9.3	4.4	6.1
5	11.7	4.2	9.4
5	13.0	4.2	11.0
5	14.1	4.2	12.4
5	13.5	4.2	11.6
5	14.3	4.2	12.6
measurement wavelength = 1300 nm, polarization = TE			
<sup>+</sup> estimated based on theoretical mode-field overlap			

Table 4.4: Important loss results from ICPRIE wafer #7 chip #2.

ICPRIE wafer #7 chip #3, length = 4 mm			
BCB upper cladding (10 $\mu m$ ) on SiO:Er guiding layer (0.65 $\mu m$ ) on SiO <sub>2</sub> undercladding (1.3 $\mu m$ ) on Si substrate			
Waveguide width ( $\mu m$ )	Measured insertion loss (dB)	Estimated <sup>+</sup> coupling loss (dB)	Estimated propagation loss (dB)
6	5.1	4.4	1.8
6	4.6	4.4	0.5
6	4.9	4.4	1.3
6	5.1	4.4	1.8
measurement wavelength = 1300 nm, polarization = TE			
<sup>+</sup> estimated based on theoretical mode-field overlap			

Table 4.5: Important loss results from ICPRIE wafer #7 chip #3.

problem had been identified. Preliminary results suggest that these processes could provide low loss waveguiding using refined undercladding processes. Processes such as the ribload process, and SU8 photopatterning process have the added advantage of being far simpler than the *SPPM* process, reducing the number of potential problems, and likely reducing fabrication-testing cycle times.

### **TE and TM Polarization**

Both polarization states were attempted for insertion loss characterization of the *SPPM*. It was found that TE polarization provided consistently lower insertion losses. This can be attributed to a few factors. TM light will penetrate more into the silicon substrate as discussed in section 4.3. By visual comparison of the leakage loss plots, the fundamental TM modal loss is typically 2–3 times the loss experienced by its TE equivalent. This difference could be as much as a few decibels per centimeter given the undercladding thickness in the fabricated waveguides. Second, simulations have shown that the fundamental TE mode for the 6  $\mu\text{m}$  waveguide is nearly identical in horizontal width to that of the Nufern fiber. The TM mode will likely be slightly less well matched, and will incur excess mode-field mismatch loss. New undercladding processes should mitigate some of this excess loss.

## **4.5 Spectroscopic Characteristics**

The goal of this work was to characterize the viability of Er:SiO as an optical amplification medium. In pursuit of this goal, experiments were conducted to estimate the optical absorption and emission cross-section for the  ${}^4I_{15/2}$  to  ${}^4I_{13/2}$  transition of the erbium ion. An experiment into the linearity of waveguide devices has also been conducted to explore potential nonlinear effects. Finally, waveguides from the *SPPM* process have been optically pumped in an attempt to invert erbium ions, and to measure potential signal

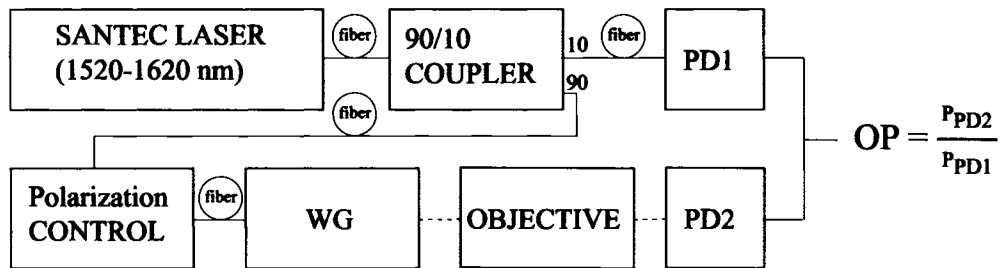


Figure 4.11: Schematic of the system used to obtain broadband transmission scans of the erbium doped waveguides under test. Dashed red connections indicate free-space, and solid blue connections indicate an electrical connection.

enhancement.

#### 4.5.1 Absorption Cross-section

Absorption spectroscopy was conducted on waveguides fabricated from the SU8 process (Section 3.3.3), and the *SPPM* process (Section 3.3.1). In each case a setup similar to that shown in Fig. 4.11 is used to collect the broadband absorption data. This process is similar to the insertion loss technique described in section (4.4.1). A tunable laser is scanned in the 1520 *nm* to 1620 *nm* band. At each point the ratio of  $P_{PD2}$  to  $P_{PD1}$  is taken. The ratio is used to calibrate for variations in the laser power. A reference scan is taken with the waveguide removed as described in Section (4.4.1). The reference scan is used to correct for the system response. Prior to data collection, the waveguide coupling is optimized, and polarization is tuned for maximum transmission (TE).

The transmission experiment effectively provides the insertion loss at each point in the spectral band. Given the nature of the erbium absorption, a maximum insertion loss is expected at a wavelength of approx. 1534 *nm*. The erbium-related absorption falls to nearly zero at a wavelength of 1620 *nm*. The difference in insertion loss between these two wavelengths can then be used as a good estimate of the peak erbium-related absorption. Similar broadband transmission experiments were conducted on undoped wave-

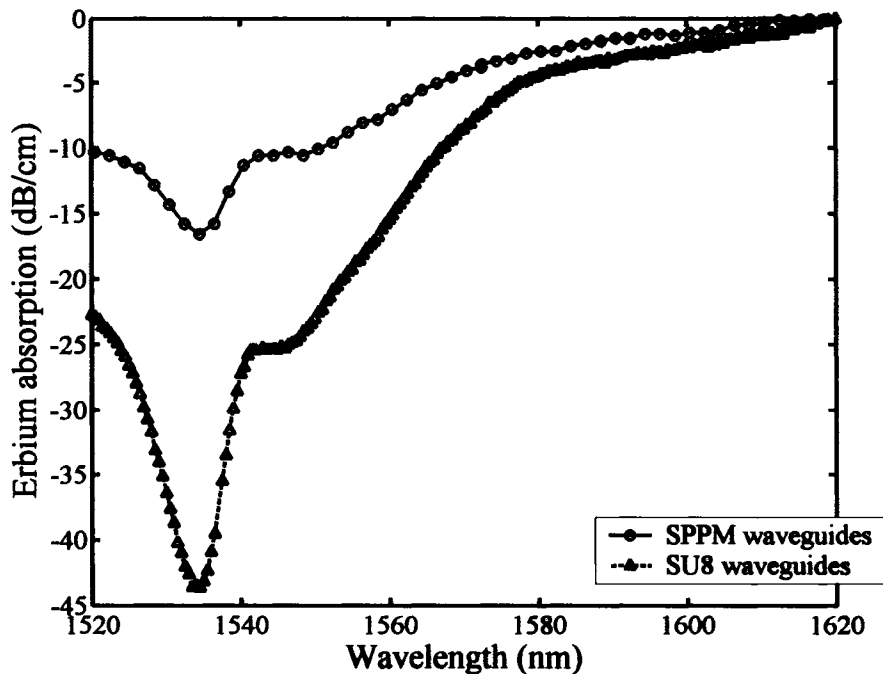


Figure 4.12: A transmission experiment conducted on Er:SiO waveguides fabricated using the SU8 and *SPPM* processes, respectively. The results have been scaled to a length of 1 cm for more accurate comparison. EMPA conducted on the SU8 guides revealed an erbium concentration of approx. 1.7 at.%. The concentration of the *SPPM* waveguides is believed to be approx. 1 at.%.

guides. The difference in insertion losses between 1520 nm and 1620 nm was assessed to be negligible compared the erbium-related absorption. Fig. 4.12 shows broadband scans of erbium-related waveguide absorption from the SU8 and *SPPM* processes. The scans have been scaled to show absorption per centimeter.

Electron microprobe analysis (EMPA) was conducted on the samples used in the SU8 waveguide process [52]. An erbium concentration of approx. 1.7 at.% was estimated. An estimate of the peak  ${}^4I_{15/2}$  to  ${}^4I_{13/2}$  absorption cross section can be made by using the relation in eqn. 4.6.  $\Gamma$  is a measure of the mode overlap with the active waveguiding region. A lower bound estimate on the



absorption cross-section can then be made by assuming  $\Gamma = 1$ . The erbium concentration (1.7 at.%) corresponds to  $N_{erb} \simeq 1 \times 10^{21} / \text{cm}^3$ . The peak absorption of the SU8 waveguides is approx. 44 dB/cm which corresponds to approx. 10 /cm. Using these values the absorption cross-section is estimated to be approx.  $1 \times 10^{-20} \text{ cm}^2$  which is similar to other silicate glasses, and to some Er:SiNC:SiO<sub>2</sub> glasses [5, 6, 32, 53]. It is approximately 1 order of magnitude lower than the cross-section reported by Han et al. in [54].

$$\sigma_{peak} = \frac{\alpha_{peak}}{\Gamma N_{erb}} \quad (4.6)$$

EMPA results for samples from the *SPPM* process were pending at the time of writing.

## 4.5.2 Waveguide Photoluminescence

Waveguide photoluminescence experiments have been conducted by directly pumping erbium ions, and by indirectly exciting erbium via the nanoclusters. A schematic showing the separate cases of pumping resonantly and non-resonantly is given in figure ???. The erbium was directly pumped with 980 nm and 1480 nm light using the configuration shown in Fig. 4.14. In this configuration, pump power is launched into the waveguide and light in the 1.55 μm band is emitted. Light traveling backwards through the waveguide is coupled into the common port of the WDM, and exits through the 1550 nm port. This light is collected using an optical spectrum analyzer. For complete rigor, the luminescence data should be corrected for the response of the WDM, but this was not done since it was not expected that the WDM would have large wavelength dependence in the 1450 nm to 1650 nm band.

Figure 4.15 shows photoluminescence traces taken using the setup in Fig. 4.14 for varied pump power from a 980 nm laser. It is apparent that the PL has the familiar erbium emission shape. The pump power is increased by a factor of 10, though the PL only increases by a factor of approx. 2. This is

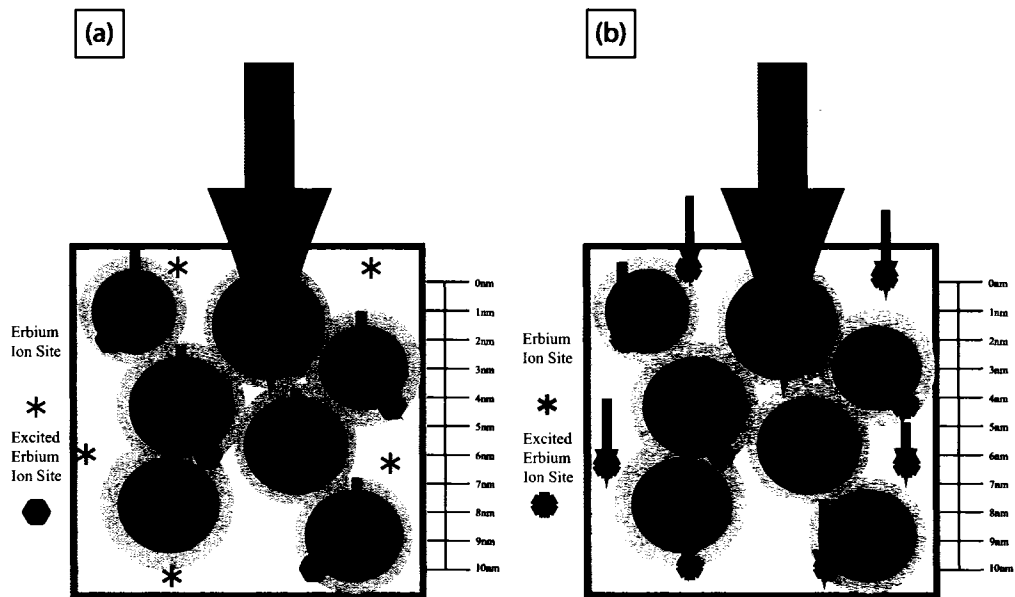


Figure 4.13: Different schemes for excitation of erbium in Er:SRO materials. (a) Pumping of erbium using amorphous silicon nanoclusters as sensitizers. Photons with energy above the material bandgap energy excite carriers within silicon nanoclusters. Carriers may eventually recombine and transfer the recombinant energy to a nearby erbium ion. It is possible that some erbium ions may be at too large a distance from silicon nanoclusters to be properly sensitized, and may not be excitable using this pumping technique. (b) Pumping of erbium directly using resonant erbium pump bands such as  $980\text{ nm}$  or  $1480\text{ nm}$ . This method of pumping should be capable of exciting all of the erbium ions within the material.

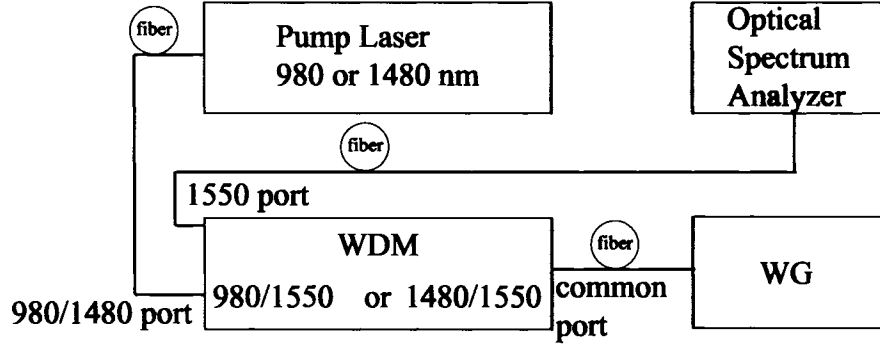


Figure 4.14: A setup used to collect waveguide photoluminescence generated by pumping at either 980 nm or 1480 nm. Power is launched from the pump laser through the WDM 980/1480 port out of the common port and into the waveguide. Backwards-travelling photoluminescence in the 1550 nm band is coupled back into the WDM through the common port and is directed out the 1550 nm port before being collected using an OSA.

potential evidence of saturation of the metastable erbium level.

Waveguides were also pumped using a 374 nm laser. This wavelength does not coincide with any direct erbium absorption bands. The laser was focused into a stripe using one spherical and one cylindrical lens, and shone onto the waveguide. Photoluminescence was collected using the setup shown in Fig. 4.16. Fig. 4.17 shows the photoluminescence spectrum generated by pumping with 374 nm light. This is evidence of non-resonant excitation of erbium via pump absorption by silicon nanoclusters.

The emission cross-section can be estimated by making use of the decay time of the metastable erbium level and the shape of the photoluminescence spectrum through the Fuchtbauer-Ladenberg [55] relation expressed in eqn. 4.7:

$$f_{ex-sec}(\lambda) = \frac{\lambda^4 f_{PL}^N(\lambda)}{8\pi cn^2 \tau_{rad} \int f_{PL}^N(\lambda) d\lambda} \quad (4.7)$$

where  $f_{ex-sec}$  is the predicted emission cross-section as a function of wavelength,  $f_{PL}^N$  is the normalized photoluminescence spectrum,  $n$  is the index of refraction of the medium,  $\tau_{rad}$  is the radiative lifetime of the metastable level, and  $\int f_{PL}^N(\lambda) d\lambda$  is an effective line width [55]. The absorption cross-section,

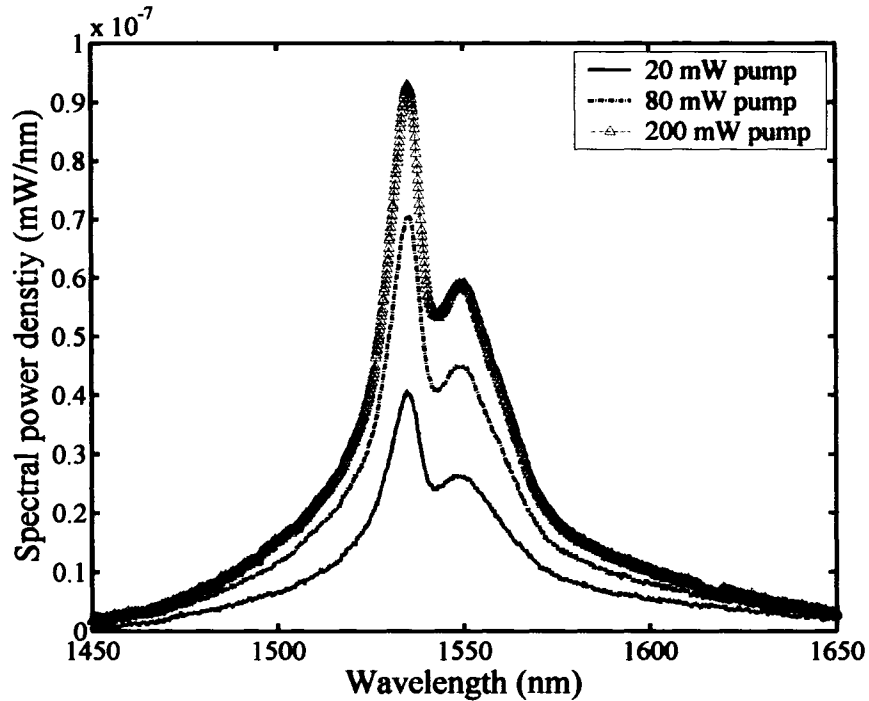


Figure 4.15: Photoluminescence from *SPPM* waveguides collected using the setup shown in Fig. 4.14. The PL strength does not follow the pumping strength in a linear fashion, indicating some form of saturation.

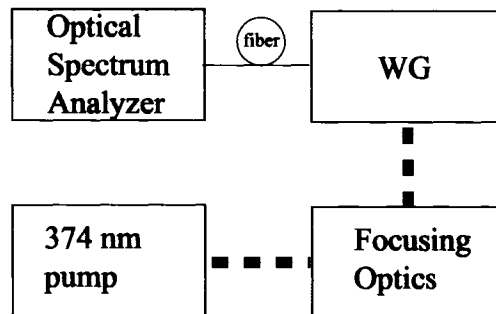


Figure 4.16: A setup used to collect waveguide photoluminescence. The waveguide is pumped using a diode laser operating at  $374 \text{ nm}$ . The laser is focused into a stripe covering the length of the waveguide.

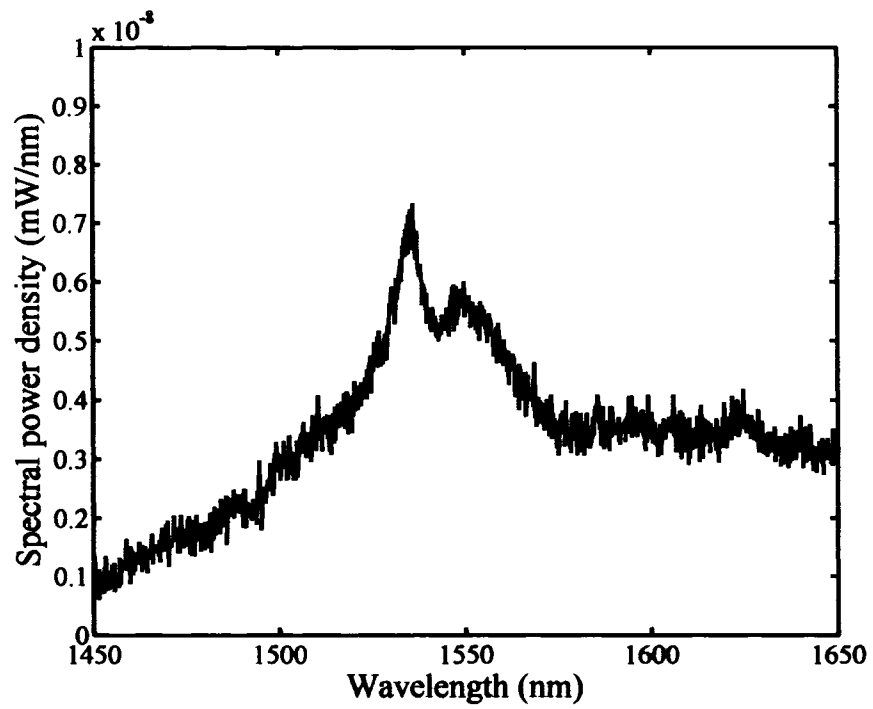


Figure 4.17: Photoluminescence from *SPPM* waveguides collected using the setup shown in Fig. 4.16. The typical erbium profile can be seen.

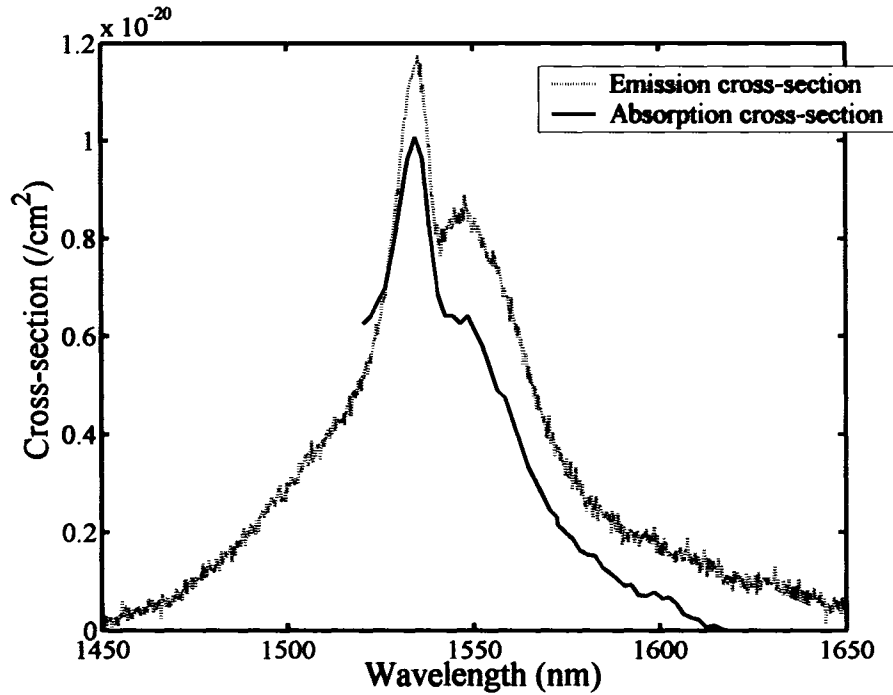


Figure 4.18: Absorption and emission cross-sections for waveguides of the *SPPM* process. The emission cross-section is produced by using the photoluminescence curves in Fig. 4.15, and by assuming a radiative lifetime of 3 *ms* in line with the work of Hryciw et al [20].

and predicted emission cross-section are shown overlaid in Fig. 4.18.

### 4.5.3 Nonlinear Transmission

One of the simpler experiments performed was an input-output type experiment. A schematic of the experimental setup is shown in Fig. 4.11. Either a tunable laser or a high-powered 1480 *nm* laser was used as a probe. Referring to Fig. 4.11, if the laser power is increased by a certain percentage it follows that the power at both the measured outputs,  $P_{PD1}$  and  $P_{PD2}$ , should increase by the same percentage. The ratio, then of  $P_{PD2}/P_{PD1}$  should be a constant. This will not be the case if the waveguide transmission is a function of intensity. This experiment was conducted on both doped and un-

doped waveguides at a wavelength of 1480 *nm*, and at 1620 *nm* for the doped waveguide only. Fig. 4.19 shows the the ratio  $P_{PD2}/P_{PD1}$  plotted against the monitor power,  $P_{PD1}$ . The undoped waveguide response seems very linear. Both doped waveguide experiments, however, reveal significant nonlinearity. The waveguide transmission at 1480 *nm* was much more nonlinear than that at 1620 *nm*. The fact that the nonlinearity is present in doped waveguides but not in undoped waveguides suggests that the effect is not an artifact of the testing system. It also suggests that the mechanism is likely related to the erbium doping. It is possible that photons in the metastable erbium level could re-excite a nanocluster by backtransfer. This would correspond to the reverse of the processes displayed in Fig. 1.3. The nonlinearity could then be exacerbated by confined carrier absorption, which is a documented process discussed in Sec. 4.5.4. CCA is an absorption process which depends on the density of free carriers or excitons, which in turn depends on the pumping strength generating the free carriers or excitons. This could explain why higher transmission power causes higher losses in the waveguide. The doped-waveguide nonlinear transmission seen at 1480 *nm* may be higher than that seen at 1620 *nm* due to the far higher absorption cross-section of erbium at 1480 *nm*.

#### 4.5.4 Optical Pumping of Waveguides

Optical pumping of erbium-doped waveguides is done to raise ground state erbium ions into their metastable level. This creates the potential for optical amplification if more than 50 % of the erbium ions can be excited to the metastable level. Erbium ions can be excited to their metastable level by pumping one of the erbium ion's absorption bands. Typical pumping bands are the  ${}^4I_{9/2}$  band (800 *nm*),  ${}^4I_{11/2}$  band (980 *nm*), and the  ${}^4I_{13/2}$  band (1480 *nm*). Pumping to any of these levels will cause a build-up in the metastable  ${}^4I_{13/2}$  band, as the Er ions quickly relax to the long-lived  ${}^4I_{13/2}$  level. Within Er:SiO, an indirect mechanism of erbium excitation is evident.

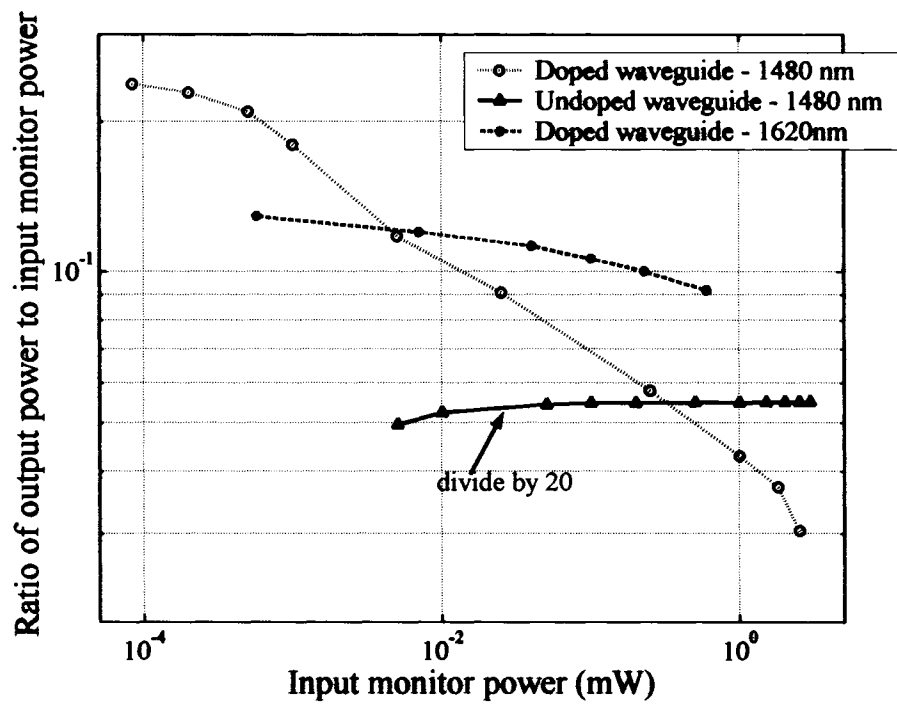


Figure 4.19: Ratio of  $P_{PD2}/P_{PD1}$  plotted against  $P_{PD1}$ . The undoped waveguide response is approximately linear. The doped waveguide shows significant nonlinearity. This could be a form of excited state absorption, or backtransfer mechanism.



Excitons within silicon nanoclusters can transfer their energy to erbium ions (see Sec. 1.3), which also leads to population build-up in the metastable  $^4I_{13/2}$  erbium band. Excitation of erbium ions by the silicon nanoclusters may allow for a reduction in required pump power, and a reduction of the costs associated with pumping equipment. Si nanoclusters have a broad absorption band in the UV-Vis region, with absorption cross-sections up to 5 orders of magnitude higher than erbium [20]. In the following sections, pumping of Er:SiO waveguides is conducted using 532 nm, 980 nm, and 1480 nm wavelength pump sources.

### **Optical Pumping with 532 nm light**

A frequency-doubled Nd:YAG laser operating at 532 nm was employed for transverse optical pumping of waveguides from the *SPPM* process. Er:SiO absorption at 532 nm is shown in the inset of Fig. 4.1(a). Absorption approx. 1 dB/ $\mu\text{m}$ . A tunable probe laser was coupled into the waveguide and the transmitted power was collected using an objective lens and germanium photodetector. The polarization condition of the probe beam was controlled using a fiber polarization controller (*PC*). Focusing optics were used to form the pump beam into a line covering the length of the waveguide. The pumping beam dimensions were estimated by creating an optical beam line with the beam projected onto a beam analyzer as seen in Fig. 4.20(a). The beam analyzer measures the beam profile and gives information on the beam widths in orthogonal directions. A beam area was defined by the product of the  $1/e^2$  beam widths. The total beam power was measured by replacing the beam analyzer with a photodetector. The beam intensity was then estimated by dividing the beam power by the beam area. The distances between each of the elements of the beam line were recorded. The optical beam line was then recreated so as to project onto waveguide samples as seen in Fig. 4.20(b). Each of the distances was kept constant, so that the beam was the same in the pumping experiment as in the beam measurement. Neutral density filters

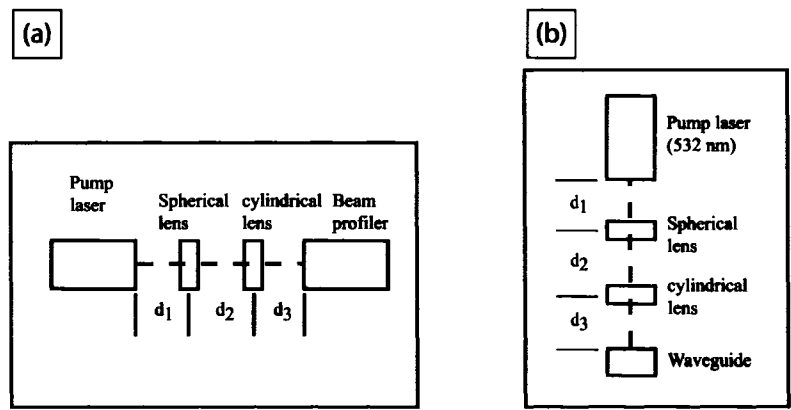


Figure 4.20: The method used to estimate the 532 nm pump beam size. (a) An optical beam line is formed, and the beam projected onto a mode analyzer. The distances between each of the elements of the beam line were recorded. (b) The optical beam line is recreated but is now projected onto a waveguide.

were placed into the beam line before the focusing optics to attenuate the pump beam. A schematic of the setup is shown in Fig. 4.21. A reference scan was taken of the system with no pumping and with the waveguide removed. Scans taken with the waveguide were subsequently divided by the reference scan to remove the spectral response of other elements in the system. The procedure is similar to that described in Section 4.4.1.

For each pump intensity, a broadband scan in the 1520 nm - 1620 nm region was collected. Upon pumping, two mechanisms acted simultaneously

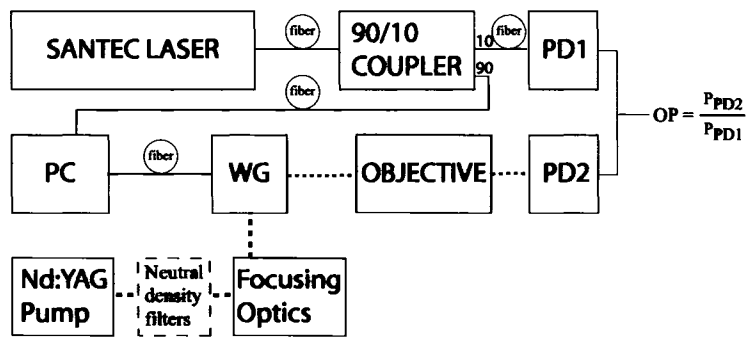


Figure 4.21: The setup used to collect broadband spectral data under transverse 532 nm pumping.

on the spectral response of the waveguide. The first mechanism is a broad, featureless, loss mechanism. This has been ascribed to CCA, which has been documented in other work on Er:SiNC:SiO<sub>2</sub> glasses [31, 17, 32]. Pumping of undoped waveguides also revealed CCA effects. This may indicate that the CCA has little to do with erbium doping, but that carriers produced within nanoclusters have broad absorption bands which cover at least the 1.3  $\mu m$  to 1.6  $\mu m$  spectral range. The second mechanism is the erbium ion emission. By dividing the data as in eqn. 4.8, the signal change,  $\Delta_{signal}$  is extracted, where  $I_p$  is the pump intensity,  $\lambda$  is the wavelength, and  $T(\lambda, I_p)$  is the transmission for a given pump intensity and wavelength. To examine only the portion of  $\Delta_{signal}$  caused by the erbium emission (the erbium-related signal change, ERSC), each of the curves obtained using eqn. 4.8 are scaled so that their minima are equal. Eqn. 4.9 shows how ERSC is derived from the raw data. This should be acceptable since each minimum is at approx. 1620  $nm$  where the erbium ion has nearly no effect. All of the  $\Delta_{signal}$  at 1620  $nm$  can therefore be attributed to CCA. ERSC can be described in terms of the peak erbium absorption,  $\alpha_{peak}$ , the total erbium population,  $N_{ERB}$ , and the erbium metastable population,  $N_2$ , and is shown in eqn. 4.10

$$\Delta_{signal}(\lambda, I_p) = \frac{T(\lambda, I_p)}{T(\lambda, 0)} \quad (4.8)$$

$$ERSC(\lambda, I_p) = \frac{T(\lambda, I_p)T(1620nm, 0)}{T(\lambda, 0)T(1620nm, I_p)} \quad (4.9)$$

$$\frac{ERSC}{2\alpha_{peak}} = \frac{N_2}{N_{ERB}} \quad (4.10)$$

Fig. 4.22 (a) shows the broadband data collected using the setup in Fig. 4.21, for different transverse pump intensities. Fig. 4.22 (b) shows the ERSC of the waveguide pumped by 532  $nm$  light.

The amount of erbium inversion can be directly assessed using the ERSC information. The maximum possible ERSC occurs when there is a complete

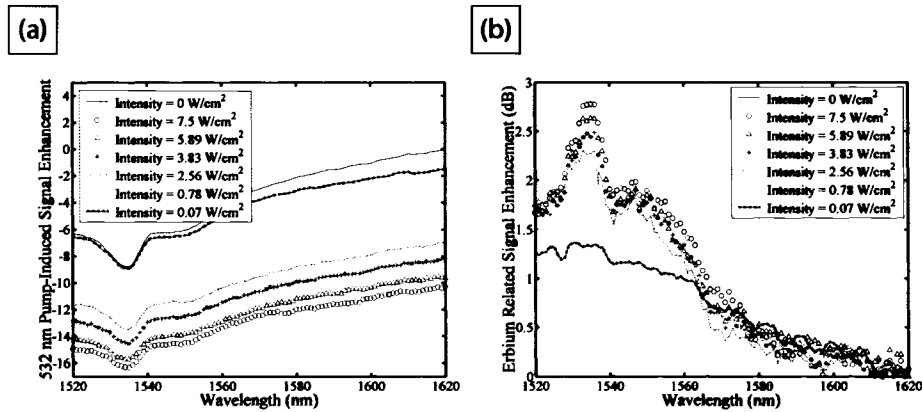


Figure 4.22: (a) Broadband curves obtained under transverse 532 nm pumping. The data was collected using the setup shown in Fig. 4.21, and using a 4 mm long waveguide from the *SPPM* process. Each curve is taken at a different pump intensity. A description of how the pump intensity was calculated can be found in the text. The curves are affected by confined carrier absorption (CCA) and by erbium ionic emission. (b) Pump-induced change in the curves from (a) due to erbium-ion emission. The effect of CCA has been removed for clarity.

population inversion. This would mean that 100 % of erbium ions had been excited to the metastable level ( $N_2/N_{ERB} = 1$ ). This would also correspond to the point where the ERSC had reached twice the value of the erbium-related absorption. For a material with 7 dB/cm peak erbium-related absorption, the maximum ERSC would be 14 dB/cm. By noting the amount of ERSC for each pump intensity, the inversion level for each pump intensity can be calculated using eqn 4.10. Fig. 4.23 shows the erbium inversion condition plotted as a function of pump intensity. It is apparent that the erbium inversion saturates near an inversion level of approx. 20 %. It is possible that the nanoclusters only sensitize approx. 20 % of the erbium. It is also possible that only approx. 20 % of the erbium is optically active. Given the estimated concentration of erbium of approx. 1 at. % (approx.  $6 \times 10^{20} / \text{cm}^3$ ) in the waveguides under test, a high percentage of erbium may be in a clustered state or otherwise deactivated.

Given the estimated erbium concentration of  $6 \times 10^{20} / \text{cm}^3$  for the post

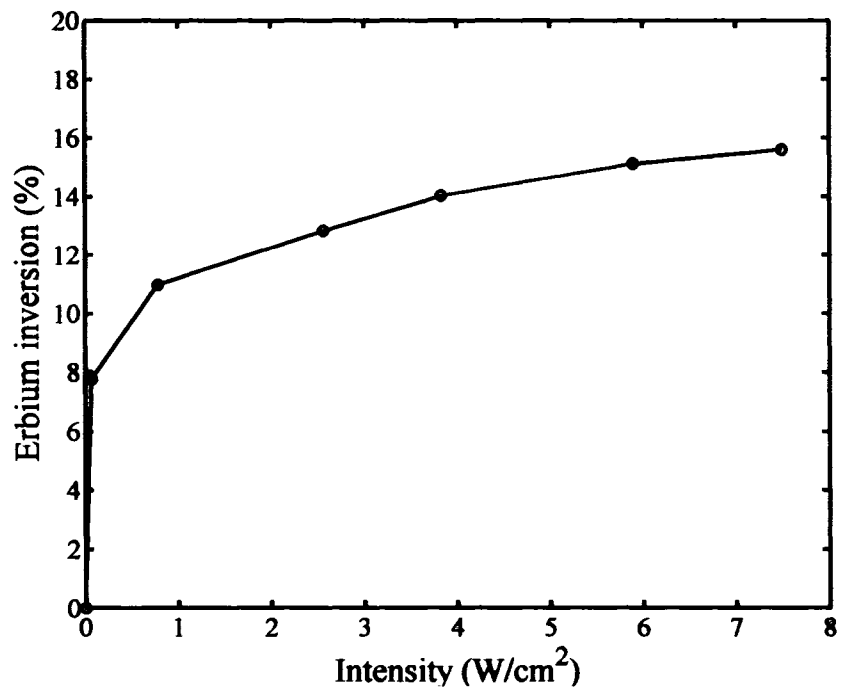


Figure 4.23: Percentage of total erbium in the metastable state plotted against transverse pump intensity. The inversion level seems to saturate at an inversion level of approx. 20 %.

waveguides tested, the approximate nanocluster density of  $2 \times 10^{19} / \text{cm}^3$ , and the maximum inversion level of approx. 20 %, each nanocluster excites approx. 4 – 5 erbium ions at maximum pump intensity.

### **Optical Pumping with 980 nm light**

Pumping at 980 nm was conducted in an attempt to further investigate the amount of excitable erbium. Due to the low absorption cross-section of the erbium ion in the 980 nm region, the pump was co-propagated with the signal. The waveguide was from the *SPPM* process, as was the case for experiments conducted with the 532 nm pump. A schematic of the setup used to collect data is shown in Fig. 4.24. The tunable probe laser was amplitude modulated in a fiber-freespace-fiber setup using SELFOC lenses, and an optical chopper wheel. The 980 nm pump beam is added via a 980/1550 nm wavelength division multiplexer (WDM). The beams are coupled into a waveguide, and are collected at the output using an objective lens focused onto a germanium detector. In theory, the lock-in amplifier should filter out all of the pump light. However, the signal is originally coupled into the lock-in amplifier as a DC signal. High-power pump light was observed to overload the input stage of the lock-in, preventing proper data collection. To overcome this problem, a scattering silicon filter was constructed using 2 pieces of single-side polished (SSP) silicon. The filter was placed in front of the germanium detector to attenuate 980 nm light. A double-side polished (DSP) silicon filter was originally used, but lead to Fabry-Perot resonance in the spectral response. The filter provided an attenuation of approx. 26 dB at 980 nm and approx. 13 dB at 1550 nm. Using a second fiber to collect light at the output of the waveguide was another option considered. This would allow a second WDM to de-multiplex the remaining 980 nm light. Unfortunately, cleaving proper facets has been a consistent problem in the *SPPM* process. A gap was always left between the end of the waveguide and the fiber at the second fiber coupling point, which led to Fabry-Perot

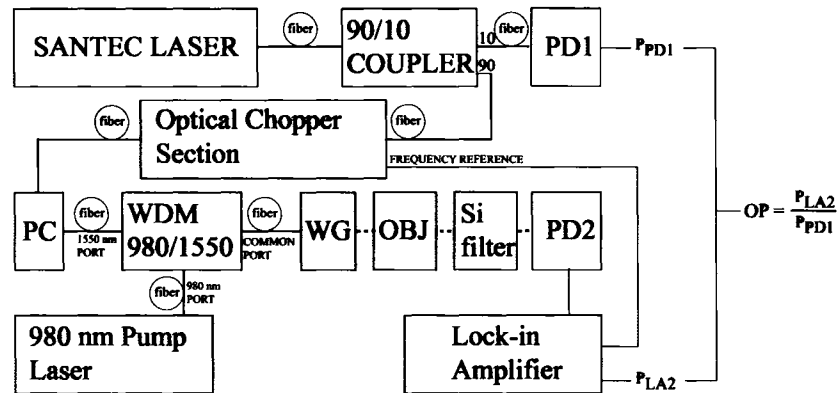


Figure 4.24: The setup used to collect broadband spectral data under co-directional 980 nm pumping.

resonance.

A reference scan of the system was taken without the waveguide and was used to remove the spectral response of elements other than the waveguide. The reference was taken at full pump power and at zero pump power to ensure that there was minimal pump-induced change to the system. Under heavy pumping a reduction in signal strength of approx. 9 % was consistently observed. This was speculatively attributed to non-linearity in the WDM at high powers. Various pump powers were selected, and a broadband scan was taken for each power. Fig. 4.25 (a) shows the broadband data collected for each pump power. Fig. 4.25 (b) shows the ERSC for the 980 nm experiment. Slight differences in the overall shape of the erbium absorption profile is evident in this experiment compared to the 532 nm pumping experiment. This was difficult to explain; it is possibly arises from the use of the lock-in amplifier in one case but not the other.

The erbium inversion condition versus incident 980 nm pump power was estimated, and is shown in Fig. 4.26. It is clear that the inversion level saturates for low pump power, and approaches a maximum inversion level of approx. 20 %, as was found for 532 nm pumping. Since both pump configurations result in similar maximum erbium inversion level, it is very

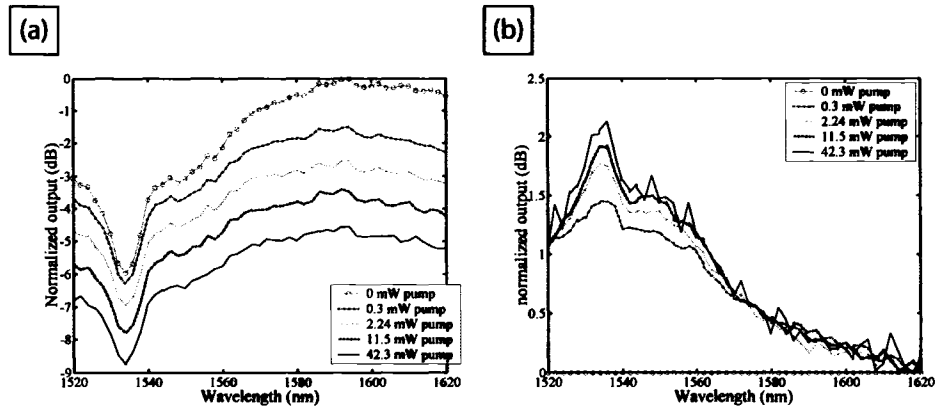


Figure 4.25: (a) Broadband curves obtained under transverse 532 nm pumping. The data was collected using the setup shown in Fig. 4.21. Each curve is taken at a different pump intensity. The curves are affected by confined carrier absorption (CCA) and by erbium ionic emission. (b) Pump-induced change in the curves from (a) due to erbium-ion emission. The effect of CCA has been removed for clarity.

likely that approx. 80 % of the erbium in the thin film is inactive. The most likely cause of the erbium inactivity is clustering of this fraction of the erbium ions [55]. The level of CCA incurred for combinations of pump wavelength, pump intensity, and signal wavelength is shown in Fig. 4.27.

### Optical Pumping with 1480 nm light

Pumping was also conducted with 1480 nm light. Again, since the absorption cross-section for 1480 nm light is very low, the pump was co-propagated the probe signal. This experiment was more difficult to implement than the 980 nm experiment because no suitably selective filter for blocking 1480 nm while passing 1520 nm probe light was available. This allowed more pump light to exit the waveguide and impinge on the photodetector, *PD2*. The lock-in amplifier was again used to filter out the pump light. However, the overall signal level of combined pump and probe had to be significantly attenuated (over 40 dB) so that it did not overload the front-end of the lock-in amplifier. This resulted in very low probe signal power at the detector. A schematic



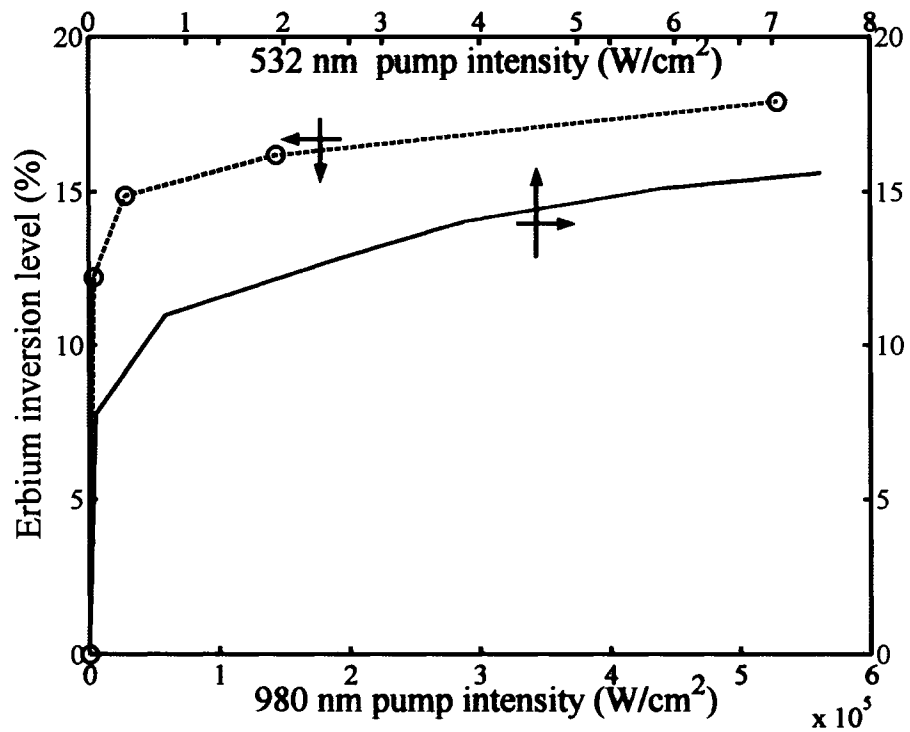


Figure 4.26: Percentage of total erbium in the metastable state plotted against pump power. The results for 532  $nm$  pumping are plotted alongside the results for 980  $nm$  pumping for comparison. The inversion level for both pumping wavelengths seems to saturate at an inversion level of approx. 20 %.

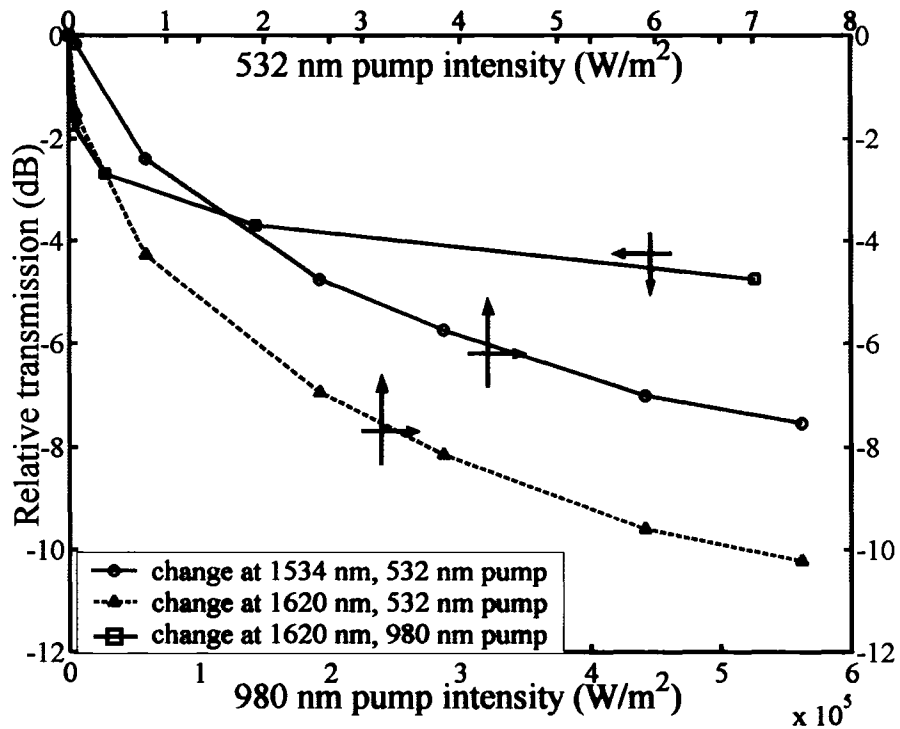


Figure 4.27: Plots of confined carrier absorption for different combinations of signal and pump wavelengths and pump intensities. The blue curve (squares) shows the effect of 980 nm pump light on signal light at 1620 nm. The CCA reaches a level of approx.  $-5$  dB. The light green curve (triangles) shows the CCA incurred for a pump wavelength of 532 nm and a signal wavelength of 1620 nm. The CCA reaches a level of approx.  $-10$  dB. The dark green curve (circles) is similar to the conditions for the light green curve except the signal wavelength is set at 1534 nm. The difference between the light green curve and the dark green curve is due to the erbium emission.

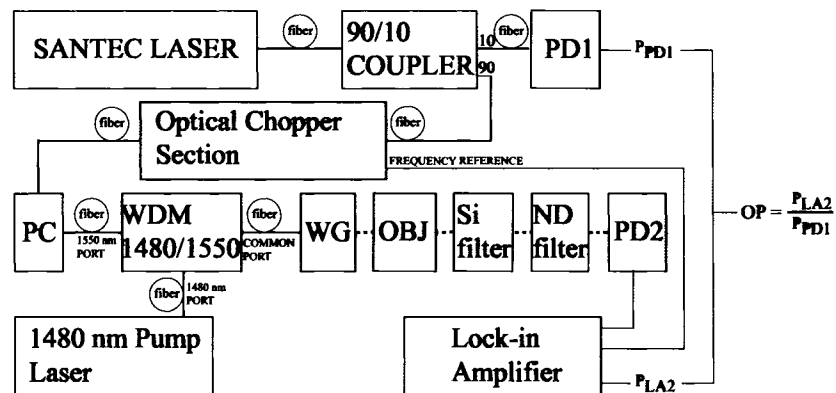


Figure 4.28: The setup used to collect broadband spectral data under co-directional 1480 nm pumping.

of the setup is shown in Fig. 4.28. It is identical to that used for the 980 nm experiment except that a neutral density filter (*ND*) is added after the SSP silicon filter (*Si filter*). The results of the pumping experiment were intriguing. Fig. 4.29 (a)-(b) shows broadband scans and signal change of the Er:SiO under 1480 nm pumping. Parts (c)-(d) are higher resolution scans taken in the 1520 nm to 1560 nm range. It can be seen that as the pump intensity is increased to 1.2 mW, signal enhancement in the 1530 nm to 1540 nm range is achieved. As the pump is increased further, signal enhancement is lost. However, a peak centered at approx. 1534 nm begins to emerge. The peak increases with pump strength, and seems to undergo spectral narrowing, which can be indicative of the onset of lasing [56]. This is not a probable explanation for the data in Fig. 4.29, since it is very clear that no signal enhancement is occurring at high pump powers where the narrowing effect is most pronounced. Net signal enhancement is a requirement for optical amplification and lasing. A second fiber coupler was aligned at the second facet of the waveguide, and was used to couple pump-induced spontaneous emission into an OSA. The OSA spectrum did not show any of the spectrum narrowing features visible in the 1534 nm region. The result was repeatable using the setup in 4.28, however, making it difficult to explain. It is possible

that it is a spurious system effect arising from one of the system components.

## 4.6 Discussion of Experimental Results

From Sections 4.2, 4.3, and 4.4, there is evidence that good quality passive integrated optic elements can be fabricated in silicon monoxide. Low propagation losses, high index of refraction contrast, and compatibility with silicon support this argument. Section 4.5, however, provides evidence that optical amplification in Er:SiO may be difficult to achieve. A few key observations from Results show that the material suffers from a pair of problems. The first problem is CCA, which provides for high levels of excess loss in each pumping region attempted. The second problem is the high level of inactive erbium in the glass. Since only approx. 20 % of erbium can be excited to the metastable level, it is likely that the performance is suffering from problems due to high concentration. A third problem is backtransfer of energy from erbium ions to the nanoclusters. A few observations support the claim of backtransfer in the glass:

1. Pumping doped and undoped waveguides with 532 *nm* light causes CCA.
2. Pumping undoped waveguides at 1480 *nm* does not cause nonlinear processes such as CCA.
3. Pumping doped waveguides at 1480 *nm* does cause a nonlinear process, which is likely CCA.

Since the only difference in the undoped waveguide pumping experiments is the wavelength of the pump, it is likely that the nanoclusters have approx. zero absorption cross-section at 1480 *nm*, and that CCA is caused by excitons generated in the nanoclusters. Since the CCA has been attributed

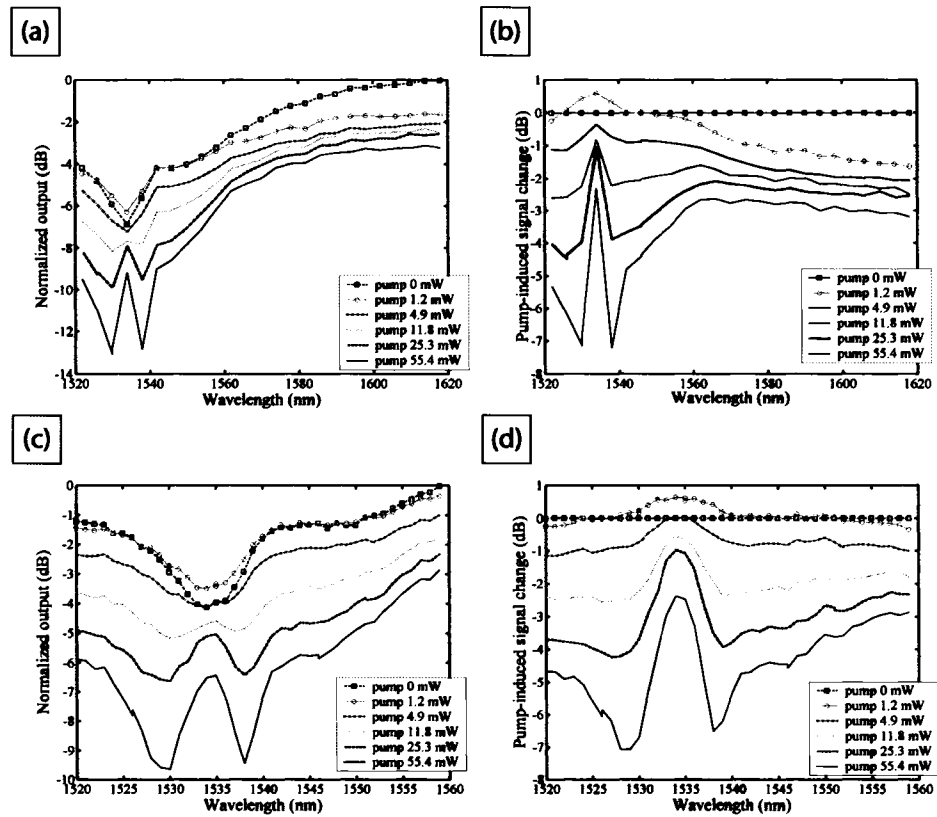


Figure 4.29: (a) Broadband scans of a waveguide from the *SPPM* process under different 1480 nm pumping intensities. (b) signal change of the waveguide spectral response under pumping. (c) broadband scans in the spectral range 1520 nm to 1560 nm. Signal enhancement can be clearly seen for low pump powers. (d) Higher resolution plot of the signal change of the Er:SiO under increasing 1480 nm pumping. A feature centered around 1534 nm develops as the pump strength is increased. The feature seems like spectrum narrowing, an onset to lasing.

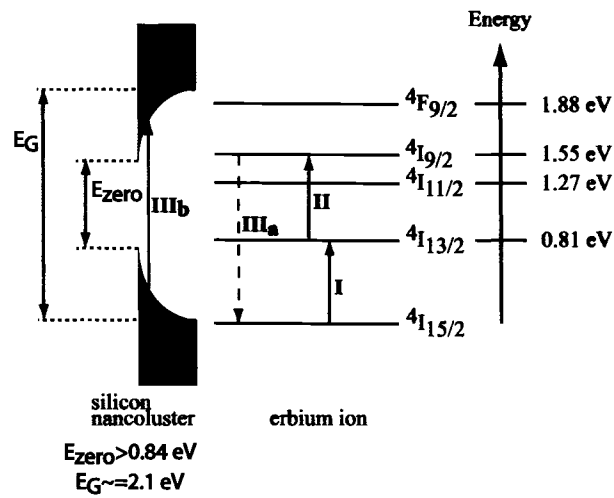


Figure 4.30: Energy diagram showing one route to backtransfer of energy from the erbium ion to the silicon nanocluster under 1480 nm pumping. As can be seen on the left, the bandtails effectively terminate leaving a gap,  $E_{zero}$ , greater than 0.84 eV (the pump energy). First, an erbium ion is excited to the metastable  $4I_{15/2}$  level (event I). Second, this electron is promoted to a higher state through either excited state absorption or upconversion (II). Finally, the erbium electron de-excites ( $III_a$ ) and creates an exciton within the silicon nanocluster ( $III_b$ ).

to the presence of excitons within the nanoclusters, and since excitons are not directly generated within nanoclusters under 1480 nm light, it is likely that the presence of erbium allows for a backtransfer route for creating excitons within nanoclusters, and the associated CCA. A possible mechanism is shown in Fig. 4.30. It should be noted that the undoped waveguide used in section 4.5.3 had much higher propagation losses than the doped waveguide, and that this experiment should be re-attempted using undoped waveguides with lower propagation losses.

# Chapter 5

## Conclusion

### 5.1 Summary of Results

This MSc project was conceived to test the feasibility of Er:SiO as an optical amplifying medium. Er:SiO is a member of the family of materials commonly referred to as either silicon-rich oxides (SRO) or erbium-doped silicon nanocluster-doped silicon dioxides (Er:SiNC:SiO<sub>2</sub>). The Er:SiO films studied here contain a high density of small (2 – 3 nm diameter) amorphous silicon nanoclusters (SiNC). SiNC have a large absorption cross-section in the UV-visible light region, and can transfer energy to nearby erbium ions.

Some key results of this work include:

- SiO was evaluated as a waveguiding material for the first time.
  1. The index of refraction of annealed silicon monoxide films was measured and an index of 1.9 at 1530 nm wavelength was verified.
  2. Both wet and dry etching processes were developed for SiO.
  3. Strip waveguides, strip-loaded waveguides, and rib-loaded waveguides were fabricated.
  4. Strip waveguides exhibited losses as low as 0.5 dB/cm at 1300 nm wavelength.

- Efficient non-resonant excitation of erbium ions was demonstrated.
  1. Er:SiO waveguides were pumped at 532 *nm* and at 374 *nm* in a transverse arrangement.
  2. Low transverse pump intensities saturated the erbium inversion level.
  3. The upper limit on the erbium inversion was approx. 20 %.
  4. The inversion limit was likely due to erbium clustering since both resonant and non-resonant pumping led to the same maximum inversion level.
  5. Approx. 5 erbium ions were excited per nanocluster.
  
- Er:SiO was tested as an optical amplification material.
  1. The  ${}^4I_{15/2}$  to  ${}^4I_{13/2}$  absorption and emission cross-sections were characterized and were in line with some work in the literature [32, 53].
  2. Waveguides were pumped non-resonantly at 532 *nm* and resonantly at 980 *nm* and 1480 *nm*, and transmission measurements were taken at different pumping intensities.
  3. Erbium-related signal enhancement (ERSC) was observed and recorded at all pump wavelengths and pump strengths.
  4. Confined carrier absorption (CCA) was observed and recorded for all pump wavelengths and pump strengths.
  5. Signal enhancement was observed for low power 1480 *nm* pump intensity.

Undercladding thickness and waveguide dimensions were specified for waveguides using Er:SiO as a core material. Various waveguide fabrication processes were attempted. Eventually, three highly flexible fabrication processes were deemed successful. These include the silicon post prefabrication



method (*SPPM*, see Sec. 3.3.1), the silicon dioxide ribload process (see Sec. 3.3.2), and the SU8 photopatterned stripload process (see Sec. 3.3.3). Each of these processes should be insensitive to the experimental material being deposited, so long as experimental materials are thermo-mechanically compatible with the cladding layer. Waveguides were fabricated based predominantly on the *SPPM* process, and losses as low as  $0.5 \text{ dB/cm}$  were demonstrated. Due to short waveguide lengths, error estimates are high. Waveguides from this process also support multiple modes, which complicates most analyses.

The ribload process is a far simpler process than the *SPPM* process. It requires fewer processing steps, allows for easy design of single-mode waveguides, and will likely allow for much easier cleaving and characterization. Groups that have previously fabricated waveguides using Er:SiNC:SiO<sub>2</sub> materials include: Kik and Polman [17], Daldosso et al. [32], Nishii et al. [31], and Han et al. [57]. Each of these groups, except Kik and Polman, reported on the losses of their waveguides. Daldosso et al. [32] claimed transmission losses as low as  $2 \text{ dB/cm}$  at  $1600 \text{ nm}$  wavelength, though, the authors somewhat arbitrarily assigned a large portion of the total measured insertion losses to coupling losses and coupling errors. Han et al. reported bulk optical losses (background losses) of approx  $4 \text{ dB/cm}$  at  $1.54 \mu\text{m}$ . Nishii et al. conducted broadband transmission measurements on erbium-doped films [31], reporting transmission losses as low as  $6.5 \text{ dB/cm}$  at approx.  $1600 \text{ nm}$  wavelength. In this work, we have found losses as low as  $0.5 \text{ dB/cm}$  at  $1300 \text{ nm}$  wavelength. The waveguide losses in this work are as good or better than other published data for *SiO<sub>x</sub>* materials, in spite of their higher core-cladding index offset. The low losses may be attributable to the homogeneity of our low-temperature processed material, and to superior fabrication techniques.

The  ${}^4I_{15/2}$  to  ${}^4I_{13/2}$  absorption cross-section in Er:SiNC:SiO<sub>2</sub> materials is a parameter which has caused much controversy due to early reports of high values of this parameter with respect to values in other silicate glasses [17, 54]. Some of the initial reports have now been refuted [53], and recent

Group	Excess silicon (at. %)	Type	Measured cross-section ( $cm^2$ )	$\lambda$ (nm)	Reference
Wang et al.	0	emission	$5.4 \times 10^{-21}$	1535	[58]
Mertens et al.	10	absorption	$8 \pm 2 \times 10^{-21}$	1536	[53]
Daldosso et al.	16	absorption	$5 \pm 2 \times 10^{-21}$	1534	[32]
Shin et al.	1-2.5	emission	$6 \times 10^{-20}$	1533	[59]
This work	25	absorption	$1 \times 10^{-20}$	1534	This work

Table 5.1: Measured cross sections of the  ${}^4I_{15/2}$  to  ${}^4I_{13/2}$  transition. The type of cross-section and the peak cross-sectional wavelength are also listed.

work has shown this parameter to be more in line with cross-sectional values of erbium-doped silicon dioxide [32, 53, 58]. The value determined from this work is approx.  $1 \times 10^{-20}$  ( $cm^2$ ) at 1534 nm, which is approx. 2 times the cross-sectional value in erbium doped silicon dioxide. Table 5.1 lists either the absorption or emission cross-sectional values reported by groups working in the area. Peak absorption and emission cross-sections are often assumed equal [5].

Pumping of the waveguides at 532 nm, 980 nm, and 1480 nm was performed in order to explore the erbium inversion condition and attempt waveguide amplification in the 1.5  $\mu m$  band. At each wavelength, significant CCA was evident, which is in line with other work on (Er:SiNC:SiO<sub>2</sub>) materials [17, 32]. The work of Han et al., and Shin et al. [54, 59], however, is notably different since it shows very little CCA. The work by Nishii et al. [31] shows that as the excess silicon concentration is increased from 1 mol. % to 2 mol. %, CCA increases dramatically. The fact that CCA is present in our 1480 nm experiment likely indicates the presence of backtransfer from erbium ions to the silicon nanoclusters (see Section 4.6). The pumping experiments at 532 nm, and 980 nm showed an inversion saturation at approx. 20 % erbium inversion. Given the high erbium concentration of approx. 1 at. %, this likely indicates that approx. 80 % of the erbium is non-invertible due to clustering.

The results of this thesis indicate that there is potential for high-index-contrast passive integrated optics in materials based on SiO. However, the stoichiometry used here (with approx. 1 at. % erbium) will not suffice as an amplification material due to the unfavourable CCA, and the erbium inversion limitations.

## **5.2 Suggested Future Work**

### **5.2.1 Analysis of Loss in SiO Waveguides**

A key task for future work is the further characterization and clarification of SiO waveguide losses. Fabrication of waveguides a few cm in length or longer would significantly reduce the uncertainty in estimations of loss. Waveguides based on the ribload process (see Sec. 3.3.2) will likely also provide for easily obtained high quality end-facets and single-mode operation. These two characteristics should allow the use of the Fabry-Perot characterization method, which provides the propagation losses independent of the coupling condition.

### **5.2.2 Further Exploration of SiO as an Erbium Host**

There is still much information that can be obtained based on glasses fabricated using SiO as an erbium host. Waveguides with a reduced erbium concentration should be fabricated to determine whether higher erbium inversion conditions can be achieved. This would likely indicate that (at least in part) the high erbium concentration is leading to deactivation of some of the erbium ions. Also, aluminum doping of the experimental material could be explored to investigate whether it allows for a higher active erbium fraction [60]. The exploration of how CCA scales with erbium concentration could provide valuable insight as to whether CCA and erbium concentration are at all correlated. Annealing cycles for this work involved a 1 hour cycle time at

a temperature of 500 °C. This cycle was selected because it maximizes the material's photoluminescence intensity. However, it is not necessarily true that optical amplification is optimized with the same annealing cycle. A different annealing cycle may provide more favourable conditions for optical amplification.

### 5.2.3 Fabrication Using Other Hosts

In order for erbium-doped silicon nanoparticle glasses to have potential as optical amplifiers, materials must be optimized for reduced CCA, and for higher potential erbium inversion. The characterization of materials with a reduced silicon content, such as  $SiO_{1.8}$ , may reduce CCA based simply on the lower amount of available silicon. The amount of excess silicon will likely lead to a decrease in the nanoparticle density in the glass. By exploring the dependence of CCA on silicon content, and potential erbium inversion on erbium content, trends or regions may be uncovered where optical amplification is favourable in Er:SiNC:SiO<sub>2</sub> glasses.

# Bibliography

- [1] D. Zimmerman and L. Spiekman, “Amplifiers for the masses: EDFA, EDWA, and SOA amplifiers for metro and access applications,” *Journal of Lightwave Technology*, vol. 22, no. 1, pp. 63–70, 2004.
- [2] K. Ennsner, G. D. Valle, M. Ibsen, J. Shmulovich, and S. Taccheo, “Erbium-doped waveguide amplifier for reconfigurable WDM metro networks,” *IEEE Photonics Technology Letters*, vol. 17, no. 7, pp. 1468–1470, 2005.
- [3] R. DeCorby, N. Ponnampalam, M. Pai, H. Nguyen, P. Dwivedi, T. Clement, C. Haugen, J. McMullin, and S. Kasap, “High index contrast waveguides in chalcogenide glass and polymer,” *IEEE Journal of Selected Topics in Quantum Electronics*, vol. 11, no. 2, pp. 539–546, 2005.
- [4] S. Saini, J. Michel, and L. Kimerling, “Index contrast scaling for optical amplifiers,” *Journal of Lightwave Technology*, vol. 21, no. 10, pp. 2368–2376, 2002.
- [5] M. Yamane and Y. Asahara, *Glasses For Photonics*. Cambridge University Press, 2000.
- [6] M. Weber, Ed., *Handbook of Lasers*. CRC Press, 2001.

- [7] A. Polman and F. van Veggel, "Broadband sensitizers for erbium-doped planar optical amplifiers: review," *Journal of the Optical Society of America B*, vol. 21, no. 5, pp. 871–892, May 2004.
- [8] F. Patel, S. DiCarolis, P. Lum, S. Venkatesh, and J. Miller, "A compact high-performance optical waveguide amplifier," *IEEE Photonics Technology Letters*, vol. 16, no. 12, pp. 2607–2609, December 2004.
- [9] G. D. Valle, S. Taccheo, P. Laporta, G. Sorbello, E. Cianci, and V. Foglietti, "Compact high gain erbium-ytterbium doped waveguide amplifier fabricated by the Ag-Na ion exchange," *Electronics Letters*, vol. 42, no. 11, pp. 632–633, 25 May 2006.
- [10] S. Iyer and Y.-H. Xie, "Light emission from silicon," *Science*, vol. 260, no. 5104, pp. 40–46, 2 April 1993.
- [11] A. Kenyon, "Erbium in silicon," *Semiconductor Science and Technology*, vol. 20, pp. R65–R84, 2005.
- [12] A. Polman, "Erbium implanted thin film photonic materials," *Journal of Applied Physics*, vol. 82, no. 1, pp. 1–39, July 1997.
- [13] A. Kenyon, "Quantum confinement in rare-earth doped semiconductor systems," *Current Opinion in Solid State and Materials Science*, vol. 7, pp. 143–149, 2003.
- [14] K. Imakita, M. Fujii, Y. Yamaguchi, and S. Hayashi, "Interaction between *Er* ions and shallow impurities in *Si* nanocrystals within *SiO<sub>2</sub>*," *Physical Review B*, vol. 71, p. 115440, 31 March 2005.
- [15] G. N. van den Hoven, J. H. Shin, A. Polman, S. Lombardo, and S. U. Campisano, "Erbium in oxygen-doped silicon: Optical excitation," *Journal of Applied Physics*, vol. 78, no. 4, pp. 2642–2650, 15 August 1995.

- [16] D. Adler, D. C. Jacobson, D. J. Eaglesham, M. A. Marcus, J. L. Benton, J. M. Poate, and P. H. Citrin, “Local structure of 1.54- $\mu\text{m}$ -luminescence  $\text{Er}^{3+}$  implanted in  $\text{Si}$ ,” *Applied Physics Letters*, vol. 61, no. 18, pp. 2181–2183, 2 November 1992.
- [17] P. Kik and A. Polman, “Gain limiting processes in  $\text{Er}$ -doped  $\text{Si}$  nanocrystals waveguides in  $\text{SiO}_2$ ,” *Journal of Applied Physics*, vol. 91, pp. 534–536, January 2002.
- [18] J. Lee, Shin, J.H., and N. Park, “Optical gain at 1.5  $\mu\text{m}$  in nanocrystal  $\text{Si}$ -sensitized  $\text{Er}$ -doped silica waveguide using top-pumping 470 nm LEDs,” *Journal of Lightwave Technology*, vol. 23, no. 1, pp. 19–25, January 2005.
- [19] M. Fujii, M. Yoshida, Y. Kanzawa, S. Hayashi, and K. Yamamoto, “1.54 $\mu\text{m}$  photoluminescence of  $\text{Er}^{3+}$  doped into  $\text{SiO}_2$  films containing  $\text{Si}$  nanocrystals: Evidence for energy transfer from  $\text{Si}$  nanocrystals to  $\text{Er}^{3+}$ ,” *Applied Physics Letters*, vol. 71, no. 9, pp. 1198–1200, 1 September 1997.
- [20] A. Hryciw, C. Blois, A. Meldrum, T. Clement, R. DeCorby, and Q. Li, “Photoluminescence from  $\text{Er}$ -doped silicon oxide microcavities,” *Optical Materials*, vol. 28, no. 6-7, pp. 873–878, May 2006.
- [21] J. Wang, X. F. Wang, Q. Li, A. Hryciw, and A. Meldrum, “The microstructure of  $\text{SiO}$  thin films: from nanoclusters to nanocrystals,” *Philosophical Magazine*, pp. 1–17, August 2006.
- [22] T. Shimizu-Iwayama, Y. Terao, A. Kamiya, M. Takeda, S. Nakao, and K. Saitoh, “Visible photoluminescence from silicon nanocrystals formed in silicon dioxide by ion implantation and thermal processing,” *Thin Solid Films*, vol. 276, no. 1-2, pp. 104–107, 15 April 1996.

- [23] R. Wehrspohn, J.-N. Chazalviel, F. Ozanam, and I. Solomon, "Spatial versus quantum confinement in porous amorphous silicon nanostructures," *The European Physical Journal B*, vol. 8, pp. 179–193, 1999.
- [24] C. Delerue, G. Allan, and M. Lannoo, "Theoretical aspects of the luminescence of porous silicon," *Physical Review B*, vol. 48, no. 15, pp. 11 024–11 036, March 1993.
- [25] M. Fujii, K. Imakita, K. Watanabe, and S. Hayashi, "Coexistence of two different energy transfer processes in  $SiO_2$  films containing  $Si$  nanocrystals and  $Er$ ," *Journal of Applied Physics*, vol. 95, no. 1, pp. 272–280, 1 January 2004.
- [26] S. Roberts and G. Parker, "Strong room temperature photoluminescence from erbium-doped silicon monoxide," *Electronics Letters*, vol. 31, pp. 1499–1500, August 1995.
- [27] A. J. Kenyon, P. F. Trwoga, M. Federighi, and C. W. Pitt, "Optical properties of PECVD erbium-doped silicon-rich silica: Evidence for energy transfer between silicon microclusters and erbium ions," *Journal of Physics. Condensed Matter*, vol. 6, no. 21, pp. L319–L324, 1994.
- [28] V. Y. Timoshenko, M. G. Lisachenko, O. A. Shalygina, B. V. Kamenev, D. M. Zhigunov, S. A. Teterukov, P. K. Kashkarov, J. Heitmann, M. Schmidt, and M. Zacharias, "Comparative study of photoluminescence of undoped and erbium-doped size-controlled nanocrystalline  $Si/SiO_2$  multilayered structures," *Journal of Applied Physics*, vol. 96, pp. 2254–2260, August 2004.
- [29] N.-M. Park, T.-Y. Kim, S. H. Kim, G. Y. Sung, B.-H. Kim, S.-J. Park, K. S. Cho, J. H. Shin, J.-K. Lee, and M. Nastasi, "Luminescence of erbium-doped amorphous silicon quantum dots," *Proceedings of the SPIE*, vol. 5361, pp. 60–65, June 2004.



- [30] M. Fujii, M. Yoshida, S. Hayashi, and K. Yamamoto, "Photoluminescence from  $SiO_2$  films containing  $Si$  nanocrystals and  $Er$ : Effects of nanocrystalline size on photoluminescence efficiency of  $Er^{3+}$ ," *Journal of Applied Physics*, vol. 84, no. 8, pp. 4525–4531, 15 October 1998.
- [31] J. Nishii, C. Se-Weon, H. Hosono, T. Taguchi, N. Nakane, H. Samata, Y. Oshitani, and M. Saito, "UV-induced excess loss of  $Er$ - and  $Si$ -nanocrystal co-doped silica waveguide for optical amplifier," *31st European Conference on Optical Communication*, vol. 4, pp. 941–942, September 2005.
- [32] N. Daldosso, D. Navarro-Urrios, M. Melchiorri, , L. Pavesi, F. Gourbilleau, M. Carrada, R. Rizk, C. Garcia, P. Pellegrino, B. Garrido, and L. Cagnolato, "Absorption cross section and signal enhancement in  $Er$ -doped  $Si$  nanocluster rib-loaded waveguides," *Applied Physics Letters*, vol. 86, p. 261103, June 2005.
- [33] W. Spitzer and H. Fan, "Infrared absorption in (n)-type silicon," *Physical Review*, vol. 108, no. 2, pp. 873–878, 15 October 1957.
- [34] S. Roberts and G. Parker, "Photoluminescence excitation and de-excitation mechanism of erbium doped silicon monoxide," *Electronics Letters*, vol. 32, no. 6, pp. 589–591, 14 March 1996.
- [35] S. W. Roberts, G. J. Parker, and M. Hempstead, "The photoluminescence of erbium-doped silicon monoxide," *Optical Materials*, vol. 6, no. 1-2, pp. 99–102, July 1996.
- [36] J. C. Manifacier, J. Gasiot, and J. P. Fillard, "A simple method for the determination of the optical constants  $n$ ,  $k$  and the thickness of a weakly absorbing thin film," *Journal of Physics E: Scientific Instruments*, vol. 9, no. 11, pp. 1002–1004, 1976.

- [37] R. Swanepoel, "Determination of the thickness and optical constants of amorphous silicon," *Journal of Physics E: Scientific Instruments*, vol. 16, pp. 1214–1222, 1983.
- [38] R. Swanepoel, "Determination of surface roughness and optical constants of inhomogeneous amorphous silicon films," *Journal of Physics E: Scientific Instruments*, vol. 17, pp. 896–903, 1984.
- [39] W. Stutius and W. Streifer, "Silicon nitride films on silicon for optical waveguides," *Applied Optics*, vol. 16, no. 12, pp. 3218–3222, Dec 1977.
- [40] R. Emmons, B. Kurdi, and D. Hall, "Buried-oxide silicon-on-insulator structures i: Optical waveguide characteristics," *IEEE Journal of Quantum Electronics*, vol. 28, no. 1, pp. 157–163, Jan 1992.
- [41] D. Bulla, W.-T. Li, C. Charles, R. Boswell, A. Ankiewicz, and J. Love, "Low-loss silica-based optical film waveguides deposited by helicon-activated reactive evaporation," *Journal of Lightwave Technology*, vol. 23, no. 3, pp. 1302–1307, Mar 2005.
- [42] C. Pollock, *Fundamentals of Optoelectronics*. Richard D. Irwin, 1995.
- [43] K. Chiang, "Review of numerical and approximate methods for the modal analysis of general optical dielectric waveguides," *Optical and Quantum Electronics*, vol. 26, pp. S113–S134, 1994.
- [44] G. Lifante, *Integrated Photonics: Fundamentals*. John Wiley and Sons, 2003.
- [45] H. G. Technologies. (2006, Aug.) Sol-gel hybrids. [Online]. Available: <http://www.hybridglass.com/products.html>
- [46] J. B. Ramirez-Malo, E. Marquez, C. Corrales, P. Villares, and R. Jimenez-Garay, "Optical characterization of  $As_2S_3$  and  $As_2Se_3$  semi-conducting glass films of non-uniform thickness from transmission mea-

- surements,” *Materials Science and Engineering B*, vol. 25, pp. 53–59, 1994.
- [47] G. Haas and C. Salzberg, “Optical properties of silicon monoxide in the wavelength region from 0.24 to 14.0 microns,” *Journal of the Optical Society of America*, vol. 44, no. 3, pp. 181–187, March 1954.
- [48] N. Ponnampalam, R. DeCorby, H. Nguyen, P. Dwivedi, C. Haugen, J. McMullin, and S. Kasap, “Small core rib waveguides with embedded gratings in  $As_2Se_3$  glass,” *Optics Express*, vol. 12, no. 25, pp. 6270–6277, December 2004.
- [49] G. Tittelbach, B. Richter, and W. Karthe, “Comparison of three transmission methods for integrated optical waveguide propagation loss measurement,” *Pure and Applied Optics*, vol. 2, no. 6, pp. 683–700, 1993.
- [50] L. S. Yu, Q. Z. Liu, S. A. Pappert, P. K. L. Yu, and S. S. Lau, “Laser spectral linewidth dependence on waveguide loss measurements using the Fabry-Perot method,” *Applied Physics Letters*, vol. 64, no. 5, pp. 536–538, 31 January 1993.
- [51] Y. Okamura, S. Yoshinaka, and S. Yamamoto, “Measuring mode propagation losses of integrated optical waveguides: A simple method,” *Applied Optics*, vol. 22, no. 23, pp. 3892–3894, December 1983.
- [52] E. Lifshin, “Electron microprobe analysis,” in *Encyclopedia of Materials: Science and Technology*, K. H. J. B. et al., Ed. Elsevier Science Ltd., 2001, pp. 2563–2569.
- [53] H. Mertens, A. Polman, I. M. P. Aarts, W. M. M. Kessels, and M. C. M. van de Sanden, “Absence of the enhanced intra- $4f$  transition cross section at  $1.5 \mu\text{m}$  of  $Er^{3+}$  in  $Si$ -rich  $SiO_2$ ,” *Applied Physics Letters*, vol. 86, p. 241109, June 2005.

- [54] H.-S. Han, S.-Y. Seo, and J. H. Shin, "Optical gain at  $1.54 \mu\text{m}$  in erbium-doped silicon nanocluster sensitized waveguide," *Applied Physics Letters*, vol. 79, no. 27, pp. 4568–4570, 2001.
- [55] M. J. F. Digonnet, Ed., *Rare-Earth-Doped Fiber Lasers and Amplifiers*. Marcel Dekker, Inc., 1993.
- [56] A. Siegman, *Lasers*. University Science Books, 1986.
- [57] H.-S. Han, S.-Y. Seo, J. H. Shin, and D.-S. Kim, " $1.54 \mu\text{m}$   $\text{Er}^{3+}$  photoluminescent and waveguiding properties of erbium-doped silicon-rich silicon oxide," *Journal of Applied Physics*, vol. 88, no. 4, pp. 2160–2162, 2000.
- [58] Q. Wang, N. K. Dutta, and R. Ahrens, "Spectroscopic properties of  $\text{Er}$  doped silica glasses," *Journal of Applied Physics*, vol. 95, no. 8, pp. 4025–4028, 15 April 2004.
- [59] J. Shin, J. Lee, H. seung Han, J.-H. Jhe, J. S. Chang, S.-Y. Seo, H. Lee, and N. Park, " $\text{Si}$  nanocluster sensitization of  $\text{Er}$ -doped silica for optical amplet using top-pumping visible LEDs," *Journal of Selected Topics in Quantum Electronics*, vol. 12, no. 4, pp. 783–796, July/August 2006.
- [60] R. Quimby, W. Miniscalco, and B. Thompson, "Clustering in erbium-doped silica glass fibers using 980 nm excited-state absorption," *Journal of Applied Physics*, vol. 76, no. 8, pp. 4472–4478, 1994.

# Appendix A

## Standard Processes

### A.1 The Standard Cleaning Process

Before processes were applied to thin films or patterned structures, it was routine to apply a cleaning process to remove any debris or organic material. The process is commonly referred to as a piranha cleaning and is outlined in Table A.1.

Step number	Step description
1	Combine 1 part hydrogen peroxide with 2 parts sulfuric acid (always add the sulfuric acid first).
2	Place sample into the solution for 20 minutes immediately after combining the two chemicals
3	Remove the sample and dump-rinse it in de-ionized water
4	Dry the sample with a nitrogen gun or in a spin-rinse dryer

Table A.1: The steps of the standard cleaning process.

### A.2 The Standard Annealing Process

All of the SiO and Er:SiO thin films were sourced from the lab of Al Meldrum. An optimum annealing cycle was developed for these films to optimize photo-

luminescence [20]. The sequence of steps involved in the standard annealing process is shown in Table A.2.

Step number	Step description
1	Apply the standard cleaning process to the sample.
2	Load the sample into the furnace and fill the furnace with 5%:95% $H_2:N_2$ to a pressure of 2 psi.
3	Anneal the sample for 1 hour at $500^\circ C$ .
4	Remove the sample from the furnace and apply the standard cleaning process again.

Table A.2: The steps of the standard annealing process.

# Appendix B

## Matlab Programs

### B.1 Matlab Code for Swanepoel's Method

This section shows the code used to extract the index of refraction from thin film transmission spectra.

#### The Top Level Calling Function

```
%%%%%%%%%%%%%%%%%%%%%%%%%%%%%%%%%%%%%%%%%%%%%%%%%%%%%%%%%%%%%%%%%%%%%%%%%%%%%%  
%%%%%%%%%%%%%%%%%%%%%%%%%%%%%%%%%%%%%%%%%%%%%%%%%%%%%%%%%%%%%%%%%%%%%%%%%%%%%%  
function [nFit,n_raw,d,del_d] = Swanepoel_nonlinear_V6_CWV  
    (name_start,file_num,lowwave,highwave)  
  
%  
%This function is a (hopeful) improvement over the original  
code which was written  
%by T Clement about a year ago. This version  
of things modularises several portions  
%of the code from the original. This version  
also stops using the built in non-linear  
%equation solver provided by Matlab, and instead uses  
a functionalized Newton-Rhapson%method.
```

```

%
%Questions regarding this function should be
addressed to T Clement, (ph: 441 3880)
%
%Version 6 CWV (Current Working Version) uses
several starting guesses and
%increments and reports the index and thickness
for each combination.
format long;
warning('off');

%%%%%%%%%%%%%%%%%%%%%%%%%%%%%%%%%%%%%%%%%%%%%%%%%%%%%%%%%%%%%%%%%%%%%%%%Extracting Data%%%%%%%%%%%%%%%%%%%%%%%%%%%%%%%%%%%%%%%%%%%%%%%%%%%%%%%%%%%%%%%%%%%%%%%%

name1 = strcat(name_start,int2str(file_num)
, '.rpk'); %name of peak data file
[peak_data] = get_spectro_peak_data(name1);
%Extracting peak data
name2 = strcat(name_start,int2str(file_num)
, '.sp'); %name of transmission data file
[trans_data] = get_spectro_trans_data(name2);
%extracting transmission data
name3 = strcat(name_start,'s.sp'); %name of
substrate data file
[subs_data] = get_spectro_trans_data(name3);
%Extracting substrate transmission data

sub_ind_calc = 100./subs_data(:,2)+((100
./subs_data(:,2)).^2-1).^0.5;
%substrate index calculation
subs_ind = [subs_data(:,1) sub_ind_calc];

```



```

    %New matrix with wavelength in first column,
    substrate index in second
mat = interp_extrema(peak_data, subs_ind);
%interpolates points for the enveloped
curves of the windowed data
mat = window_peak_data(mat,lowwave,highwave);
%selects the peak data between the upper
    and lower prescribed limits

dims_mat = size(mat); %the size if interpolated matrix

%%%%%%%%%%%%%%%%%%%%%%%%%%%%%%%%%%%%%%%%%%%%%%%%%%%%%%%%%%%%%%%%%%%%%%%%Setting Search Start Parameters%%%%%%%%%%%%%%%%%%%%%%%%%%%%%%%%%%%%%%%%%%%%%%%%%%%%%%%%%%%%%%%%%%%%%%%%

guess_start = [0:2.5:70];
increment = [0.5 0.1];
len_guess_start = length(guess_start);
len_increment = length(increment);

%This section of code determines a value for the index of
refraction (and thickness variation) for multiple
different starting guess values. the%values de-evolved
will depend on these starting guesses, because the
%non-linear eqn solver does not always iterate to the same
point. An%intelligent decision of which value to use
for the index should be made.
%
number = 0;
for j = 1:len_guess_start
    for k = 1:len_increment
        del_d_guess = guess_start(j);

```

```

inc = increment(k);
index = (j-1)*len_increment + k;
for i = 1:dims_mat(1)
    number2 = 0;
    n1(index,i) =7;
    del_d(index,i) = 200;
    while ((~((n1(index,i)<5)&(n1(index,i)>1.4))
    | ~(del_d(index,i) <100)) & del_d_guess < 85)
        number = number+1;
        number2 = number2+1;
        %fprintf('%d\n   %d\n',number,number2);
        del_d_guess = del_d_guess+inc;
        [n1(index,i), del_d(index,i),iter(index,i)]
        =NR_eqn_solver(2.8,mat(i,4),del_d_guess,
        mat(i,2),mat(i,3),mat(i,1)); % a first
        estimate for the index of refraction, and
        thickness non-homogeneity
        dummy(i,j,k) = n1(index,i);
    end
end
mat_combs(index,1) = guess_start(j);
mat_combs(index,2) = increment(k);
mat_combs(index,3:(3+dims_mat(1)-1)) = n1(index,:);
end
end
del_d_reshape = reshape(del_d,1,prod(size(del_d)));
del_d = value_decision(abs(del_d_reshape'),5);
fprintf('\n\nnumber of cycles was %d \n',number);

```

%At this point, we've extracted a best fit del\_d

parameter and could go back and plug it in and redo the index find with simpler equations

```
foutput = fopen('SNL_v4_op1','w');
%count = fprintf(foutput,'%6.5f',n1);

%FILTERING n1 for NAN values
n1_filter_mean = mean(n1');
row_inds = find(n1_filter_mean<1E10);
n1 = n1(row_inds,:);
%End n1 filtering

n1_copy = n1;

[n1] = value_decision(n1,0.0002);

n1_tot = [n1_copy;n1];

lam_n1 = [mat(:,1),n1']; %used for concatenating large amounts
of data points from multiple files

dims_n1_tot = size(n1_tot);
str1 = '';
str2 = '    %012.7f';
for k = 1:dims_n1_tot(2)
    str1 = strcat(str1,str2);
end
str1 = strcat(str1,'\n');
count = fprintf(foutput,str1,mat(:,1),n1_tot');
```

```

for j = 1:(dims_mat(1)-2)
    d1(:,j) = mat(j,1)*mat(j+2,1)./(2*(mat(j,1)*n1(:,j+2)
        -mat(j+2,1)*n1(:,j)));
    %first estimate for thickness
end

[n2,d2_mean,d2_std,m_vec] = n_d_interference_update_v3b
    (n1,d1,mat(:,1),mat(:,2));
[lambda,n_vec] = Wemple_DiDomenico_fit(n2,mat(:,1)',lowwave);
figure(2);
plot(lambda,n_vec);
hold on;
plot(mat(:,1),n1,'m*');
plot(mat(:,1),(n2),'ro');
legend('fit to n2','experimental n1','experimental n2');
grid on;

n_1550 = n_vec(1550-lowwave)
Tauc_plot_v2(trans_data(:,2),trans_data(:,1),d2_mean,
    max(trans_data(:,2)))
warning('on');

fclose(foutput);
nFit = [lambda; n_vec]';
n_raw = n2;
d = d2_mean;

```

```

%%%%%%%%%%%%%%%%%%%%%%%%%%%%%%%%%%%%%%%%%%%%%%%%%%%%%%%%%%%%%%%%%%%%%%%%
%%%%%%%%%%%%%%%%%%%%%%%%%%%%%%%%%%%%%%%%%%%%%%%%%%%%%%%%%%%%%%%%%%%%%%%%

```

## Embedded Functions Called

```
%%%%%%%%%%%%%%%%%%%%%%%%%%%%%%%%%%%%%%%%%%%%%%%%%%%%%%%%%%%%%%%%%%%%%%%%
%%%%%%%%%%%%%%%%%%%%%%%%%%%%%%%%%%%%%%%%%%%%%%%%%%%%%%%%%%%%%%%%%%%%%%%%
function [peak_data_f] = get_spectro_peak_data(name)
%
%This function takes a general string identifier
, name, which is the name of the ***peak data file***
in question and opens and removes the desirable
information.%
%the variable returned, peak_data_f, is a n rows by 2
column matrix containing wavelengths in the first column
and corresponding transmission percentages in the second.
format long;

fid = fopen(name,'r');
for j = 1:10 %scanning useless character info at start of file
    fgetl(fid);
end
[A,count] = fscanf(fid,'%s'); %scanning rest of
data file to determine # of elements in file
frewind(fid); %sends pointer back
to start of data file
for j = 1:10 %again eating up
useless character info
    fgetl(fid);
end
for j = 1:count/4 %with the knowledge of # of
elements in file correct assignment can begin
    peak_data(3*(j-1)+1) = fscanf(fid,'%f',1); % first three
elements are numerical
```

```

    peak_data(3*(j-1)+2) = fscanf(fid,'%f',1);
    peak_data(3*(j-1)+3) = fscanf(fid,'%f',1);
    junk = fscanf(fid,'%s',1);           % fourth element is
    an unimportant string
end
peak_data_r = reshape(peak_data,3,count/4);
%reshaping linear vector into a three row matrix
peak_data_r = peak_data_r';
peak_data_r = peak_data_r(:,2:3);
%selecting desired numerical components to keep
peak_data_r = sortrows(peak_data_r);
%sorts entire rows in ascending order on the basis of the
    value of the first non-singleton column of the matrix
peak_data_f = flipud(peak_data_r);
    %data now in descending order
frewind(fid);
fclose(fid);

%%%%%%%%%%%%%%%%%%%%%%%%%%%%%%%%%%%%%%%%%%%%%%%%%%%%%%%%%%%%%%%%%%%%%%%%%%%%%%
%%%%%%%%%%%%%%%%%%%%%%%%%%%%%%%%%%%%%%%%%%%%%%%%%%%%%%%%%%%%%%%%%%%%%%%%%%%%%%
function [trans_data_f] = get_spectro_trans_data(name)
%
%Much like get_spectro_peak_data, get_spectro_trans_data is
    designed to take the name of%a spectrophotometer
    transmission file and return the useful data
%
%trans_data_f is an n by 2 matrix containing wavelengths
    (in nm) in the first column, and
%transmission percentages in the second
format long;

```

```

fid = fopen(name,'r');
for j = 1:86
%scanning useless character info at start of file
    fgetl(fid);
end
trans_data = fscanf(fid,'%f');
trans_data_f = reshape(trans_data,2,length(trans_data)/2)';
frewind(fid);
fclose(fid);

%%%%%%%%%%%%%%%%%%%%%%%%%%%%%%%%%%%%%%%%%%%%%%%%%%%%%%%%%%%%%%%%%%%%%%%%%%%%%%
%%%%%%%%%%%%%%%%%%%%%%%%%%%%%%%%%%%%%%%%%%%%%%%%%%%%%%%%%%%%%%%%%%%%%%%%%%%%%%
function mat = interp_extrema(data,subs_ind)
format long;

fcol = data(:,1);
%creating new vectors for new matrix
scol = data(:,2);
origmaxmin = scol;
%for determining if starting with min or max
tcol = zeros(length(fcol),1);
scoln = zeros(length(fcol),2);
mat = zeros(length(fcol),4);
mtp = repmat(eye(2),ceil(length(scol)/2));
mtp = mtp(1:length(scol),1);
%vector of the form [1 0 1 0 1 0 1 ...]
mtp = bitcmp(mtp,1);
%vector of the form [0 1 0 1 0 1 0 ...]
scoln(:,2) = scol.*mtp;

```

```

%splitting peaks up into max peaks and min peak columns
scoln(:,1) = scol.*mtp;
%since they are currently all in scol
mat = [fcol,scoln,tcol];
[p,s,mu] = polyfit([mat(1,1),mat(3,1),mat(5,1)], [mat(1,3),
mat(3,3),mat(5,3)],2);
%beginning interpolations to determine
mat(2,3)= polyval(p, (mat(2,1)-mu(1))/mu(2));
% values between empirical values
[p,s,mu] = polyfit([mat(2,1),mat(4,1),mat(6,1)], [mat(2,2),
mat(4,2),mat(6,2)],2);
mat(3,2)= polyval(p, (mat(3,1)-mu(1))/mu(2));
k = 3;
dims = size(mat);
for j = 4:dims(1)
    k= k+1;
    if k+1<=length(mat)
        [p,s,mu] = polyfit([mat(k-3,1),mat(k-1,1),mat(k+1,1)],
            [mat(k-3,3),mat(k-1,3),mat(k+1,3)],2);
        mat(k,3)= polyval(p, (mat(k,1)-mu(1))/mu(2));
        %the automated interpolation process (third column)
    end
    k = k+1;
    if k+1<=length(mat)
        [p,s,mu] = polyfit([mat(k-3,1),mat(k-1,1),mat(k+1,1)],
            [mat(k-3,2),mat(k-1,2),mat(k+1,2)],2);
        mat(k,2)= polyval(p, (mat(k,1)-mu(1))/mu(2));
        %the automated interpolation process (second column)
    end
end
end

```



```

dims = size(mat);
for j =1:dims(1)
    k = max(find(subs_ind(:,1) >= mat(j,1)));
    %Finding the corresponding substrate index for this place
    mat(j,4) = interp1([subs_ind(k,1);
    subs_ind(k+1,1)], [subs_ind(k,2); subs_ind(k+1,2)], mat(j,1));
    %interpolates for precise index value
end
mat = mat(2:dims(1)-1,:);
*****%%Truncating data to get rid of zeros in matrix
origmaxmin = origmaxmin(2:dims(1)-1,:);
if (mat(1,2)-mat(1,3))<0
%Want to make sure that maximums are in column
2 and minimums are
    dumb = mat(:,2);
    %in column 3; if they are not, they are exchanged.
    mat(:,2) = mat(:,3);
    mat(:,3) = dumb;
end
    mat(:,2:3) = mat(:,2:3)/100;
    %Changing percentage transmission into normalized
    transmission (0->1)

%%%%%%%%%%%%%%%%%%%%%%%%%%%%%%%%%%%%%%%%%%%%%%%%%%%%%%%%%%%%%%%%%%%%%%%%%%%%%%
%%%%%%%%%%%%%%%%%%%%%%%%%%%%%%%%%%%%%%%%%%%%%%%%%%%%%%%%%%%%%%%%%%%%%%%%%%%%%%
function [mat_f] = window_peak_data(mat,low,high)
%
%This function takes user specified high and low wavelengths
%and windows the data set within these extremities
%
```

```

format long;

ind = find(mat(:,1)>low & mat(:,1)<high);
%finding data between low and high cutoff wavelengths
mat_f = mat(ind(1):ind(length(ind)),:);
%selecting data between low and high cutoff wavelengths

%%%%%%%%%%%%%%%%%%%%%%%%%%%%%%%%%%%%%%%%%%%%%%%%%%%%%%%%%%%%%%%%%%%%%%%%
%%%%%%%%%%%%%%%%%%%%%%%%%%%%%%%%%%%%%%%%%%%%%%%%%%%%%%%%%%%%%%%%%%%%%%%%
function [lambda,n_vec] = Wemple_DiDomenico_fit(n,lam,low)
%
%This function fits the dispersion in the index of
%refraction to the Wemple-DiDomenico relation. This
%relation has two free parameters
%

%n = n(1:3);
%lam = lam(1:3);
c=2.997e8; %m/s
lam_m = lam/1e9'; %in metres
h = 6.626e-34; %J*s

E = h*c./lam_m; % Joules

X = E.^2;
Y = 1./(n.^2-1);

figure(1);
clf;
plot(X/(1.6e-19)^2,Y,'mo');

```

```

p = polyfit(X,Y,1);

E0_u = sqrt(-p(2)/p(1))/1.6e-19
Ed_u = 1/sqrt(-p(1)*p(2))/1.6e-19

E0 = sqrt(-p(2)/p(1));
Ed = 1/sqrt(-p(1)*p(2));

lambda = [low:2000];
lambda_m =lambda/1E9;
E = h*c./lambda_m; % Joules
n_vec = sqrt(1+(E0*Ed)./(E0^2-E.^2));

figure(2);
clf;
plot(lambda,n_vec);

%%%%%%%%%%%%%%%%%%%%%%%%%%%%%%%%%%%%%%%%%%%%%%%%%%%%%%%%%%%%%%%%%%%%%%%%
%%%%%%%%%%%%%%%%%%%%%%%%%%%%%%%%%%%%%%%%%%%%%%%%%%%%%%%%%%%%%%%%%%%%%%%%
function [n1_output]= value_decision(n1_input,threshold)
%
%A different method of trying to determine the
%appropriate index of refraction iterated to using
%the transcendental solver.
%

s_n1 = size(n1_input);

%n1_input is a matrix with columns representing

```

```

%different wavelengths. The rows represent different
%initial guesses, and the entry is the index of
%refraction iterated to.

for i = 1:s_n1(2)

    n_v_present = n1_input(:,i);
    inds_uninf = find(n_v_present < 1e50);
    %This finds values less than NaN or Inf
    n_v_present = n_v_present(inds_uninf);
    if isempty(n_v_present) == 1
        fprintf('values did not converge');
        n1_output = [];
        return
    end
    l_n_v_present = length(n_v_present);
    n_v_present_s = (sort(n_v_present));
    %now the values are sorted. Values of a specific
    %wavelength are still in columns.

    n_v_present_s_diff = diff(n_v_present_s);
    %This takes the difference between successive values
    %in the matrix n1_input_sorted.
    vals_to_ave = [];
    inds = (find(n_v_present_s_diff > threshold))';
    %finds where the differences between successive index
    %values is larger than value 'threshold'.

    l_inds = length(inds);
    bps = [0 inds l_n_v_present]; % breaking values

```

```

%Shows starts and ends of ranges of points with
%similar index values.
%
if l_inds==0
    n1_output(i) = mean(n_v_present_s);
    %if there are no breakpoints, all points are
    %assumed to be of approximately equal value
end
if l_inds>=1
    d_bps = diff(bps);
    %for systems with breakpoints (significant
    %changes in index), this provides the number
    %of similar values. The values with the
    %largest number of similar values is ASSUMED
    %to be the correct values
    inds_d_bps = find(d_bps == max(d_bps));
    %finds the values which are represented the most
    for n = 1:length(inds_d_bps)
        vals_to_ave = [vals_to_ave
            (bps(inds_d_bps(n))+1):bps(inds_d_bps(n)+1)];
    end
    n1_output(i) = mean(n_v_present_s(vals_to_ave));
end
end

```

```

%%%%%%%%%%%%%%%%%%%%%%%%%%%%%%%%%%%%%%%%%%%%%%%%%%%%%%%%%%%%%%%%%%%%%%%%
%%%%%%%%%%%%%%%%%%%%%%%%%%%%%%%%%%%%%%%%%%%%%%%%%%%%%%%%%%%%%%%%%%%%%%%%
function [n2,d2_mean,d2_std,m_vec] =
n_d_interference_update_v3b(n1,d1,lam,T)
%

```

```

%By calculating values for index and thickness, and
%knowing where in the wavelength spectrum these values
%are taken at, values for the interference fringe
%order, m, can be calculated.  These fringe values
%should be either integers (for interference maxima)
%or half-integers (for interference minima)

Tmax = max(T);
Tcutoff = 0.90*Tmax; %percentage of max trans for transparency
inds = find(T<Tcutoff);

%Previous lines attempt to determine the most suitable
%data points to sample for use in determining thickness
%.

if isempty(inds) == 1
    last_transparent_point = length(T);
else
    inds_min = min(inds);
    last_transparent_point = inds_min-1;
end

d = mean(d1(1:(last_transparent_point-2)));
m_first = 2.*n1.*d./lam';
m_first_update = round(m_first*2)/2;
subtraction_vec = 0.5*[0:(length(n1)-1)];
m_shift_for_choice = m_first_update-subtraction_vec;
m1 = value_decision(m_shift_for_choice',0.249);
%0.249 selected because it is slightly less than half of 0.5

```

```

m_vec = m1+0.5*[0:(last_transparent_point-1)];
lam_ll = lam(1:last_transparent_point);
n1_ll = n1(1:last_transparent_point);
n1_hl = n1((last_transparent_point+1):length(n1));
d2 = m_vec.*lam_ll'./(2.*n1_ll);
d2_mean = mean(d2(1:last_transparent_point));
%%%%%%%%this needs the same averaging as above
d2_std = std(d2(1:last_transparent_point));

n2_ll = m_vec.*lam_ll'./(2*d2_mean);
n2 = [n2_ll n1_hl];

```

```

%%%%%%%%%%%%%%%%%%%%%%%%%%%%%%%%%%%%%%%%%%%%%%%%%%%%%%%%%%%%%%%%%%%%%%%%
%%%%%%%%%%%%%%%%%%%%%%%%%%%%%%%%%%%%%%%%%%%%%%%%%%%%%%%%%%%%%%%%%%%%%%%%
function [] = Tauc_plot_v2(T_tauc,lam_tauc,d,T_max)
%
%This function generates a Tauc plot in order to
%try to uncover the bandgap of the material in
%question. alpha should be in (/cm).
%
%
T_norm = T_tauc./T_max;
alpha_tauc = -log(T_norm)/d*1e7;
c = 2.997e8 %m/s
v = c./lam_tauc*1e9;;
h = 6.626e-34/1.6e-19; %(eV)s

E = h*v;

```

```

y_axis = (alpha_tauc.*E).^0.5;

figure(4);
clf;

plot(E',y_axis,'ro');
grid on;
title('Tauc plot');

%%%%%%%%%%%%%%%%%%%%%%%%%%%%%%%%%%%%%%%%%%%%%%%%%%%%%%%%%%%%%%%%%%%%%%%%
%%%%%%%%%%%%%%%%%%%%%%%%%%%%%%%%%%%%%%%%%%%%%%%%%%%%%%%%%%%%%%%%%%%%%%%%
function [n,del_d,iter] = NR_eqn_solver(n,s,del_d,TMd,Tmd,lam)

format long
chg_n = 1;
chg_del_d = 2;
iter = 0;

while (abs(chg_n)>2E-3 & abs(chg_del_d) > 1)

f1 = (lam/(2*pi*n*del_d))*((16*n^2*s/((n+1)^3*(n+s^2)+(n-1)^3*
(n-s^2)))/(1-(2*(n^2-1)*(n^2-s^2)/((n+1)^3*(n+s^2)+
(n-1)^3*(n-s^2))))^2)^0.5)*atan((1+(2*(n^2-1)*(n^2-s^2)/
((n+1)^3*(n+s^2)+(n-1)^3*(n-s^2))))/(1-(2*(n^2-1)*
(n^2-s^2)/((n+1)^3*(n+s^2)+(n-1)^3*(n-s^2))))^2)^0.5
*tan(2*pi*n*del_d/lam)) - TMd;
f2 = (lam/(2*pi*n*del_d))*((16*n^2*s/((n+1)^3*
(n+s^2)+(n-1)^3*(n-s^2)))/(1-(2*(n^2-1)*(n^2-s^2)/
((n+1)^3*(n+s^2)+(n-1)^3*(n-s^2))))^2)^0.5)

```



$$\begin{aligned}
& * \operatorname{atan}\left(\frac{(1-(2*(n^2-1)*(n^2-s^2))/((n+1)^3*(n+s^2)+(n-1)^3*(n-s^2)))}{(1-(2*(n^2-1)*(n^2-s^2)/((n+1)^3*(n+s^2)+(n-1)^3*(n-s^2)))^2}\right)^{0.5} \\
& * \tan(2*\pi*n*\operatorname{del}_d/\operatorname{lam})) - Tmd;
\end{aligned}$$

$$\begin{aligned}
df1\_dn = & 8*\operatorname{lam}/\pi/\operatorname{del}_d*s/((n+1)^3*(n+s^2)+(n-1)^3*(n-s^2))/ \\
& (1-(2*n^2-2)^2*(n^2-s^2)^2/((n+1)^3*(n+s^2)+(n-1)^3*(n-s^2))^2)^{(1/2)} * \\
& \operatorname{atan}\left(\frac{(1+(2*n^2-2)*(n^2-s^2))/((n+1)^3*(n+s^2)+(n-1)^3*(n-s^2))}{(1-(2*n^2-2)^2*(n^2-s^2)^2/((n+1)^3*(n+s^2)+(n-1)^3*(n-s^2))^2}\right)^{(1/2)} * \\
& \tan(2*\pi*n*\operatorname{del}_d/\operatorname{lam})) - 8*\operatorname{lam}/\pi*n/\operatorname{del}_d*s/ \\
& ((n+1)^3*(n+s^2)+(n-1)^3*(n-s^2))^2/(1-(2*n^2-2)^2*(n^2-s^2)^2/((n+1)^3*(n+s^2)+(n-1)^3*(n-s^2))^2)^{(1/2)} * \\
& \operatorname{atan}\left(\frac{(1+(2*n^2-2)*(n^2-s^2))/((n+1)^3*(n+s^2)+(n-1)^3*(n-s^2))}{(1-(2*n^2-2)^2*(n^2-s^2)^2/((n+1)^3*(n+s^2)+(n-1)^3*(n-s^2))^2}\right)^{(1/2)} * \\
& \tan(2*\pi*n*\operatorname{del}_d/\operatorname{lam})) * (3*(n+1)^2*(n+s^2)+(n+1)^3+3*(n-1)^2*(n-s^2)+(n-1)^3) - 4*\operatorname{lam}/\pi * \\
& n/\operatorname{del}_d*s/((n+1)^3*(n+s^2)+(n-1)^3*(n-s^2))/ \\
& (1-(2*n^2-2)^2*(n^2-s^2)^2/((n+1)^3*(n+s^2)+(n-1)^3*(n-s^2))^2)^{(3/2)} * \operatorname{atan}\left(\frac{(1+(2*n^2-2)*(n^2-s^2))/((n+1)^3*(n+s^2)+(n-1)^3*(n-s^2))}{(1-(2*n^2-2)^2*(n^2-s^2)^2/((n+1)^3*(n+s^2)+(n-1)^3*(n-s^2))^2}\right)^{(1/2)} * \\
& \tan(2*\pi*n*\operatorname{del}_d/\operatorname{lam})) * (-8*(2*n^2-2)*(n^2-s^2)^2/((n+1)^3*(n+s^2)+(n-1)^3*(n-s^2))^2 * n - 4*(2*n^2-2)^2*(n^2-s^2)/((n+1)^3*(n+s^2)+(n-1)^3*(n-s^2))^2 * n + 2*(2*n^2-2)^2*(n^2-s^2)^2/((n+1)^3*(n+s^2)+(n-1)^3*(n-s^2))^3 * (3*(n+1)^2*(n+s^2)+(n+1)^3+3*(n-1)^2*(n-s^2)+
\end{aligned}$$

$$\begin{aligned}
& (n-1)^3)) + 8 * \text{lam} / \text{pi} * n / \text{del\_d} * s / ((n+1)^3 * (n+s^2) + \\
& (n-1)^3 * (n-s^2)) / (1 - (2*n^2-2)^2 * (n^2-s^2)^2 / \\
& ((n+1)^3 * (n+s^2) + (n-1)^3 * (n-s^2))^2)^{(1/2)} * \\
& ((4*n*(n^2-s^2) / ((n+1)^3 * (n+s^2) + (n-1)^3 * \\
& (n-s^2)) + 2 * (2*n^2-2) * n / ((n+1)^3 * (n+s^2) + (n-1)^3 \\
& * (n-s^2)) - (2*n^2-2) * (n^2-s^2) / ((n+1)^3 * (n+s^2) + \\
& (n-1)^3 * (n-s^2)))^2 * (3 * (n+1)^2 * (n+s^2) + (n+1)^3 + 3 * \\
& (n-1)^2 * (n-s^2) + (n-1)^3)) / (1 - (2*n^2-2)^2 * \\
& (n^2-s^2)^2 / ((n+1)^3 * (n+s^2) + (n-1)^3 * \\
& (n-s^2))^2)^{(1/2)} * \tan(2 * \text{pi} * n * \text{del\_d} / \text{lam}) - 1/2 * \\
& (1 + (2*n^2-2) * (n^2-s^2) / ((n+1)^3 * (n+s^2) + (n-1)^3 \\
& * (n-s^2))) / (1 - (2*n^2-2)^2 * (n^2-s^2)^2 / ((n+1)^3 * \\
& (n+s^2) + (n-1)^3 * (n-s^2))^2)^{(3/2)} * \\
& \tan(2 * \text{pi} * n * \text{del\_d} / \text{lam}) * (-8 * (2*n^2-2) * (n^2-s^2)^2 / \\
& ((n+1)^3 * (n+s^2) + (n-1)^3 * (n-s^2))^2 * n - 4 * (2*n^2-2)^2 \\
& * (n^2-s^2) / ((n+1)^3 * (n+s^2) + (n-1)^3 * (n-s^2))^2 * \\
& n + 2 * (2*n^2-2)^2 * (n^2-s^2)^2 / ((n+1)^3 * (n+s^2) + \\
& (n-1)^3 * (n-s^2))^3 * (3 * (n+1)^2 * (n+s^2) + (n+1)^3 + \\
& 3 * (n-1)^2 * (n-s^2) + (n-1)^3)) + 2 * (1 + (2*n^2-2) * \\
& (n^2-s^2) / ((n+1)^3 * (n+s^2) + (n-1)^3 * (n-s^2))) / \\
& (1 - (2*n^2-2)^2 * (n^2-s^2)^2 / ((n+1)^3 * (n+s^2) + \\
& (n-1)^3 * (n-s^2))^2)^{(1/2)} * (1 + \tan(2 * \text{pi} * n * \\
& \text{del\_d} / \text{lam})^2 * \text{pi} * \text{del\_d} / \text{lam}) / (1 + (1 + (2*n^2-2) * \\
& (n^2-s^2) / ((n+1)^3 * (n+s^2) + (n-1)^3 * (n-s^2)))^2 / \\
& (1 - (2*n^2-2)^2 * (n^2-s^2)^2 / ((n+1)^3 * (n+s^2) + \\
& (n-1)^3 * (n-s^2))^2) * \tan(2 * \text{pi} * n * \text{del\_d} / \text{lam})^2); \\
\text{df2\_dn} = & 8 * \text{lam} / \text{pi} / \text{del\_d} * s / ((n+1)^3 * (n+s^2) + \\
& (n-1)^3 * (n-s^2)) / (1 - (2*n^2-2)^2 * (n^2-s^2)^2 / \\
& ((n+1)^3 * (n+s^2) + (n-1)^3 * (n-s^2))^2)^{(1/2)} * \\
& \text{atan}((1 - (2*n^2-2) * (n^2-s^2) / ((n+1)^3 * (n+s^2) +
\end{aligned}$$

$$\begin{aligned}
& ((n-1)^{3(n-s^2)}) / (1 - (2n^2-2)^2 (n^2-s^2)^2 / \\
& ((n+1)^{3(n+s^2)} + (n-1)^{3(n-s^2)})^2)^{1/2} * \\
& \tan(2\pi n \text{del}_d / \text{lam}) - 8\text{lam} / \pi n / \text{del}_d * s / \\
& ((n+1)^{3(n+s^2)} + (n-1)^{3(n-s^2)})^2 / \\
& (1 - (2n^2-2)^2 (n^2-s^2)^2 / ((n+1)^{3(n+s^2)} + \\
& (n-1)^{3(n-s^2)})^2)^{1/2} * \text{atan}((1 - (2n^2-2) * \\
& (n^2-s^2) / ((n+1)^{3(n+s^2)} + (n-1)^{3(n-s^2)})) / \\
& (1 - (2n^2-2)^2 (n^2-s^2)^2 / ((n+1)^{3(n+s^2)} + \\
& (n-1)^{3(n-s^2)})^2)^{1/2} * \tan(2\pi n \text{del}_d / \text{lam})) * \\
& (3(n+1)^2 (n+s^2) + (n+1)^3 + 3(n-1)^2 (n-s^2) + \\
& (n-1)^3) - 4\text{lam} / \pi n / \text{del}_d * s / ((n+1)^{3(n+s^2)} + \\
& (n-1)^{3(n-s^2)}) / (1 - (2n^2-2)^2 (n^2-s^2)^2 / \\
& ((n+1)^{3(n+s^2)} + (n-1)^{3(n-s^2)})^2)^{3/2} * \\
& \text{atan}((1 - (2n^2-2) * (n^2-s^2) / ((n+1)^{3(n+s^2)} + \\
& (n-1)^{3(n-s^2)})) / (1 - (2n^2-2)^2 (n^2-s^2)^2 / \\
& ((n+1)^{3(n+s^2)} + (n-1)^{3(n-s^2)})^2)^{1/2} * \\
& \tan(2\pi n \text{del}_d / \text{lam})) * (-8 * (2n^2-2) * \\
& (n^2-s^2)^2 / ((n+1)^{3(n+s^2)} + (n-1)^{3(n-s^2)})^2 \\
& * n - 4 * (2n^2-2)^2 (n^2-s^2) / ((n+1)^{3(n+s^2)} + \\
& (n-1)^{3(n-s^2)})^2 * n + 2 * (2n^2-2)^2 * \\
& (n^2-s^2)^2 / ((n+1)^{3(n+s^2)} + (n-1)^{3 * \\
& (n-s^2)})^3 * (3 * (n+1)^2 * (n+s^2) + (n+1)^3 + 3 * \\
& (n-1)^2 * (n-s^2) + (n-1)^3)) + 8\text{lam} / \pi n / \text{del}_d * \\
& s / ((n+1)^{3(n+s^2)} + (n-1)^{3(n-s^2)}) / (1 - (2 * \\
& n^2-2)^2 (n^2-s^2)^2 / ((n+1)^{3(n+s^2)} + (n-1)^3 \\
& * (n-s^2)})^2)^{1/2} * ((-4 * n * (n^2-s^2) / ((n+1)^3 * \\
& (n+s^2) + (n-1)^3 * (n-s^2)) - 2 * (2n^2-2) * n / ((n+1)^3 * \\
& (n+s^2) + (n-1)^3 * (n-s^2)) + (2n^2-2) * (n^2-s^2) / \\
& ((n+1)^3 * (n+s^2) + (n-1)^3 * (n-s^2)))^2 * (3 * (n+1)^2 * \\
& (n+s^2) + (n+1)^3 + 3 * (n-1)^2 * (n-s^2) + (n-1)^3) /
\end{aligned}$$

$$\begin{aligned}
& (1-(2*n^2-2)^2*(n^2-s^2)^2/((n+1)^3*(n+s^2)+ \\
& (n-1)^3*(n-s^2))^2)^{(1/2)}*\tan(2*pi*n*del\_d/lam) \\
& -1/2*(1-(2*n^2-2)*(n^2-s^2)/((n+1)^3*(n+s^2)+ \\
& (n-1)^3*(n-s^2)))/(1-(2*n^2-2)^2*(n^2-s^2)^2/ \\
& ((n+1)^3*(n+s^2)+(n-1)^3*(n-s^2))^2)^{(3/2)}* \\
& \tan(2*pi*n*del\_d/lam)*(-8*(2*n^2-2)*(n^2-s^2)^2 \\
& /((n+1)^3*(n+s^2)+(n-1)^3*(n-s^2))^2*n-4* \\
& (2*n^2-2)^2*(n^2-s^2)/((n+1)^3*(n+s^2)+(n-1)^3 \\
& *(n-s^2))^2*n+2*(2*n^2-2)^2*(n^2-s^2)^2/((n+1)^3 \\
& *(n+s^2)+(n-1)^3*(n-s^2))^3*(3*(n+1)^2*(n+s^2)+ \\
& (n+1)^3+3*(n-1)^2*(n-s^2)+(n-1)^3))+2*(1-(2*n^2-2) \\
& *(n^2-s^2)/((n+1)^3*(n+s^2)+(n-1)^3*(n-s^2)))/ \\
& (1-(2*n^2-2)^2*(n^2-s^2)^2/((n+1)^3*(n+s^2)+ \\
& (n-1)^3*(n-s^2))^2)^{(1/2)}*(1+\tan(2*pi*n*del\_d/ \\
& lam)^2)*pi*del\_d/lam)/(1+(1-(2*n^2-2)*(n^2-s^2)/ \\
& ((n+1)^3*(n+s^2)+(n-1)^3*(n-s^2))^2/ \\
& (1-(2*n^2-2)^2*(n^2-s^2)^2/((n+1)^3*(n+s^2)+ \\
& (n-1)^3*(n-s^2))^2)*\tan(2*pi*n*del\_d/lam)^2);
\end{aligned}$$

$$\begin{aligned}
df1\_ddel\_d = & -8*lam/pi*n/del\_d^2*s/((n+1)^3* \\
& (n+s^2)+(n-1)^3*(n-s^2))/(1-(2*n^2-2)^2* \\
& (n^2-s^2)^2/((n+1)^3*(n+s^2)+(n-1)^3* \\
& (n-s^2))^2)^{(1/2)}*atan((1+(2*n^2-2)* \\
& (n^2-s^2)/((n+1)^3*(n+s^2)+(n-1)^3* \\
& (n-s^2)))/(1-(2*n^2-2)^2*(n^2-s^2)^2/ \\
& ((n+1)^3*(n+s^2)+(n-1)^3*(n-s^2))^2)^{(1/2)}* \\
& \tan(2*pi*n*del\_d/lam))+16*n^2/del\_d*s/ \\
& ((n+1)^3*(n+s^2)+(n-1)^3*(n-s^2))/ \\
& (1-(2*n^2-2)^2*(n^2-s^2)^2/((n+1)^3* \\
& (n+s^2)+(n-1)^3*(n-s^2))^2)*(1+(2*n^2-2)*
\end{aligned}$$

```

(n^2-s^2)/((n+1)^3*(n+s^2)+(n-1)^3*
(n-s^2))* (1+tan(2*pi*n*del_d/lam)^2)/
(1+(1+(2*n^2-2)*(n^2-s^2)/((n+1)^3*
(n+s^2)+(n-1)^3*(n-s^2)))^2/(1-(2*n^2-2)^2*
(n^2-s^2)^2/((n+1)^3*(n+s^2)+(n-1)^3*
(n-s^2))^2)*tan(2*pi*n*del_d/lam)^2);
df2_ddel_d = -8*lam/pi*n/del_d^2*s/((n+1)^3*
(n+s^2)+(n-1)^3*(n-s^2))/(1-(2*n^2-2)^2*
(n^2-s^2)^2/((n+1)^3*(n+s^2)+(n-1)^3*
(n-s^2))^2)^(1/2)*atan((1-(2*n^2-2)*
(n^2-s^2)/((n+1)^3*(n+s^2)+(n-1)^3*
(n-s^2)))/(1-(2*n^2-2)^2*(n^2-s^2)^2/
((n+1)^3*(n+s^2)+(n-1)^3*(n-s^2))^2)^(1/2)*
tan(2*pi*n*del_d/lam))+16*n^2/del_d*s/
((n+1)^3*(n+s^2)+(n-1)^3*(n-s^2))/
(1-(2*n^2-2)^2*(n^2-s^2)^2/((n+1)^3*
(n+s^2)+(n-1)^3*(n-s^2))^2)*(1-(2*n^2-2)*
(n^2-s^2)/((n+1)^3*(n+s^2)+(n-1)^3*
(n-s^2)))*(1+tan(2*pi*n*del_d/lam)^2)/
(1+(1-(2*n^2-2)*(n^2-s^2)/((n+1)^3*
(n+s^2)+(n-1)^3*(n-s^2)))^2/(1-(2*n^2-2)^2*
(n^2-s^2)^2/((n+1)^3*(n+s^2)+(n-1)^3*
(n-s^2))^2)*tan(2*pi*n*del_d/lam)^2);

chg_n = (-f2 + f1*df2_ddel_d/df1_ddel_d)/
(df2_dn-df1_dn*df2_ddel_d/df1_ddel_d);
chg_del_d = (-f1+f1*df2_ddel_d)/df1_ddel_d;

n = n+chg_n;
del_d = del_d + chg_del_d;

```

```

iter = iter+1;
fprintf('%d \n',iter);
end

```

```

%%%%%%%%%%%%%%%%%%%%%%%%%%%%%%%%%%%%%%%%%%%%%%%%%%%%%%%%%%%%%%%%%%%%%%%%
%%%%%%%%%%%%%%%%%%%%%%%%%%%%%%%%%%%%%%%%%%%%%%%%%%%%%%%%%%%%%%%%%%%%%%%%

```

## B.2 Matlab Code for the Three-Layer Slab Model

This function provides the transverse propagation constants (*kappa* values) of allowed TE and TM modes in a specified structure. The structure can be asymmetric, and a schematic of the structure is shown in Fig. 2.2.

### The Top Level Calling Function

```

%%%%%%%%%%%%%%%%%%%%%%%%%%%%%%%%%%%%%%%%%%%%%%%%%%%%%%%%%%%%%%%%%%%%%%%%
%%%%%%%%%%%%%%%%%%%%%%%%%%%%%%%%%%%%%%%%%%%%%%%%%%%%%%%%%%%%%%%%%%%%%%%%

```

```

function mode_solver_test(k0,t,n1,n2,n3)

[search_zones,kap_min,kap_max] = search_zone_finder
                                (n1,n2,n3,k0,t);

ssz = size(search_zones);
L_ssz = ssz(1);

for ii = 1:L_ssz
    h1 = search_zones(ii,1);

```

```

h2 = search_zones(ii,2);
[kap_TM_exact(ii),fval,exitflag] =
    fminbnd('eigenasymmTM2',h1,h2,[],t,k0,n1,n2,n3);
[kap_TE_exact(ii),fval,exitflag] =
    fminbnd('eigenasymm_bound',h1,h2,[],t,k0,n2,n1,n3);
end

if kap_TM_exact(length(kap_TM_exact))==kap_max
    kap_TM_exact = kap_TM_exact(1:(length(kap_TM_exact)-1));
end

if kap_TE_exact(length(kap_TE_exact))==kap_max
    kap_TE_exact = kap_TE_exact(1:(length(kap_TE_exact)-1));
end

kap_TM_exact
kap_TE_exact

```

```

%%%%%%%%%%%%%%%%%%%%%%%%%%%%%%%%%%%%%%%%%%%%%%%%%%%%%%%%%%%%%%%%%%%%%%%%
%%%%%%%%%%%%%%%%%%%%%%%%%%%%%%%%%%%%%%%%%%%%%%%%%%%%%%%%%%%%%%%%%%%%%%%%

```

### Embedded Functions Called

```

%%%%%%%%%%%%%%%%%%%%%%%%%%%%%%%%%%%%%%%%%%%%%%%%%%%%%%%%%%%%%%%%%%%%%%%%
%%%%%%%%%%%%%%%%%%%%%%%%%%%%%%%%%%%%%%%%%%%%%%%%%%%%%%%%%%%%%%%%%%%%%%%%

```

```

function [search_zones,kap_min,kap_max] = search_zone_finder
                                                (n1,n2,n3,k0,t)

```

```

%
%This function determines the search zones applicable
%for the TE and TM mode-solver algorithms

```

```

%
%

if n1>n3
    Beta_min = (1+1e-3)*n1*k0;
else
    Beta_min = (1+1e-3)*n3*k0;
end

Beta_max = (1-1e-3)*n2*k0;

kap_min = sqrt(k0^2*n2^2-Beta_max^2)
kap_max = sqrt(k0^2*n2^2-Beta_min^2);

kap_break(1) = kap_min;
pi_num = t*kap_max/pi;
num_zonebreaks = floor(t*kap_max/pi);
for ii = 1:num_zonebreaks
    break_val = (ii)*pi;
    kap_break(ii+1) = break_val/t;
end

kap_break(length(kap_break)+1) = kap_max;

search_zones = [kap_break(1:(length(kap_break)-1));
    kap_break(2:length(kap_break))]' ;

%%%%%%%%%%%%%%%%%%%%%%%%%%%%%%%%%%%%%%%%%%%%%%%%%%%%%%%%%%%%%%%%%%%%%%%%
%%%%%%%%%%%%%%%%%%%%%%%%%%%%%%%%%%%%%%%%%%%%%%%%%%%%%%%%%%%%%%%%%%%%%%%%
function y=eigenasymm_bound(kap,h,k0,ncore,nup,ndown)

```



```

y=abs(tan(kap*h)-((sqrt(k0^2*(ncore^2-nup^2)-kap^2)+
sqrt(k0^2*(ncore^2-ndown^2)-kap^2))/(kap*(1-(1/kap^2)
*(sqrt(k0^2*(ncore^2-nup^2)-kap^2)*sqrt(k0^2*
(ncore^2-ndown^2)-kap^2))))));

```

```

%%%%%%%%%%%%%%%%%%%%%%%%%%%%%%%%%%%%%%%%%%%%%%%%%%%%%%%%%%%%%%%%%%%%%%%%
%%%%%%%%%%%%%%%%%%%%%%%%%%%%%%%%%%%%%%%%%%%%%%%%%%%%%%%%%%%%%%%%%%%%%%%%

```

```

function y=eigenasymmTM2(kap2,h,k0,n1,n2,n3)
y=abs(tan(h*kap2)-((kap2*(((n2^2/n3^2)*
sqrt((sqrt(k0^2*n2^2-kap2^2))^2-k0^2*n3^2)))+
(((n2^2/n1^2)*sqrt((sqrt(k0^2*n2^2-kap2^2))^2
-k0^2*n1^2)))))/(kap2^2-(((n2^4/(n1^2*n3^2))
*sqrt((sqrt(k0^2*n2^2-kap2^2))^2-k0^2*n1^2)
*sqrt((sqrt(k0^2*n2^2-kap2^2))^2-k0^2*n3^2))))));

```

```

%%%%%%%%%%%%%%%%%%%%%%%%%%%%%%%%%%%%%%%%%%%%%%%%%%%%%%%%%%%%%%%%%%%%%%%%
%%%%%%%%%%%%%%%%%%%%%%%%%%%%%%%%%%%%%%%%%%%%%%%%%%%%%%%%%%%%%%%%%%%%%%%%

```

### B.3 Matlab Code for the Leaky Mode Slab Model

This code was written to analyze how modal leakage to a high index substrate varied as the undercladding thickness was changed. Two methods were attempted. The first method finds the exact roots of complex transcendental equation. The second method first solves a much simpler structure, and then perturbs this simplified solution to find the actual solutions.

### B.3.1 The Exact Method

#### The Top Level Calling Function

```
%%%%%%%%%%%%%%%%%%%%%%%%%%%%%%%%%%%%%%%%%%%%%%%%%%%%%%%%%%%%%%%%%%%%%%%%
%%%%%%%%%%%%%%%%%%%%%%%%%%%%%%%%%%%%%%%%%%%%%%%%%%%%%%%%%%%%%%%%%%%%%%%%

function loss_db_per_cm = Plot_leaky_imag_beta_v4(k0,t2,t3,n1,
                                                    n2,n3,n4)

%This function finds exact roots
%in the complex plain for a Leaky
%mode. This treatment is all for TE
%Put everything in per centimeter

format long;

if n1>n3
    Beta_min = 1.00001*n1*k0;
else
    Beta_min = 1.00001*n3*k0;
end
Beta_max = 0.99999*n2*k0;

btf = linspace(Beta_min,Beta_max,20000);

kx4 = (k0^2*n4^2-btf.^2).^0.5;
kx1p = (btf.^2-k0^2*n1^2).^0.5;
kx2 = (k0^2*n2^2-btf.^2).^0.5;
kx3p = (btf.^2-k0^2*n3^2).^0.5;
```

```

kx4h = kx4;
kx1ph = kx1p;
kx2h = kx2;
kx3ph = kx3p;

U = (cos(kx2.*t2)+(kx1ph./kx2).*(sin(kx2.*t2)));
V = (-(kx2./kx3ph).*(sin(kx2.*t2))+(kx1ph./kx3ph)
    .*(cos(kx2.*t2)));

yy = ((kx4h + i.*kx3p).*(U+V)+(kx4h -i.*kx3p)
    .*(U-V).*exp(-2*kx3p.*t3));

% figure(21);
% clf;
% plot(btf,imag(yy),'r*',btf,real(yy),'bo');

Roots_imag = Real_root_finder(btf,imag(yy));

Roots_real = Real_root_finder(btf,real(yy));

Beta_max_orig = Beta_max;
Beta_min_orig = Beta_min;

%Beta_im_vec = i*linspace(0,2,198);%%%%%%%%%%%%%%
Beta_im_min = 0;
Beta_im_max = 4;

mult_const = 1.05;
num_iter = 1;
for mm = 1:length(Roots_imag)

```

```

Beta_zero_imag = Roots_imag(mm);
Beta_zero_real = Roots_real(mm);
for kk = 1:num_iter
    [Beta_zero_real,Beta_zero_imag,Beta_im_min,
     Beta_im_max,Beta_im_root]
    = min_point_focus(Beta_zero_real,Beta_zero_imag,
    Beta_min_orig,Beta_max_orig,mult_const,Beta_im_min,
    Beta_im_max,k0,t2,t3,n1,n2,n3,n4);
end
loss_db_per_cm(mm) = 4.343*2*mean(imag(Beta_im_root))
end

```

```

%%%%%%%%%%%%%%%%%%%%%%%%%%%%%%%%%%%%%%%%%%%%%%%%%%%%%%%%%%%%%%%%%%%%%%%%
%%%%%%%%%%%%%%%%%%%%%%%%%%%%%%%%%%%%%%%%%%%%%%%%%%%%%%%%%%%%%%%%%%%%%%%%

```

### Embedded Functions Called

```

%%%%%%%%%%%%%%%%%%%%%%%%%%%%%%%%%%%%%%%%%%%%%%%%%%%%%%%%%%%%%%%%%%%%%%%%
%%%%%%%%%%%%%%%%%%%%%%%%%%%%%%%%%%%%%%%%%%%%%%%%%%%%%%%%%%%%%%%%%%%%%%%%
function [Beta_zero_real_new,Beta_zero_imag_new,Beta_im_min_new,
         Beta_im_max_new,Beta_im_root]
=min_point_focus(Beta_zero_real,Beta_zero_imag,Beta_min_orig,
Beta_max_orig,mult_const,Beta_im_min,Beta_im_max,k0,t2,t3
                ,n1,n2,n3,n4)
%
%This function accepts a number of variables:
%Beta_real_zero: a scalar value of the intercept of the real
%part of the eigenequation
%Beta_imag_zero: a scalar value of the intercept of the

```

```

    imaginary part of the eigenequation
%
%Beta_min_orig: a scalar: the minimum real value of the
    Beta supported by the designed structure
%
%Beta_max_orig: a scalar: the maximum real value of the
    Beta supported by the designed structure
%
%mult_const: a scalar which reduces the size of the
%search vector on successive iterations

%Beta_im_min: a scalar which gives the minimum
%imaginary Beta component to search for

%Beta_im_max: a scalar which gives the maximum
%imaginary Beta component to search for

    if Beta_zero_imag>=Beta_zero_real
        if (mult_const)*Beta_zero_imag>Beta_max_orig
            Beta_max = Beta_max_orig;
        else
            Beta_max = (mult_const)*Beta_zero_imag;
        end

        if (1/mult_const)*Beta_zero_real<Beta_min_orig
            Beta_min = Beta_min_orig;
        else
            Beta_min = (1/mult_const)*Beta_zero_real;
        end
    end

```

```

end

if Beta_zero_real>Beta_zero_imag
    if (mult_const)*Beta_zero_real>Beta_max_orig
        Beta_max = Beta_max_orig;
    else
        Beta_max = (mult_const)*Beta_zero_real;
    end

    if (1/mult_const)*Beta_zero_imag<Beta_min_orig
        Beta_min = Beta_min_orig;
    else
        Beta_min = (1/mult_const)*Beta_zero_imag;
    end
end

btf = linspace(Beta_min,Beta_max,50000);
Beta_im_vec = i*linspace(Beta_im_min,Beta_im_max,200);

for kk = 1:length(Beta_im_vec)
    btim = Beta_im_vec(kk);

    kx4 = (k0^2*n4^2-(btf +btim).^2).^0.5;
    kx1p = ((btf +btim).^2-k0^2*n1^2).^0.5;
    kx2 = (k0^2*n2^2-(btf +btim).^2).^0.5;
    kx3p = ((btf +btim).^2-k0^2*n3^2).^0.5;

    kx4h = kx4;
    kx1ph = kx1p;
    kx2h = kx2;

```

```

kx3ph = kx3p;

U = (cos(kx2.*t2)+(kx1ph./kx2).*(sin(kx2.*t2)));
V = (-(kx2./kx3ph).*(sin(kx2.*t2))+(kx1ph./kx3ph)
    .*(cos(kx2.*t2)));

yy = ((kx4h + i.*kx3p).*(U+V)+(kx4h -i.*kx3p)
    .*(U-V).*exp(-2*kx3p.*t3));

%     figure(21);
%     clf;
%     plot(btf,imag(yy),'r*',btf,real(yy),'bo');

Root_imag = Real_root_finder(btf,imag(yy));

Root_real = Real_root_finder(btf,real(yy));

if length(Root_imag)>1
    fprintf('narrowed search zone finds more than one
        root! Reduce search size\n');
    Root_imag = mean(Root_imag)
end
if length(Root_real)>1
    fprintf('narrowed search zone finds more than one
        root! Reduce search size\n');
    Root_imag = mean(Root_imag)
end
Root_imag_vec(kk) = Root_imag;
Root_real_vec(kk) = Root_real;

```

```

end

diff_roots = Root_real_vec-Root_imag_vec;
inds = find(abs(diff_roots) == min(abs(diff_roots)));
Beta_zero_real_new = mean(Root_real_vec(inds));
Beta_zero_imag_new = mean(Root_imag_vec(inds));
Beta_im_root = Real_root_finder(Beta_im_vec,diff_roots)
%   if length(Beta_im_root)>1
%       fprintf('narrowed search zone finds more than one
%           root! Reduce search size\n');
%       Beta_im_root = mean(Beta_im_root)
%   end

Beta_im_min_new = (1/mult_const)*min(imag(Beta_im_root));
Beta_im_max_new = mult_const*max(imag(Beta_im_root));
%%%%%%%%%%%%%%%%%%%%%%%%%%%%%%%%%%%%%%%%%%%%%%%%%%%%%%%%%%%%%%%%%%%%%%%%
%%%%%%%%%%%%%%%%%%%%%%%%%%%%%%%%%%%%%%%%%%%%%%%%%%%%%%%%%%%%%%%%%%%%%%%%

```

## B.3.2 The Approximate Technique

### TE Modes

```

function [alpha_TE_f] = loss_by_perturbation_TE(t2,t_vec,n1
                                                ,n2,n3,n4,k0,Neff)

%%This function takes the actual material parameters along
%%with an effective structure index which has been previously
%%determined. The wavelength must also be incorporated into
%%the wavenumber. the function returns the loss in /cm

```



```

btf = Neff*k0;

kx4 = (k0^2*n4^2-btf^2)^0.5;
kx1p = (btf^2-k0^2*n1^2)^0.5;
kx2 = (k0^2*n2^2-btf^2)^0.5;
kx3p = (btf^2-k0^2*n3^2)^0.5;

kx4h = kx4;
kx1ph = kx1p;
kx2h = kx2;
kx3ph = kx3p;

for ii = 1:length(t_vec)
    t3 = t_vec(ii);

    teff = t2 + 1/kx1p + 1/kx3p;
    WTE = btf*teff*(kx2^2+kx3p^2);

    dbeta = 2*kx2^2*kx3ph*((kx4h-j*kx3p)/(kx4h+j*kx3p))
            *exp(-2*kx3p*t3)/WTE;

    betaTE = btf+dbeta;
    betaTE_im =imag(betaTE);
    if k0>5e5
        alpha_TE_f(ii) = -4.3429*(2*betaTE_im)/100;
        %db per centimeter,%all units in the program
        %are in meters
    else
        alpha_TE_f(ii) = -4.3429*(2*betaTE_im);
        %db per centimeter,%all units in the program
    end
end

```

```

                %are in meters
            end
        end

figure(40);
clf;
semilogy(t_vec,alpha_TE_f,'ro')
a = 1;

```

### TM Modes

```

function [alpha_TM_f] = loss_by_perturbation_TM(t2,t_vec,n1,
                                                n2,n3,n4,k0,Neff)

```

```

    btmf = Neff*k0;

```

```

    kx4 = (k0^2*n4^2-btmf^2)^0.5;

```

```

    kx1p = (btmf^2-k0^2*n1^2)^0.5;

```

```

    kx2 = (k0^2*n2^2-btmf^2)^0.5;

```

```

    kx3p = (btmf^2-k0^2*n3^2)^0.5;

```

```

    kx4h = (n3/n4)^2*(k0^2*n4^2-btmf^2)^0.5;

```

```

    kx1ph = (n2/n1)^2*(btmf^2-k0^2*n1^2)^0.5;

```

```

    kx2h = (k0^2*n2^2-btmf^2)^0.5;

```

```

    kx3ph = (n2/n3)^2*(btmf^2-k0^2*n3^2)^0.5;

```

```

    for ii = 1:length(t_vec)

```

```

        t3 = t_vec(ii);

```

```

teffTM = t2 + 1/kx1p + 1/kx3p;
WA = t2*(kx2^2+kx3ph^2);
WB = (kx3ph/kx3p^2)*(kx2^2+kx3p^2);
WC = (kx1ph/kx1p^2)*(kx2^2+kx3ph^2)*(kx1p^2+kx2^2);
WD = (kx1ph^2+kx2^2);

WTM = btmf*(WA+WB+(WC/WD));

dbetaTM = 2*kx2^2*kx3ph*((kx4h-j*kx3p)/(kx4h+j*kx3p))
          *exp(-2*kx3p*t3)/WTM;

betaTM = btmf+dbetaTM;
betaTM_im = imag(betaTM);
if k0>5e5
    alpha_TM_f(ii) = -4.3429*(2*betaTM_im)/100;
    %db per centimeter, all units in the program
    %are in meters
else
    alpha_TM_f(ii) = -4.3429*(2*betaTM_im);
    %db per centimeter, all units in the program
    %are in meters
end
end

figure(41);
clf;
semilogy(t_vec,alpha_TM_f,'g^')

```

## B.4 Matlab Code for the Four-Layer Slab Model

A Matlab program was written to analyze structures such as that shown in Fig. 2.3(b). The code analyzes two separate four-layer slab regions, one for the guiding region of Fig. 2.3(b), and one for the cladding region of Fig. 2.3(b). The effective indices are then used to calculate predicted 2D waveguide modes. The solver only analyzes the four-layer slab waveguide in TE polarization.

### The Top Level Calling Function

```
%%%%%%%%%%%%%%%%%%%%%%%%%%%%%%%%%%%%%%%%%%%%%%%%%%%%%%%%%%%%%%%%%%%%%%%%%%%%%%
%%%%%%%%%%%%%%%%%%%%%%%%%%%%%%%%%%%%%%%%%%%%%%%%%%%%%%%%%%%%%%%%%%%%%%%%%%%%%%
function [I_norm,subs_tot] = fourlayer_eigen_v3
%
%An eigenequation for a four-layer slab model
%The first step in a solver for quasi-TE waveguide modes
%
%
%

warning('off'); %suppresses warning messages

%%%%%%%%%%%%%%%%%%%%%%%%%%%%%%%%%%%%%%%%%%%%%%%%%%%%%%%%%%%%%%%%%%%%%%%%%%%%%%INDICES%%%%%%%%%%%%%%%%%%%%%%%%%%%%%%%%%%%%%%%%%%%%%%%%%%%%%%%%%%%%%%%%%%%%%%%%%%%%%%
ns =1.46; %(PECVD silica)
nf = 1.9; %(silicon monoxide)
nc =1.46; %(PECVD silica)
na = 1;  %(the index of air)
```

```

%%%%%%%%%%%%%%%%%%%%%%%%%%%%%%%%%%%%%%%%%%%%%%%%%%%%%%%%%%%%%%%%%%%%%%%%GENERAL CONSTANTS%%%%%%%%%%%%%%%%%%%%%%%%%%%%%%%%%%%%%%%%%%%%%%%%%%%%%%%%%%%%%%%%%%%%%%%%
lam = 1.55e-6; %meters
k0 = 2*pi/lam;
point_dim = 0.0125e-6 %distance between points in the
                    plotted electric %field functions
%Define root of -1
ii = (-1)^0.5;

%%%%%%%%%%%%%%%%%%%%%%%%%%%%%%%%%%%%%%%%%%%%%%%%%%%%%%%%%%%%%%%%%%%%%%%%BETA RANGE%%%%%%%%%%%%%%%%%%%%%%%%%%%%%%%%%%%%%%%%%%%%%%%%%%%%%%%%%%%%%%%%%%%%%%%%
Beta = linspace(k0*ns,0.999*k0*nf,100000); %prefactors get
                    %rid of zero at end of value range

%the gamma coefficients for each of the layers%%

gam_a = (Beta.^2-k0^2*na^2).^0.5;
gam_c = (Beta.^2-k0^2*nc^2).^0.5;
gam_f = (k0^2*nf^2-Beta.^2).^0.5;
gam_s = (Beta.^2-k0^2*ns^2).^0.5;

%%%%%%%%%%%%%%%%%%%%%%%%%%%%%%%%%%%%%%%%%%%%%%%%%%%%%%%%%%%%%%%%%%%%%%%%THE GUIDE DIMENSIONS%%%%%%%%%%%%%%%%%%%%%%%%%%%%%%%%%%%%%%%%%%%%%%%%%%%%%%%%%%%%%%%%%%%%%%%%
guiding_layer_height = 1.0e-6;
guiding_width = 4e-6;
rib_cladding = 0.05e-6
rib_height = 0.65e-6;

df = guiding_layer_height;
df2 = guiding_width
dc_vec = [rib_height rib_cladding]

```

```

for kk = 1:2
    if kk==1
        disp('We are searching for the effective
              index of the guiding region');
    else
        disp('We are searching for the effective
              index of the slab region');
    end
    dc = dc_vec(kk)

    %Parts of eigenequation

    Part1=-exp(ii.*gam_f.*df).*((1+exp(-2.*ii.*gam_f.*df)
        .*((ii.*gam_f-gam_s)./(ii.*gam_f+gam_s)))
        ./((1+exp(-2.*gam_c.*dc).*((gam_c-gam_a)
        ./((gam_c+gam_a))))).*gam_c;

    Part2=exp(ii.*gam_f.*df).*((1+exp(-2.*ii.*gam_f.*df)
        .*((ii.*gam_f-gam_s)./(ii.*gam_f+gam_s)))
        ./((1+exp(2.*gam_c.*dc).*((gam_c+gam_a)
        ./((gam_c-gam_a))))).*gam_c;

    Part3 = -ii.*gam_f.*exp(ii.*gam_f.*df);

    Part4 = ii.*gam_f.*exp(-ii.*gam_f.*df).*
        ((ii.*gam_f-gam_s)./(ii.*gam_f+gam_s));

    eigen = Part1+Part2+Part3+Part4;

    figure(2);

```

```

clf;
plot(Beta,abs(eigen));

Beta_val(kk) = input('What is Beta? ');
close(2);

Effective_index(kk) = Beta_val(kk)/k0;

end
%CONSTRUCTION AND PLOT OF THE ELECTRIC FIELD AND INTENSITY FIELD

clear Beta %gets rid of the vector of Beta used to search
           %for the propagation constants of the slab and
           %guiding regions

Beta = Beta_val(1); % Beta for the guiding region
dc = rib_height; %sets the value for the rib zone
gam_A = (Beta.^2-k0^2*na^2).^0.5;
gam_C = (Beta.^2-k0^2*nc^2).^0.5;
gam_F = (k0^2*nf^2-Beta.^2).^0.5;
gam_S = (Beta.^2-k0^2*ns^2).^0.5;

E = 1;
F = E*((ii*gam_F-gam_S)/(ii*gam_F+gam_S));
C = E*exp(ii*gam_F*df)*((1+exp(-2*ii*gam_F*df))*((ii*gam_F-gam_S)
/(ii*gam_F+gam_S)))/(1+exp(-2*gam_C*dc)*((gam_C-gam_A)
/(gam_C+gam_A))));
D=E*exp(ii*gam_F*df)*((1+exp(-2*ii*gam_F*df))*((ii*gam_F-gam_S)
/(ii*gam_F+gam_S)))/(1+exp(2*gam_C*dc)*((gam_C+gam_A)
/(gam_C-gam_A))));

```

```

D2 = C*exp(-2*gam_C*dc)*((gam_C-gam_A)/(gam_C+gam_A));
A = C*exp(-gam_C*dc)+D*exp(gam_C*dc);
H = E+F;

subs_ind = linspace(-2e-6,0,(0--2e-6)/point_dim+1);
subs_vals = H.*exp(gam_S.*subs_ind);
% figure(5);
% clf;
% plot(subs_ind,subs_vals);

subs_film = linspace(point_dim,df,df/point_dim);
film_vals = E*exp(ii.*gam_F.*subs_film)+F
            .*exp(-ii.*gam_F.*subs_film);
% figure(6);
% clf;
% plot(subs_film,film_vals);

subs_clad = linspace(df+point_dim,df+dc,dc/point_dim);
clad_vals = C*exp(-gam_C.*(subs_clad-df))+D
            .*exp(gam_C*(subs_clad-df));
% figure(7);
% clf;
% plot(subs_clad,clad_vals);

subs_air = linspace(df+dc+point_dim,df+dc+2e-6,2e-6/point_dim);
air_vals = A*exp(-gam_A*(subs_air-(df+dc)));
% figure(8);
% clf;
% plot(subs_air,air_vals);
%%%%%%%%%%%%%%%%%%%%%%%%%%%%%%%%%%%%%%%%%%%%%%%%%%%%%%%%%%%%%%%%%%%%%%%%

```



```

subs_tot = [subs_ind subs_film subs_clad subs_air];
field_tot = [subs_vals film_vals clad_vals air_vals];
field_tot_norm = field_tot/max(field_tot);
I_norm = field_tot_norm.^2;

% figure(4);
% clf;
% plot(subs_tot,abs(field_tot_norm));
% hold on;
% plot(subs_tot,I_norm,'r');

%AREA WHICH LINKS FIRST AND SECOND PART
Ncore = Effective_index(1)
Nclad = Effective_index(2)

field = I_norm;
field_ind = subs_tot;

%%%%%%%%%%%%%%%%%%%%%%%%%%%%%%%%%%%%%%%%%%%%%%%%%%%%%%%%%%%%%%%%%%%%%%%%
%THE SECOND PART OF THE EFFECTIVE INDEX METHOD%
%THIS PART SOLVES A TM EIGENEQUATION FROM LIFANTES%
%%%%%%%%%%%%%%%%%%%%%%%%%%%%%%%%%%%%%%%%%%%%%%%%%%%%%%%%%%%%%%%%%%%%%%%%
diff = (Ncore-Nclad)/1000;
N = linspace(Nclad+diff,Ncore-diff,10000);
b = ((N.^2-Nclad^2)/(Ncore^2-Nclad^2));
V = k0*df2*(Ncore^2-Nclad^2)^0.5;
a = 0;
gam_1 = (Nclad/Ncore)^2;
gam_2 = gam_1;

```

```

Part1 = 1/gam_1.*(b./(1-b)).^0.5;
Part2 = 1/gam_2.*((b+a)./(1-b)).^0.5;
Part3 = 1-(1/(gam_1*gam_2))*((b.*(b+a)).^0.5./(1-b));
Part4 = tan(V.*(1-b).^0.5);

f = (Part1+Part2)./Part3 - Part4;
f2 = (Part1+Part2)./Part3;

figure(10);
clf;
plot(N,f,'ro');
axis([N(1) N(length(N)) -100 100]);
grid on;
% figure(11);
% clf;
% plot(N,f2);
% hold on;
% plot(N,Part4,'ro');
% grid on;
N2 = input('what is the effective index? ');
close(10)

Beta2 = k0*N2;

gam_C2 = (Beta2^2-k0^2*Nclad^2)^0.5;
gam_S2 = gam_C2;
kappa_f2 = (k0^2*Ncore^2-Beta2^2)^0.5;

xClad1 = linspace(0,8e-6,(8e-6-0)/point_dim);

```

```

function EIM_fundamental_modes_v2(k0,t1,t2,n1,
    n2,n3,n4,n5,mode_order_vert,mode_order_horiz)
%
%
%
%This function applies the effective index method
%to determine the approximate modal profiles
%of the fundamental quasi-TE and quasi-TM guided modes in a
%rectangular waveguide (stripe waveguide)
%
%Parameters:
%k0 - free space radial wavenumber
%t1 - vertical dimension (height) of the waveguide
%t2 - horizontal dimension (width) of the waveguide
%n1 - index above the waveguide core
%n2 - index of the waveguide core
%n3 - index below the waveguide core
%n4 - index to the left of the waveguide core
    (looking at the face)
%n5 - index to the right of the waveguide core
    (looking at the face)
%mode_order - allows you to search for higher
    order modal effective indices

if k0<1e6
    eps_0 = 8.85e-14;
    c = 3e10;
else
    eps_0 = 8.85e-12;
    c = 3e8;

```

```

end
lam = 2*pi/k0;
omega = 2*pi*c/lam;
spanx = 5*t1;
spany = 3*t2;
vert_vals = linspace((-spanx-t1)/2,(spanx-t1)/2,750);
E_above_0_sub_x = vert_vals(find(vert_vals>=0));
E_film_sub_x = vert_vals(find(vert_vals<0 &vert_vals>=-t1));
E_film_subs_sub_x = vert_vals(find(vert_vals<-t1));
subx = [E_film_subs_sub_x';E_film_sub_x';E_above_0_sub_x'];
horiz_vals = linspace((-spany-t2)/2,(spany-t2)/2,750);
E_above_0_sub_y = horiz_vals(find(horiz_vals>=0));
E_film_sub_y = horiz_vals(find(horiz_vals<0 &horiz_vals >=-t2));
E_film_subs_sub_y = horiz_vals(find(horiz_vals<-t2));
suby = [E_film_subs_sub_y';E_film_sub_y';E_above_0_sub_y'];

%%%QUASI-TE Fundamental mode
%First part of the effective index method

[search_zones,kap_min,kap_max] = search_zone_finder
                                (n1,n2,n3,k0,t1);
%For quasi-TE modes we start with a TE solver
kap_low = search_zones(mode_order_vert,1);
kap_high = search_zones(mode_order_vert,2);
[kap_TE_part1,fval,exitflag] = fminbnd('eigenasymm_bound'
    ,kap_low,kap_high,[],t1,k0,n2,n1,n3);

Beta_TE_part1 = sqrt(k0^2*n2^2-kap_TE_part1^2);
Neff_TE = Beta_TE_part1/k0

```

```

gam1_qTE = sqrt(Beta_TE_part1^2-k0^2*n1^2);
gam3_qTE = sqrt(Beta_TE_part1^2-k0^2*n3^2);

E_above_0_qTE = exp(-gam1_qTE.*E_above_0_sub_x);
E_film_qTE = cos(kap_TE_part1.*E_film_sub_x)
    -(gam1_qTE/kap_TE_part1).*sin(kap_TE_part1
    .*E_film_sub_x);
E_film_subs_qTE = (cos(kap_TE_part1.*t1)+
    (gam1_qTE/kap_TE_part1).*sin(kap_TE_part1.*t1))
    *exp(gam3_qTE.*(E_film_subs_sub_x+t1));

Ex_qTE = [E_film_subs_qTE';E_film_qTE';E_above_0_qTE'];
Ex_qTE_n = Ex_qTE./max(Ex_qTE);
Ix_qTE_n = Ex_qTE_n.^2;

P_in_film_TE_p1 = trapz(E_film_sub_x,(E_film_qTE
    ./max(E_film_qTE)).^2)/trapz(vert_vals,Ix_qTE_n);

figure(30);
clf;
plot(vert_vals,Ix_qTE_n,'g^');

%Second part of the effective index method

[search_zones_part2,kap_min,kap_max] = search_zone_finder
    (n4,Neff_TE,n5,k0,t2);
kap_low = search_zones_part2(mode_order_horiz,1);
kap_high = search_zones_part2(mode_order_horiz,2);
%For quasi-TE modes we finish with a TM solver

```

```

[kap_TM_part2,fval,exitflag] = fminbnd('eigenasymmTM2',
    kap_low,kap_high,[],t2,k0,n4,Neff_TE,n5);

Beta_qTE_00 = sqrt(k0^2*Neff_TE^2-kap_TM_part2^2);
Neff_qTE_00 = Beta_qTE_00/k0

gam4_qTE = sqrt(Beta_qTE_00^2-k0^2*n4^2);
gam5_qTE = sqrt(Beta_qTE_00^2-k0^2*n5^2);

H_2_Econv_qTE = Beta_qTE_00/(omega*eps_0);

E_above_0y_qTE = (H_2_Econv_qTE/n5^2)*(exp(-gam5_qTE
    .*E_above_0_sub_y));
E_filmy_qTE = (H_2_Econv_qTE/Neff_TE^2)*(cos(kap_TM_part2
    .*E_film_sub_y)-(Neff_TE^2/n5^2)*(gam5_qTE/kap_TM_part2
    .*sin(kap_TM_part2.*E_film_sub_y)));
E_film_subsy_qTE = (H_2_Econv_qTE/n4^2)*
    ((cos(kap_TM_part2.*t2)+(Neff_TE^2/n5^2)
    *(gam5_qTE/kap_TM_part2).*sin(kap_TM_part2.*t2))
    *exp(gam4_qTE.*(E_film_subs_sub_y+t2)));

Ey_qTE = [E_film_subsy_qTE';E_filmy_qTE';E_above_0y_qTE'];
Ey_qTE_n = Ey_qTE./max(Ey_qTE);
Iy_qTE_n = Ey_qTE_n.^2;

P_in_film_TE_p2 = trapz(E_film_sub_y,(E_filmy_qTE
    ./max(E_filmy_qTE)).^2)/trapz(horiz_vals,Iy_qTE_n);
P_in_film_TE = P_in_film_TE_p1.*P_in_film_TE_p2

```

```

figure(30);
hold on;
plot(horiz_vals,Iy_qTEEn,'r^');

L_vert = length(vert_vals);
L_horiz = length(horiz_vals);

Ix_qTEEn_mat = repmat(Ix_qTEEn,1,L_vert);
Iy_qTEEn_mat = repmat(Iy_qTEEn',L_vert,1);

% figure(33);
% mesh(subx,suby,Ix_qTEEn_mat);
% view(2);
% figure(34);
% clf;
% mesh(subx,suby,Iy_qTEEn_mat);
% view(2);

qTEEn_field = Ix_qTEEn_mat.*Iy_qTEEn_mat;
figure(32);
clf;
mesh(subx,suby,qTEEn_field);
view(2);
H_modefield = field_size(Iy_qTEEn,suby)
V_modefield = field_size(Ix_qTEEn,subx)

%%%%%%%%%%%%%%%%%%%%%%%%%%%%%%%%%%%%%%%%%%%%%%%%%%%%%%%%%%%%%%%%%%%%%%%%%
%%%%%%%%%%%%%%%%%%%%%%%%%%%%%%%%%%%%%%%%%%%%%%%%%%%%%%%%%%%%%%%%%%%%%%%%%
%%%%%%%%%%%%%%%%%%%%%%%%%%%%%%%%%%%%%%%%%%%%%%%%%%%%%%%%%%%%%%%%%%%%%%%%%

```

```

%%%%%%%%%%%%%%%%%%%%%%%%%%%%%%%%%%%%%%%%%%%%%%%%%%%%%%%%%%%%%%%%%%%%%%%%
%%%%%%%%%%%%%%%%%%%%%%%%%%%%%%%%%%%%%%%%%%%%%%%%%%%%%%%%%%%%%%%%%%%%%%%%

[search_zones_qTM1,kap_min,kap_max] = search_zone_finder
                                     (n1,n2,n3,k0,t1);

%For quasi-TM modes we start with a TM solver
kap_low = search_zones_qTM1(mode_order_vert,1);
kap_high = search_zones_qTM1(mode_order_vert,2);
[kap_TM_part1,fval,exitflag] = fminbnd('eigenasymmTM2',
                                     kap_low,kap_high,[],t1,k0,n1,n2,n3);

Beta_TM_part1 = sqrt(k0^2*n2^2-kap_TM_part1^2);
Neff_TM = Beta_TM_part1/k0

H_2_Econv_qTM = Beta_TM_part1/(omega*eps_0);

gam1_qTM = sqrt(Beta_TM_part1^2-k0^2*n1^2);
gam3_qTM = sqrt(Beta_TM_part1^2-k0^2*n3^2);

E_above_0_qTM = (H_2_Econv_qTM/n1^2)
                *(exp(-gam1_qTM.*E_above_0_sub_x));
E_film_qTM = (H_2_Econv_qTM/n2^2)*(cos(kap_TM_part1
.*E_film_sub_x)-(n2^2/n1^2)*(gam1_qTM/kap_TM_part1)
.*sin(kap_TM_part1.*E_film_sub_x));
E_film_subs_qTM = (H_2_Econv_qTM/n3^2)*
                ((cos(kap_TM_part1.*t1)+(n2^2/n1^2)*
                (gam1_qTM/kap_TM_part1).*sin(kap_TM_part1.*t1))
                *exp(gam3_qTM.*(E_film_subs_sub_x+t1)));

Ex_qTM = [E_film_subs_qTM';E_film_qTM';E_above_0_qTM'];

```



```

Ex_qTMn = Ex_qTM./max(Ex_qTM);
Ix_qTMn = Ex_qTMn.^2;

figure(31);
clf;
plot(vert_vals,Ix_qTMn,'ro');

%Second part of the effective index method

[search_zones_part2,kap_min,kap_max] = search_zone_finder
                                     (n4,Neff_TM,n5,k0,t2);
kap_low = search_zones_part2(mode_order_horiz,1);
kap_high = search_zones_part2(mode_order_horiz,2);
%For quasi-TM modes we finish with a TE solver
[kap_TE_part2,fval,exitflag] = fminbnd('eigenasymm_bound',
                                     kap_low,kap_high,[],t2,k0,Neff_TM,n4,n5);

Beta_qTM_00 = sqrt(k0^2*Neff_TM^2-kap_TE_part2^2);
Neff_qTM_00 = Beta_qTM_00/k0

gam4_qTM = sqrt(Beta_qTM_00^2-k0^2*n4^2);
gam5_qTM = sqrt(Beta_qTM_00^2-k0^2*n5^2);

E_above_0y = exp(-gam5_qTM.*E_above_0_sub_y);
E_film_y = cos(kap_TE_part2.*E_film_sub_y)-(gam5_qTM
        /kap_TE_part2).*sin(kap_TE_part2.*E_film_sub_y);
E_film_subsy = (cos(kap_TE_part2.*t2)+(gam5_qTM
        /kap_TE_part2).*sin(kap_TE_part2.*t2))

```

```

*exp(gam4_qTM.*(E_film_subs_sub_y+t2));

Ey_qTM = [E_film_subsy';E_filmy';E_above_0y'];

Ey_qTMn = Ey_qTM./max(Ey_qTM);
Iy_qTMn = Ey_qTMn.^2;

figure(31);
hold on;
plot(suby,Iy_qTMn,'bo');

Ix_qTMn_mat = repmat(Ix_qTMn,1,L_horiz);
Iy_qTMn_mat = repmat(Iy_qTMn',L_vert,1);

% figure(35);
% mesh(subx,suby,Ix_qTMn_mat);
% view(2);
% figure(36);
% clf;
% mesh(subx,suby,Iy_qTMn_mat);
% view(2);

qTM_field = Ix_qTMn_mat.*Iy_qTMn_mat;
figure(33);
clf;
mesh(subx,suby,qTM_field);
view(2);
H_qTM_modefield = field_size(Iy_qTMn,suby)
V_qTM_modefield = field_size(Ix_qTMn,subx)

```

```

xfilm = linspace(-df2,-point_dim,df2/point_dim);
xClad2 = linspace(-df2-8e-6,-df2-point_dim,
    ((-df2-point_dim)-(-df2-8e-6))/point_dim);

Clad1_vals = exp(-gam_C2.*xClad1);
E_Clad1_vals = Clad1_vals./Nclad^2;
film_vals = cos(kappa_f2.*xfilm)-Ncore^2/Nclad^2
    *gam_C2/kappa_f2*sin(kappa_f2.*xfilm);
E_film_vals = film_vals./Ncore^2;
Clad2_vals = (cos(kappa_f2.*df2)+Ncore^2/Nclad^2*gam_C2
    /kappa_f2*sin(kappa_f2.*df2))*exp(gam_S2.*(xClad2+df2));
E_Clad2_vals = Clad2_vals./Nclad^2;

ind = [xClad2 xfilm xClad1];
vals = [Clad2_vals film_vals Clad1_vals];
E_vals = [E_Clad2_vals E_film_vals E_Clad1_vals];
vals_norm = vals/max(vals);
E_vals_norm = E_vals/max(E_vals);
I_vals_norm = E_vals_norm.^2;

% figure(12)
% clf;
% plot(ind,E_vals_norm);
% hold on;
% plot(ind,I_vals_norm,'r');
field_f = fliplr(field); %reverses the field so that
    %bottom winds up on bottom
field_tot = field_f'*I_vals_norm; %constructs Intensity field
size(field_tot);
figure(13);

```

```

clf;
mesh(ind,field_ind,real(field_tot));
VIEW(2);

spotsizes_vert = field_size(I_norm,subs_tot)
spotsizes_horiz = field_size(I_vals_norm,ind)

guide_region_overlap(field_tot,subs_tot,ind
    ,guiding_layer_height,0);

warning('on')

%%%%%%%%%%%%%%%%%%%%%%%%%%%%%%%%%%%%%%%%%%%%%%%%%%%%%%%%%%%%%%%%%%%%%%%%
%%%%%%%%%%%%%%%%%%%%%%%%%%%%%%%%%%%%%%%%%%%%%%%%%%%%%%%%%%%%%%%%%%%%%%%%

```

**Embedded Functions Called**

```

%%%%%%%%%%%%%%%%%%%%%%%%%%%%%%%%%%%%%%%%%%%%%%%%%%%%%%%%%%%%%%%%%%%%%%%%
%%%%%%%%%%%%%%%%%%%%%%%%%%%%%%%%%%%%%%%%%%%%%%%%%%%%%%%%%%%%%%%%%%%%%%%%
function [spotsizes] = field_size(field,field_ind)
%
%This function takes a given field and calculates the
% 1/e2 values. It returns the width of the between the
%1/e2 values, commonly referred to as the spot size.
%

field_norm = real(field)/max(real(field));
value = exp(-2); %standard modefield diameter value
% value = 0.5;

```

```

% value = exp(-1);

field_norm_shift = field_norm-value;
for kk = 1:(length(field)-1)
    fns_mult(kk) = field_norm_shift(kk)*field_norm_shift(kk+1);
end
inds = find(fns_mult <0);
low_point = field_ind(inds(1));
high_point = field_ind(inds(length(inds))+1);
spotsize = high_point-low_point;

%%%%%%%%%%%%%%%%%%%%%%%%%%%%%%%%%%%%%%%%%%%%%%%%%%%%%%%%%%%%%%%%%%%%%%%%
%%%%%%%%%%%%%%%%%%%%%%%%%%%%%%%%%%%%%%%%%%%%%%%%%%%%%%%%%%%%%%%%%%%%%%%%
function [percentage_overlap] =
guide_region_overlap(field,sup_vec_vert,sup_vec_horiz,
                    upper_boundary,lower_boundary)
%
%This function calculates the percentage of a fundamental
%mode which overlaps%with the structural high-index guiding
layer. Necessary to optimize mode-overlap with an active
%medium such as erbium
%
%really seems only completely valid for
%rib-loaded/strip-loaded guides
%

field_val_tot = sum(sum(field));

inds = find(sup_vec_vert>=lower_boundary &
            sup_vec_vert<=upper_boundary);

```

```

field_overlap = field(inds,:);

field_val_overlap = sum(sum(field_overlap));

percentage_overlap = real(field_val_overlap)/real(field_val_tot)

```

```

%%%%%%%%%%%%%%%%%%%%%%%%%%%%%%%%%%%%%%%%%%%%%%%%%%%%%%%%%%%%%%%%%%%%%%%%
%%%%%%%%%%%%%%%%%%%%%%%%%%%%%%%%%%%%%%%%%%%%%%%%%%%%%%%%%%%%%%%%%%%%%%%%

```

## B.5 Matlab Code for the Effective Index Method (EIM)

Matlab code was written to predict quasi-TE and quasi-TM modes in  $2D$  strip waveguides. A schematic of the modeled structure is shown in Fig. 2.5(a). Only one modal solution is plotted per call to the function, but the modal order is controllable by setting a pair of integers in the function call. This function has several embedded functions, though, all of the embedded functions have been shown in the previous coding sections.

### The Top Level Calling Function

```

%%%%%%%%%%%%%%%%%%%%%%%%%%%%%%%%%%%%%%%%%%%%%%%%%%%%%%%%%%%%%%%%%%%%%%%%
%%%%%%%%%%%%%%%%%%%%%%%%%%%%%%%%%%%%%%%%%%%%%%%%%%%%%%%%%%%%%%%%%%%%%%%%
function EIM_fundamental_modes_v2(k0,t1,t2,n1,n2,n3,n4,n5,
                                mode_order_vert,mode_order_horiz)

%
%
%
%This function applies the effective index method

```

```

%to determine the approximate modal profiles
%of the fundamental quasi-TE and quasi-TM guided modes in a
%rectangular waveguide (stripe waveguide)
%
%Parameters:
%k0 - free space radial wavenumber
%t1 - vertical dimension (height) of the waveguide
%t2 - horizontal dimension (width) of the waveguide
%n1 - index above the waveguide core
%n2 - index of the waveguide core
%n3 - index below the waveguide core
%n4 - index to the left of the waveguide core (looking at the
      face)
%n5 - index to the right of the waveguide core (looking at the
      face)
%mode_order - allows you to search for higher order modal
               effective indices

if k0<1e6
    eps_0 = 8.85e-14;
    c = 3e10;
else
    eps_0 = 8.85e-12;
    c = 3e8;
end
lam = 2*pi/k0;
omega = 2*pi*c/lam;
spanx = 5*t1;
spany = 3*t2;
vert_vals = linspace((-spanx-t1)/2,(spanx-t1)/2,750);

```

```

E_above_0_sub_x = vert_vals(find(vert_vals>=0));
E_film_sub_x = vert_vals(find(vert_vals<0 &vert_vals>=-t1));
E_film_subs_sub_x = vert_vals(find(vert_vals<-t1));
subx = [E_film_subs_sub_x';E_film_sub_x';E_above_0_sub_x'];
horiz_vals = linspace((-spany-t2)/2,(spany-t2)/2,750);
E_above_0_sub_y = horiz_vals(find(horiz_vals>=0));
E_film_sub_y = horiz_vals(find(horiz_vals<0
    &horiz_vals >=-t2));
E_film_subs_sub_y = horiz_vals(find(horiz_vals<-t2));
suby = [E_film_subs_sub_y';E_film_sub_y';E_above_0_sub_y'];

%%%QUASI-TE Fundamental mode
%First part of the effective index method

[search_zones,kap_min,kap_max] = search_zone_finder
    (n1,n2,n3,k0,t1);
%For quasi-TE modes we start with a TE solver
kap_low = search_zones(mode_order_vert,1);
kap_high = search_zones(mode_order_vert,2);
[kap_TE_part1,fval,exitflag] = fminbnd('eigenasymm_bound',
    kap_low,kap_high,[],t1,k0,n2,n1,n3);

Beta_TE_part1 = sqrt(k0^2*n2^2-kap_TE_part1^2);
Neff_TE = Beta_TE_part1/k0

gam1_qTE = sqrt(Beta_TE_part1^2-k0^2*n1^2);
gam3_qTE = sqrt(Beta_TE_part1^2-k0^2*n3^2);

E_above_0_qTE = exp(-gam1_qTE.*E_above_0_sub_x);
E_film_qTE = cos(kap_TE_part1.*E_film_sub_x)

```



```

    -(gam1_qTE/kap_TE_part1).*sin(kap_TE_part1
    .*E_film_sub_x);
E_film_subs_qTE = (cos(kap_TE_part1.*t1)+
    (gam1_qTE/kap_TE_part1).*sin(kap_TE_part1
    .*t1))*exp(gam3_qTE.*(E_film_subs_sub_x+t1));

Ex_qTE = [E_film_subs_qTE';E_film_qTE';E_above_0_qTE'];
Ex_qTEn = Ex_qTE./max(Ex_qTE);
Ix_qTEn = Ex_qTEn.^2;

P_in_film_TE_p1 = trapz(E_film_sub_x,(E_film_qTE
    ./max(E_film_qTE)).^2)/trapz(vert_vals,Ix_qTEn);

figure(30);
clf;
plot(vert_vals,Ix_qTEn,'g^');

%Second part of the effective index method

[search_zones_part2,kap_min,kap_max] = search_zone_finder
    (n4,Neff_TE,n5,k0,t2);
kap_low = search_zones_part2(mode_order_horiz,1);
kap_high = search_zones_part2(mode_order_horiz,2);
%For quasi-TE modes we finish with a TM solver
[kap_TM_part2,fval,exitflag] = fminbnd('eigenasymmTM2',
    kap_low,kap_high,[],t2,k0,n4,Neff_TE,n5);

Beta_qTE_00 = sqrt(k0^2*Neff_TE^2-kap_TM_part2^2);
Neff_qTE_00 = Beta_qTE_00/k0

```

```

gam4_qTE = sqrt(Beta_qTE_00^2-k0^2*n4^2);
gam5_qTE = sqrt(Beta_qTE_00^2-k0^2*n5^2);

H_2_Econv_qTE = Beta_qTE_00/(omega*eps_0);

E_above_0y_qTE = (H_2_Econv_qTE/n5^2)*(exp(-gam5_qTE
    .*E_above_0_sub_y));
E_filmy_qTE = (H_2_Econv_qTE/Neff_TE^2)*(cos(kap_TM_part2
    .*E_film_sub_y)-(Neff_TE^2/n5^2)*(gam5_qTE
    /kap_TM_part2).*sin(kap_TM_part2.*E_film_sub_y));
E_film_subsy_qTE = (H_2_Econv_qTE/n4^2)*((cos(kap_TM_part2
    .*t2)+(Neff_TE^2/n5^2)*(gam5_qTE/kap_TM_part2)
    .*sin(kap_TM_part2.*t2))*exp(gam4_qTE.*
    (E_film_subs_sub_y+t2)));

Ey_qTE = [E_film_subsy_qTE';E_filmy_qTE';E_above_0y_qTE'];
Ey_qTE_n = Ey_qTE./max(Ey_qTE);
Iy_qTE_n = Ey_qTE_n.^2;

P_in_film_TE_p2 = trapz(E_film_sub_y,(E_filmy_qTE
    ./max(E_filmy_qTE)).^2)/trapz(horiz_vals,Iy_qTE_n);
P_in_film_TE = P_in_film_TE_p1.*P_in_film_TE_p2

figure(30);
hold on;
plot(horiz_vals,Iy_qTE_n,'r^');

L_vert = length(vert_vals);

```

```

L_horiz = length(horiz_vals);

Ix_qTEEn_mat = repmat(Ix_qTEEn,1,L_vert);
Iy_qTEEn_mat = repmat(Iy_qTEEn',L_vert,1);

% figure(33);
% mesh(subx,suby,Ix_qTEEn_mat);
% view(2);
% figure(34);
% clf;
% mesh(subx,suby,Iy_qTEEn_mat);
% view(2);

qTEEn_field = Ix_qTEEn_mat.*Iy_qTEEn_mat;
figure(32);
clf;
mesh(subx,suby,qTEEn_field);
view(2);
H_modefield = field_size(Iy_qTEEn,suby)
V_modefield = field_size(Ix_qTEEn,subx)

%%%%%%%%%%%%%%%%%%%%%%%%%%%%%%%%%%%%%%%%%%%%%%%%%%%%%%%%%%%%%%%%%%%%%%%%%
%%%%%%%%%%%%%%%%%%%%%%%%%%%%%%%%%%%%%%%%%%%%%%%%%%%%%%%%%%%%%%%%%%%%%%%%%
%%%%%%%%%%%%%%%%%%%%%%%%%%%%%%%%%%%%%%%%%%%%%%%%%%%%%%%%%%%%%%%%%%%%%%%%%
%%%%%%%%%%%%%%%%%%%%%%%%%%%%%%%%%%%%%%%%%%%%%%%%%%%%%%%%%%%%%%%%%%%%%%%%%
%%%%%%%%%%%%%%%%%%%%%%%%%%%%%%%%%%%%%%%%%%%%%%%%%%%%%%%%%%%%%%%%%%%%%%%%%

[search_zones_qTM1,kap_min,kap_max] = search_zone_finder
                                     (n1,n2,n3,k0,t1);

```

```

%For quasi-TM modes we start with a TM solver
kap_low = search_zones_qTM1(mode_order_vert,1);
kap_high = search_zones_qTM1(mode_order_vert,2);
[kap_TM_part1,fval,exitflag] = fminbnd('eigenasymmTM2'
    ,kap_low,kap_high,[],t1,k0,n1,n2,n3);

Beta_TM_part1 = sqrt(k0^2*n2^2-kap_TM_part1^2);
Neff_TM = Beta_TM_part1/k0

H_2_Econv_qTM = Beta_TM_part1/(omega*eps_0);

gam1_qTM = sqrt(Beta_TM_part1^2-k0^2*n1^2);
gam3_qTM = sqrt(Beta_TM_part1^2-k0^2*n3^2);

E_above_0_qTM = (H_2_Econv_qTM/n1^2)*(exp(-gam1_qTM.
    *E_above_0_sub_x));
E_film_qTM=(H_2_Econv_qTM/n2^2)*(cos(kap_TM_part1.
    *E_film_sub_x)-(n2^2/n1^2)*(gam1_qTM/kap_TM_part1)
    .*sin(kap_TM_part1.*E_film_sub_x));
E_film_subs_qTM = (H_2_Econv_qTM/n3^2)*((cos(kap_TM_part1
    .*t1)+(n2^2/n1^2)*(gam1_qTM/kap_TM_part1) .
    *sin(kap_TM_part1.*t1))*exp(gam3_qTM.*
    (E_film_subs_sub_x+t1)));

Ex_qTM = [E_film_subs_qTM';E_film_qTM';E_above_0_qTM'];
Ex_qTMn = Ex_qTM./max(Ex_qTM);
Ix_qTMn = Ex_qTMn.^2;

figure(31);

```

```

clf;
plot(vert_vals,Ix_qTMn,'ro');

%Second part of the effective index method

[search_zones_part2,kap_min,kap_max] = search_zone_finder
    (n4,Neff_TM,n5,k0,t2);
kap_low = search_zones_part2(mode_order_horiz,1);
kap_high = search_zones_part2(mode_order_horiz,2);
%For quasi-TM modes we finish with a TE solver
[kap_TE_part2,fval,exitflag] = fminbnd('eigenasymm_bound',
    kap_low,kap_high,[],t2,k0,Neff_TM,n4,n5);

Beta_qTM_00 = sqrt(k0^2*Neff_TM^2-kap_TE_part2^2);
Neff_qTM_00 = Beta_qTM_00/k0

gam4_qTM = sqrt(Beta_qTM_00^2-k0^2*n4^2);
gam5_qTM = sqrt(Beta_qTM_00^2-k0^2*n5^2);

E_above_0y = exp(-gam5_qTM.*E_above_0_sub_y);
E_filmy = cos(kap_TE_part2.*E_film_sub_y)-
    (gam5_qTM/kap_TE_part2).*sin(kap_TE_part2
    .*E_film_sub_y);
E_film_subsy = (cos(kap_TE_part2.*t2)+(gam5_qTM
    /kap_TE_part2).*sin(kap_TE_part2.*t2))
    *exp(gam4_qTM.*(E_film_subs_sub_y+t2));

Ey_qTM = [E_film_subsy';E_filmy';E_above_0y'];

```

```

Ey_qTMn = Ey_qTM./max(Ey_qTM);
Iy_qTMn = Ey_qTMn.^2;

figure(31);
hold on;
plot(suby,Iy_qTMn,'bo');

Ix_qTMn_mat = repmat(Ix_qTMn,1,L_horiz);
Iy_qTMn_mat = repmat(Iy_qTMn',L_vert,1);

% figure(35);
% mesh(subx,suby,Ix_qTMn_mat);
% view(2);
% figure(36);
% clf;
% mesh(subx,suby,Iy_qTMn_mat);
% view(2);

qTM_field = Ix_qTMn_mat.*Iy_qTMn_mat;
figure(33);
clf;
mesh(subx,suby,qTM_field);
view(2);
H_qTM_modefield = field_size(Iy_qTMn,suby)
V_qTM_modefield = field_size(Ix_qTMn,subx)

%%%%%%%%%%%%%%%%%%%%%%%%%%%%%%%%%%%%%%%%%%%%%%%%%%%%%%%%%%%%%%%%%%%%%%%%
%%%%%%%%%%%%%%%%%%%%%%%%%%%%%%%%%%%%%%%%%%%%%%%%%%%%%%%%%%%%%%%%%%%%%%%%

```